



2018

Design and in vitro characterization of lipids with a pH-sensitive conformational switch and their liposomes for anticancer drug delivery

Shen Zhao
University of the Pacific

Follow this and additional works at: https://scholarlycommons.pacific.edu/uop_etds

 Part of the [Biochemistry, Biophysics, and Structural Biology Commons](#), and the [Pharmacy and Pharmaceutical Sciences Commons](#)

Recommended Citation

Zhao, Shen. (2018). *Design and in vitro characterization of lipids with a pH-sensitive conformational switch and their liposomes for anticancer drug delivery*. University of the Pacific, Dissertation. https://scholarlycommons.pacific.edu/uop_etds/3574

This Dissertation is brought to you for free and open access by the University Libraries at Scholarly Commons. It has been accepted for inclusion in University of the Pacific Theses and Dissertations by an authorized administrator of Scholarly Commons. For more information, please contact mgibney@pacific.edu.

DESIGN AND IN VITRO CHARACTERIZATION OF LIPIDS WITH A pH-SENSITIVE
CONFORMATIONAL SWITCH AND THEIR LIPOSOMES FOR ANTICANCER DRUG
DELIVERY

by

Shen Zhao

A Dissertation Submitted to the

Graduate School

In Partial Fulfillment of the

Requirements for the Degree of

DOCTOR OF PHILOSOPHY

Thomas J. Long School of Pharmacy and Health Sciences
Pharmaceutics and Drug Design

University of the Pacific
Stockton, California

2018

DESIGN AND IN VITRO CHARACTERIZATION OF LIPIDS WITH A pH-SENSITIVE
CONFORMATIONAL SWITCH AND THEIR LIPOSOMES FOR ANTICANCER DRUG
DELIVERY

By

Shen Zhao

APPROVED BY:

Dissertation Advisor: Xin Guo, Ph.D.

Committee Member: Xiaoling Li, Ph.D.

Committee Member: Bhaskara R. Jasti, MPharm, Ph.D.

Committee Member: Lisa Wrischnik, Ph.D.

Committee Member: Dongxiao Zhang, Ph.D.

Department Chair: William K. Chan, Pharm.D., Ph.D.

Dean of Graduate School: Thomas Naehr, Ph.D.

DESIGN AND IN VITRO CHARACTERIZATION OF LIPIDS WITH A pH-SENSITIVE
CONFORMATIONAL SWITCH AND THEIR LIPOSOMES FOR ANTICANCER DRUG
DELIVERY

Copyright 2018

by

Shen Zhao

DEDICATION

This dissertation is dedicated to my parents for their love and support, and is also dedicated to my beloved grandmother.

ACKNOWLEDGMENTS

I would like to express my sincere gratitude to my advisor Dr. Xin Guo for his continuous guidance and support during the years of my graduate studies. I am truly grateful to have the opportunity to work with him on this promising project. I can always get help, insight and encouragement from him in the weekly group meetings. His advice on both research as well as on my personal life have been invaluable.

I would also like to warmly thank Dr. Xiaoling Li and Dr. Bhaskara R. Jasti for their extended discussions and valuable suggestions that have contributed greatly to the improvement of my research. I really appreciate their participation to my dissertation committee. In the same way, I want to thank Dr. Lisa Wrischnik for the help she provided in using the confocal microscope. She has been always supportive and has given me the freedom to use her microscope by myself. Special thanks are due to Dr. Dongxiao Zhang who is a leader outside the university. He is a great mentor who has provided me lots of valuable suggestions both in my studies and in my life. I am honored to have Dr. Lisa Wrischnik and Dr. Dongxiao Zhang on my dissertation committee.

My sincere thanks also go to Yifan Lu who is a partner in my research and a close friend in my life. I am grateful for the time we worked together as a team in many experiments and discussions. I thank the help I received from the professors and students during my research: thank Dr. Andreas Franz and Dr. Vyacheslav Samoshin for their help in measuring my NMR samples; thank Dr. John C. Livesey for letting me use his cell counter and micro-plate reader and training me to use his flow cytometer; thank Dr. William Chan for the use of centrifuge machine; thank Dr. Yu Zheng for his great advises in the lipid synthesis; thank Dr. Patrick Batoon, Dr. Michael Pastor and Chao Feng for their help with mass-spectrometric analysis;

thank Yingbo Huang for his help in organic synthesis; thank Ruiqi Huang and Xinyu Pei for their help with cell culture. I also want to thank Kathy Kassab and Lynda Davis for taking care my documents and purchase requests.

Last, but not least, I would like to thank my parents and grandmother for their unconditional support and endless love, without which I would not have come this far.

Design and in vitro Characterization of Lipids with a pH-sensitive Conformational Switch and Their Liposomes for Anticancer Drug Delivery

Abstract

By Shen Zhao

University of the Pacific
2018

The traditional anticancer drugs are distributed in vivo through systemic blood circulation with a very small portion reaching the tumor site. Targeted drug delivery systems are developed in efforts to concentrate the drug molecules in the tissue of interest while reducing the drug distribution to healthy tissues to reduce the side effects. Liposomes are colloidal systems composed of amphiphilic molecules that assemble into vesicle structures in aqueous media. They are common carriers for targeted drug delivery with the advantages of low toxicity, low immunogenicity and the ability of encapsulating both lipophilic and hydrophilic drugs.

Prior research indicated the advantages of triggered release in drug delivery systems. As a specific example, a series of trans-2-aminocyclohexanol based lipids (flipids) have been reported to illustrate a promising strategy to render pH-triggered drug delivery systems: pH-triggered conformational switch. Based on the foregoing, we hypothesize that incorporation of lipids with a pH-sensitive conformational switch and a long-saturated lipid tail can improve the anticancer activities of stealth liposomes. In this study, six new flipids with C-16 saturated hydrocarbon tails were designed. Such lipids were synthesized with high yields by introducing a catalyst (Copper (II) tetrafluoroborate) at a key step of the synthetic scheme.

pH-sensitive liposomes (fliposomes) composed of flipids were prepared and loaded with the anticancer drug doxorubicin with high encapsulation efficiency. The physicochemical

properties of doxorubicin-loaded liposomes were characterized and their pH-dependent leakage were investigated. The results showed that among all groups liposomes containing the C-16 trans-2-morpholylcyclohexanol-based lipid (Mor-C16) exhibited the largest increase of release as the pH dropped from pH 7.4 to 6.0, indicating its good potential of serving as a component in pH-triggered drug delivery systems.

Three-dimensional multicellular spheroids (3D MCS) are self-assembled microscale tissue analogs *in vitro*. They better mimic the native and complex tumor microenvironment than the conventional two-dimensional cell culture systems. In this dissertation study, 3D MCS of six different human cancer cells were successfully cultured and their growing conditions were optimized to obtain 3D MCS of tight structure and reproducible size. The constructed 3D MCS carried heterogeneously distributed live and apoptotic cells as well as acidic inside pH based on confocal microscopic imaging studies.

The penetration of doxorubicin-loaded Mor-C16 liposomes into 3D MCS was imaged by confocal microscopy in comparison to doxorubicin-loaded non pH-sensitive liposomes and free doxorubicin. The anticancer activities of doxorubicin-loaded Mor-C16 liposomes against 3D MCS of three different cell lines was also evaluated by cell viability. Both the liposome and the non pH-sensitive liposome formulations more efficiently penetrated into two of the three types of 3D MCS compared to free doxorubicin after 4h drug exposure. However, doxorubicin-loaded Mor-C16 liposome imposed higher cytotoxicity to all three types of 3D MCS compared to doxorubicin-loaded non pH-sensitive liposome over 72 h drug exposure. Taken together, we propose that liposomes achieved superior activity against 3D MCS by efficient penetration into 3D MCS, followed by enhanced release of the anticancer drug doxorubicin.

TABLE OF CONTENTS

LIST OF FIGURES.....	14
LIST OF TABLES.....	16
LIST OF SCHEMES.....	18
LIST OF ABBREVIATIONS.....	19
Chapter 1: Introduction.....	20
1.1 Cancer and Solid Tumor.....	20
1.1.1 Cancer.....	20
1.1.2 Solid tumor.....	21
1.1.3 Cancer therapy.....	23
1.2 Anticancer Drugs.....	24
1.2.1 Classification of anticancer drugs.....	24
1.2.2 Doxorubicin.....	25
1.3 Approaches of Targeted Drug Delivery.....	27
1.3.1 Passive targeting.....	27
1.3.2 Active targeting.....	29
1.3.3 Targeted drug delivery systems.....	32
1.3.3.1 Organic nanocarriers.....	32
1.3.3.2 Inorganic nanocarriers.....	34

	10
1.3.3.3 Organic/inorganic hybrid nanocarriers.	36
1.3.3.4 Virus-based nanoparticles.	37
1.4 Liposomes.....	37
1.4.1 Conventional liposomes.	38
1.4.2 Stealth liposomes.....	39
1.4.3 Triggered release from liposomes.	40
1.4.3.1 pH-sensitive liposomes.	41
1.4.3.2 Thermo-sensitive liposomes.	41
1.4.3.3 Ultrasound-sensitive liposomes.	41
1.4.3.4 Magnetic liposomes.	42
1.4.3.5 Light-sensitive liposomes.	43
1.5 Hypothesis.....	43
Chapter 2: Design of pH-Sensitive Lipids with a Conformational Switch to Improve the Anticancer Activities of their Liposome Formulations	44
2.1 Introduction: Strategies of pH-triggered Release Liposomes.....	44
2.2 Design of pH-sensitive Lipids with a Conformational Switch.....	46
2.3 Materials and Methods.....	47
2.3.1 Materials.	47
2.3.2 Synthesis of pH-sensitive lipids with a conformational switch (flipids).....	47
2.4 Results and Discussion	66
Chapter 3: Preparation and Characterization of pH-sensitive Fliposome.....	70

	11
3.1 Introduction on Strategies to Prepare Liposomes	70
3.2 Materials and Methods.....	71
3.2.1 Materials.	71
3.2.2 Preparation of liposome.....	72
3.2.2.1 Preparation of DOX-loaded liposome.	72
3.2.2.2 Preparation of liposomes encapsulating calcein.	73
3.2.3 Physicochemical characterizations of liposomes.	74
3.2.4 Encapsulation efficiency of liposomes.....	74
3.2.5 pH-Triggered release of liposomes.	74
3.2.5.1 pH-Triggered release of DOX-loaded liposomes.....	75
3.2.5.2 pH-Triggered release of calcein-loaded liposomes.	75
3.3 Results and Discussion	76
3.3.1 Lipid compositions in liposome formulations.....	76
3.3.2 Sizes, ζ -potential and polydispersity index (PDI) of liposome formulations...	77
3.3.3 Encapsulation efficiency (EE) of DOX-loaded liposomes.	78
3.3.4 pH-Dependent leakage of liposomes.	79
Chapter 4: Development of 3D Multi-Cellular Spheroids	83
4.1 Introduction on 3D multi-cellular spheroids (MCS).....	83
4.2 Introduction on strategies of generating 3D MCS	85
4.3 Introduction on the methods of imaging 3D MCS.....	87

	12
4.4 Materials and Methods.....	88
4.4.1 Materials.....	88
4.4.2 3D MCS formation under different conditions.....	89
4.4.2.1 3D MCS formation by different cell types.....	89
4.4.2.2 3D MCS formation with different seeding densities.....	89
4.4.2.3 3D MCS formation with and without centrifugation.....	90
4.4.2.4 3D MCS formation with and without extracellular matrix (ECM).....	90
4.4.3 Viability assay for 3D MCS.....	91
4.4.4 pH gradient inside 3D MCS.....	91
4.5 Results and Discussion.....	93
4.5.1 3D MCS formation under different growth conditions.....	93
4.5.2 Imaging the viability of cells in 3D MCS.....	99
4.5.3 pH gradient in 3D MCS.....	100
Chapter 5: Anti-Cancer Activity of pH-Sensitive Liposomes on 3D MCS.....	105
5.1 Introduction: Importance of Anti-cancer Activity Test on 3D MCS.....	105
5.2 Materials and Methods.....	106
5.2.1 Materials.....	106
5.2.2 Cytotoxicity assays for DOX-loaded liposomes on 2D monolayer cells and on 3D MCS.....	107
5.2.3 Confocal microscopic imaging of 3D MCS after treatment with DOX-loaded liposomes.....	108

5.3 Results and Discussion	108
5.3.1 Cytotoxicity of liposome formulations on 3D MCS of different cell lines....	108
5.3.2 Distribution of DOX-loaded liposomes in 3D MCS.....	113
REFERENCES.....	118

LIST OF FIGURES

Figure

1.	Figure 1.1. Physiological Characteristics of Tumor Tissue and Vasculatures	22
2.	Figure 1.2. Chemical Structure of Doxorubicin.....	26
3.	Figure 1.3. Structure of Dendrimers	33
4.	Figure 1.4. Graphical representation of single-walled CNTs (A) and multi-walled CNTs (B)	35
5.	Figure 1.5. Schematics of MSNs	36
6.	Figure 2.1. Clinical applications of pH-sensitive liposomes	45
7.	Figure 2.2. Perturbation of lipid bilayer by an acid-induced conformational switch	46
8.	Figure 3.1. Release Percentage of DOX-loaded liposomes over 12h at four different pHs, 37°C. (n=3) The calculated pKa of each flipid is listed beneath the flipid name	80
9.	Figure 3.2. pH-Dependent Release of Calcein-loaded Fliposomes over 12h at 37°C. (n=3).....	80
10.	Figure 3.3. pH-Dependent Release of Mor-C16 fliposomes over 12 h at 37°C. (n=3) ..	82
11.	Figure 4.1. 3D MCS over 500 µm in diameter	85
12.	Figure 4.2. Scaffold-free methods for MCS formation. (a) liquid overlay, (b) hanging drop, (c) spinning flask cultures, (d) rotary cell cultures	86
13.	Figure 4.3. The emission of SNARF indicates pH is correlated to the ratio of fluorescence at 580/640 nm	92
14.	Figure 4.4. Morphology of Hep3b cells (upper left), Hela cells (upper right), MDA-MB-468 cells (lower left) and Hela-eGFP cells (lower right) after 5 days in culture in the ULA 96 well plates with same seeding conditions: 1000 cells/well seeding density, without collagen and centrifuge.	94
15.	Figure 4.5. 3D MCS of MDA-MB-468 cells after 5, 7, 9 and 11 days of culturing in ULA 96 well plates, starting with different seeding densities	95

16.	Figure 4.6. HeLa-eGFP growth in ULA 96 well plates 5, 7- and 9-days after seeding with and without centrifugation.	96
17.	Figure 4.7. MDA-MB-468 3D MCS growth in ULA 96 well plates at day 5, 9, 13 and 17 after seeding with and without collagen.	97
18.	Figure 4.8. 3D MCS of Hep3b cells at seeding density of 2000 cells/well without centrifugation or collagen	98
19.	Figure 4.9. Confocal Image of the Viability of Cells in A549 (left) and HeLa (right) 3D MCS.	100
20.	Figure 4.10. Confocal Images of HeLa 3D MCS with SNARF-1 at two channels (580 green, 640 red)	101
21.	Figure 4.11. Confocal Images of A549 3D MCS with SNARF-1 at two channels (580 green, 640 red)	102
22.	Figure 4.12. R values of different areas in HeLa and A549 3D MCS	103
23.	Figure 5.1. Viability of MB231 monolayer cells (left) and MB231 3D MCS (right) after 72 h drug exposure.....	109
24.	Figure 5.2. Cell Viability of A549 3D MCS at 8 h exposure (left) and 72 h exposure (right)	110
25.	Figure 5.3. Cell Viability of HeLa 3D MCS after exposure to Dox formulations for 8 h (left) and 72 h (right).....	111
26.	Figure 5.4. Confocal Images of MDA-MB-231 3D MCS (100 μ m deep) Treated with Free Dox (left), Dox-loaded Non pH-sensitive liposome (middle) and Dox-loaded Fliposome (right) for 4 h.....	113
27.	Figure 5.5. Confocal Image of A549 3D MCS (100 μ m deep) Treated with Free Dox (left), Dox-loaded Non pH-sensitive liposome (middle) and Dox-loaded Fliposome (right) for 4 h.....	114
28.	Figure 5.6. Confocal Image of HeLa 3D MCS (100 μ m deep) Treated with Free Dox (left), Dox-loaded Non pH-sensitive liposome (middle) and Dox-loaded Fliposome (right) for 4 h.....	115
29.	Figure 5.7. DOX Fluorescence in Different Depth of A549 3D MCS after 4 h Incubation	117

LIST OF TABLES

Table

1.	Table 1.1. Most Common Cancers in 2018	20
2.	Table 1.2. Types of Cancer Therapy and their Challenges.....	23
3.	Table 1.3. Classification of Anticancer Drugs.....	24
4.	Table 1.4. Advantages and challenges of commonly used targeting ligands in nanoparticle conjugations	29
5.	Table 1.5. Commonly used Organic Nanocarriers.....	33
6.	Table 2.1. Elemental Analysis of C16 flipids	66
7.	Table 2.2. Transition Temperature of Phospholipids.....	67
8.	Table 2.3. Flipids with Saturated C16 Hydrocarbon Tail and Different Amino Head Groups Designed for Studies for this Dissertation.	67
9.	Table 2.4. Yield of Designed Flipids	69
10.	Table 3.1. Lipid Compositions of pH-Sensitive Fliposomes A-F and non pH-Sensitive Control Liposome G	73
11.	Table 3.2. Size and Polydispersity Index of DOX-loaded Liposomes	77
12.	Table 3.3. Encapsulation Efficiency of Dox-loaded fliposomes	78
13.	Table 3.4. NMR-estimated pKa in CD ₃ OD versus Calculated pKa in water of flipids... ..	82
14.	Table 4.1. Comparison of scaffold-free techniques used for 3D MCS formation.....	86
15.	Table 4.2. Optimized Conditions to Construct 3D MCS of Six Different Human Cancer Cell Lines	99
16.	Table 5.1. IC ₅₀ of Different Dox Formulations on monolayer and 3D MCS of MDA-MB-231 cells after 72 h exposure.	109
17.	Table 5.2. IC ₅₀ of Different Dox Formulations on A549 3D MCS after 8 h and 72 h exposure	110

18.	Table 5.3. IC ₅₀ of Different Dox Formulations on Hela 3D MCS after 8 h and 72 h exposure	111
-----	--	-----

LIST OF SCHEMES

Schemes

1. Scheme 1.1. A Liposome Formed by Amphiphilic Molecules in Aqueous Phase 38
2. Scheme 1.2. A Scheme of PEGylated (Stealth) Liposome 40
3. Scheme 2.1. Synthesis of pH-sensitive lipids with a conformational switch 48

LIST OF ABBREVIATIONS

AZTTP	azidothymi-dine 5-triphosphate
CPBA	chloroperoxybenzoic acid
CPP	cell penetrating peptide
C ₁₂ E ₈	octaethylene glycol monododecyl ether
DART	Direct Analysis in Real Time
DAPE	diacetylenic-phosphatidyl-ethanolamine
DMEM	Dulbecco's Modification of Eagle's Medium
DMSO	dimethyl sulfoxide
DOPE	dioleoyl-phosphatidyl-ethanolamine
DLPC	1,2-dilauroyl-sn-glycero-3-phosphocholine
DMPC	1,2-dimyristoyl-sn-glycero-3-phosphocholine
DSPC	1,2-distearoyl-sn-glycero-3-phosphocholine
DOX	doxorubicin
ECM	extracellular matrix
EE	encapsulation efficiency
EPR	enhanced permeability and retention
HEPES	2-[4-(2-hydroxyethyl)piperazin-1-yl]-ethanesulfonic acid
LUV	large unilamellar vesicles
MLV	multilamellar vesicles
MPS	mononuclear phagocyte system
MSN	mesoporous silica nanoparticles
NIPAM	N-isopropylacrylamide
PEG	polyethylene glycol
POPC	1-palmitoyl-2-oleoyl-glycero-3-phosphocholine
ULA	ultra-low attachment

Chapter 1: Introduction

1.1 Cancer and Solid Tumor

1.1.1 Cancer. Cancer is a collection of related diseases that involve non-stopping abnormal cell growth with the ability of spreading into surrounding tissues[1]. The term cancer is derived from the Latin word of crab, meaning “grab on and don’t let go”[2]. There are over 100 types of cancers affecting humans, which jointly represent the second cause of death in the United States[3]. The most common cancers worldwide, as reported by World Health Organization (WHO) in 2018 are listed in Table 1.1.

Table 1.1. Most Common Cancers in 2018[4]

Cancer Types	Cases (million)
Lung	2.09
Breast	2.09
Colorectal	1.80
Prostate	1.28
Skin (non-melanoma)	1.04
Stomach	1.03

Cancer is a genetic disease and arises from the transformation of normal cells into cancer cells due to the changes of genes that control the cells growth and division. The majority of cancers are attributed to the genetic mutations from environmental factors while others are due to inherited genetics[5]. The common environmental factors include:

- Physical factors: ionizing radiation, ultraviolet

- Diet and exercise factors: specific foods, obesity, lack of physical activity
- Chemical factors: tobacco, aflatoxin, arsenic
- Biological factors: Helicobacter pylori, hepatitis B, hepatitis C, human papillomavirus, Epstein-Barr virus and HIV[6].

1.1.2 Solid tumor. A tumor, also known as neoplasm, is an abnormal growth of cells that form a mass[7]. When the growth occurs in solid tissues such as an organ, muscle or bone, it is called a solid tumor. Blood cancer do not usually take the form of a solid tumor. There are two types of solid tumors: benign (noncancerous) and malignant (cancerous). Benign tumors usually grow slowly and do not invade adjacent tissues. Most of them respond well to treatments. Malignant tumors are cancerous. They can invade nearby tissues and organs and may spread to other parts of the body[8]. Based on the types of cells forming the solid tumor, they can be divided into four categories[9]:

- Carcinoma: formed from epithelial cells, such as prostate, stomach, lung, pancreas, liver
- Sarcoma: formed in connective tissues, such as cartilage, fat, bones and nerves
- Germ cell tumor: sperm and egg cells
- Blastoma: formed from embryonic tissue

The physiological characteristics of solid tumor (Figure. 1.1) are so different from normal tissue in that neovasculature is developed in the tumor microenvironment to ensure an adequate supply of nutrients and oxygen[10]. The newly formed vessels within different parts of the tumor create an imbalance of pro- and anti-angiogenic signaling, leading to the formation of abnormal vascular network with dilated, tortuous and saccular channels[11, 12]. Unlike the ordered microvasculature of normal tissue, tumor microvasculature shows disorganized, enlarged vessels and unidentifiable arterioles, capillaries and venules[13, 14].

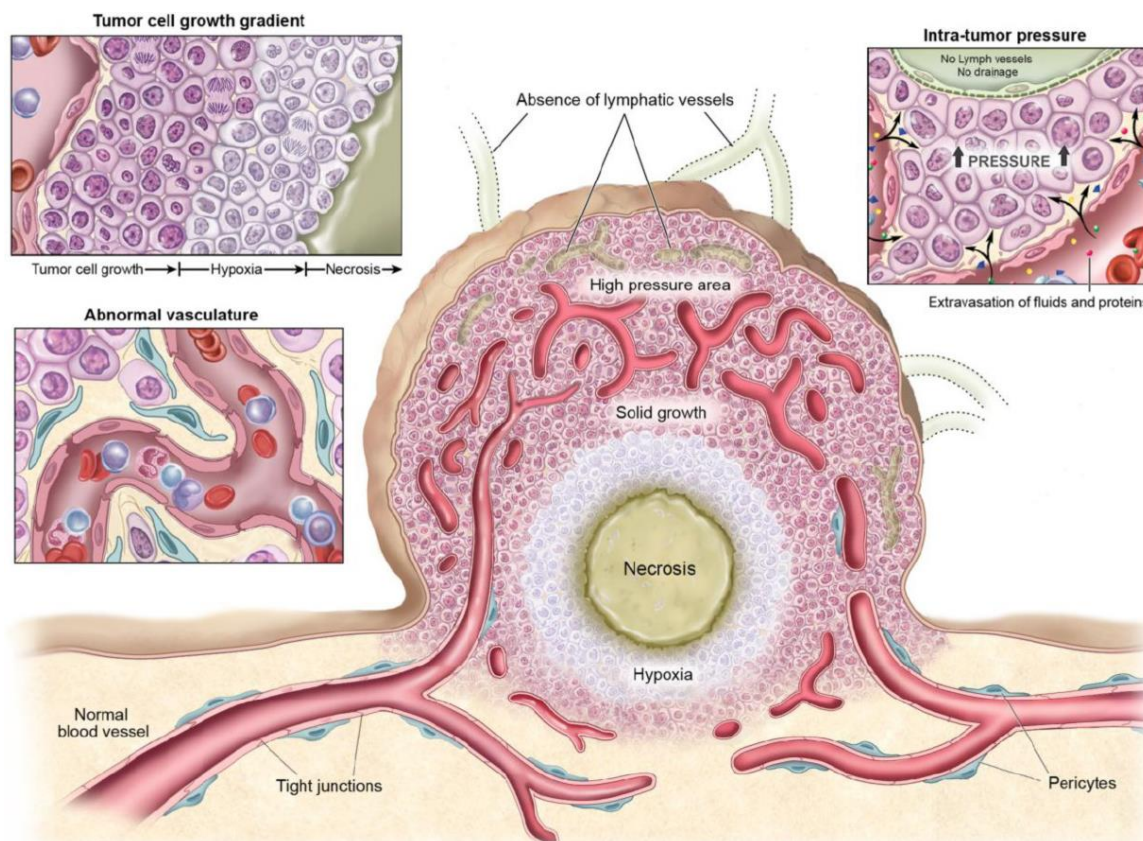


Figure 1.1. Physiological Characteristics of Tumor Tissue and Vasculatures[15]

Tumor blood vessels show structural abnormalities in that the endothelial surface is fenestrated with gaps and that the endothelial cells are surrounded by discontinuous membranes[16, 17]. Furthermore, the lack of lymphatic vessels causes the low clearance of the interstitial fluid inside the solid tumor. Most nano-sized drug delivery systems with long circulation times can accumulate within solid tumors by leaking through the abnormal tumor vasculature and then by retaining inside the tumor due to the reduced lymphatic drainage. This is the mechanism of the well-known enhanced permeability and retention (EPR) effect[18].

The cell proliferation inside the solid tumor is heterogeneous because of the imbalanced blood supply, resulting a higher cellular density near blood vessel[19]. A necrosis zone is formed in the core of solid tumor due to the lack of nutrients. Multi-gradients of oxygen, carbon dioxide and pH have been detected inside the solid tumor due to its abnormal microenvironment[20].

1.1.3 Cancer therapy. There are many types of cancer therapy for different types and stages of cancer. Traditional anticancer treatments include surgery, radiotherapy and chemotherapy. Most of the time, a combination of two or more treatments are applied depending on the condition of the patient[6]. Current common cancer therapies are summarized in Table 2 together with their challenges.

Table 1.2. Types of Cancer Therapy and their Challenges[21]

Types of Cancer Therapy	Methodology	Challenges
Surgery	Remove cancer tissues using scalpels, laser, hyperthermia or photodynamic therapy	Works only for solid tumors that are contained in one area; pain after surgery and risk of infection
Radiation	Use high doses of radiation to kill cancer cells or improve symptoms	Side effects: affect nearby healthy tissue; cause fatigue on patient
Chemotherapy	Use one or more cytotoxic drugs to kill cancer cells	Side effects: damage to healthy cells; cause fatigue on patient
Immunotherapy	Stimulate or help the immune system to fight cancer	Side effects: skin reactions at needle site; flu-like symptoms; heart palpitations; diarrhea and risk of infection
Targeted therapy	It is a form of chemotherapy that targets	Drug resistance; difficulty in developing drugs for

	specific molecular of cancer cells	some targets; side effect: diarrhea and liver problems
Hormone therapy	Slows or stops the growth of cancers (prostate for male and breast cancer for female) that need hormones to grow	Side effects for men: hot flashes, weakened bones, diarrhea, nausea and fatigue Side effects for women: hot flashes, nausea, mood changes and fatigue
Precision medicine	It is also called personalized medicine that is tailored to the genetic changes in each patient's cancer.	Not yet apply to everyone; treatment using precision medicine can be expensive

1.2 Anticancer Drugs

The first chemotherapy drug to treat cancer was developed in the early 20th century when mustard gas was discovered to be a potent suppressor of hematopoiesis[22]. Since then many other drugs have been developed for the treatment of a variety of cancers with different stages[23].

1.2.1 Classification of anticancer drugs. Generally, anticancer drugs can be grouped by their mechanism of actions. Major classes of anticancer drugs include: cytotoxic drugs, targeted drugs and hormonal drugs (Table 1.3). Understanding of the classification of anticancer drugs can be useful for a comprehensive view of the available drugs in each class and for the design of combination treatments[24].

Table 1.3. Classification of Anticancer Drugs[25]

Class	Type	Example of drugs
Cytotoxic	• Alkylating agents	• Cisplatin, Carboplatin

	<ul style="list-style-type: none"> • Antimetabolites • Microtubule damaging agents • Topoisomerase inhibitor • Antibiotics • Miscellaneous 	<ul style="list-style-type: none"> • Methotrexate, Gemcitabine • Vincristine, Vinblastine • Etoposide, Topotecan • Doxorubicin, Bleomycin • Tretinoin, Hydroxyurea
Targeted	<ul style="list-style-type: none"> • Tyrosine protein kinase inhibitor • EGF receptor inhibitor • Angiogenesis inhibitor • Proteasome inhibitor • Unarmed monoclonal antibody 	<ul style="list-style-type: none"> • Imatinib, Nilotinib • Gefitinib, Erlotinib • Bevacizumab • Bortezomib • Rituximab, Trastuzumab
Hormonal	<ul style="list-style-type: none"> • Glucocorticoids • Estrogens • Aromatase inhibitors • Antiandrogen • 5-α reductase inhibitor • GnRH analogues • Progestins 	<ul style="list-style-type: none"> • Prednisolone • Fosfestrol, ethinylestradiol • Letrozole, Anastrozole • Flutamide • Finasteride • Nafarelin, Triptorelin • Hydroxyprogesterone acetate

1.2.2 Doxorubicin. Doxorubicin (DOX or DXR) (Figure 1.2), is a member of the natural products called anthracyclines, which is produced by the soil fungus *Streptomyces*[26]. DOX is an effective chemotherapeutic belonging to the antibiotic category of cytotoxicity anticancer drugs[27]. DOX is used to treat a wide range of cancers including breast cancer, bladder cancer, Kaposi's sarcoma, lymphoma and acute lymphocytic leukemia[28, 29]. It is given by an intravenous injection and often used in a combination with other chemotherapy drugs[30].

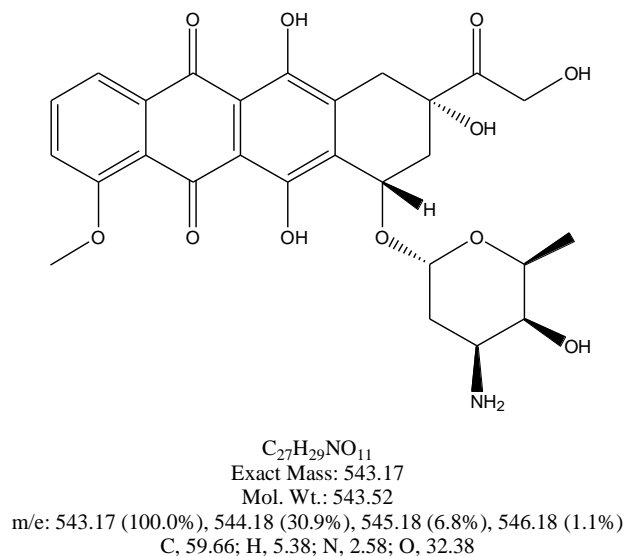


Figure 1.2. Chemical Structure of Doxorubicin

The anticancer activity of DOX comes from its interaction with DNA by intercalation and from inhibition of macromolecular biosynthesis[31, 32]. It is reported that DOX inhibits the resealing of DNA double helix by the topoisomerase II (TOP II) complex, an enzyme responsible for relaxing supercoils in DNA during transcription[31]. DOX was also shown to evict histones to induce cell death that is independent of TOP II[33]. It is highly likely that the anti-cancer effects of DOX results from a variety of mechanisms of inhibiting DNA synthesis[34, 35].

DOX was first approved for medical use by FDA in 1974[30]. It is one of the most effective and essential medicines for cancer therapy according to the World Health Organizations' report in 2015[36]. While the majority of anticancer drugs are only effective towards tumor cells in their exponential phase, DOX can arrest the cell cycle at all stages. However, the clinical use of DOX is restricted by several side effects including vomiting, bone

marrow suppression, alopecia, mucositis and especially dose-dependent cardiotoxicity[37, 38]. The most dangerous side effect of DOX is dilated cardiomyopathy with no effective treatment[39]. The liposome-encapsulated DOX carries less cardiotoxic than free DOX, leading to the development and approval of the first nano-drug “Doxil”.

DOX is a fluorescent molecule that is typically excited at 480 nm and detected of its emission between 560 - 590 nm. DOX’s broad spectrum of anticancer activity and fluorescence makes it an attractive model drug in the development of anticancer drug delivery systems.

1.3 Approaches of Targeted Drug Delivery

Traditional anticancer drugs are distributed in the body through systemic blood circulation. Only a very small portion of drugs reaches the tumor site. Thus, targeted drug delivery systems are developed in efforts to concentrate the drug molecules in the tissue of interest while reducing the drug distribution to healthy tissues to reduce the side effects. Another advantage of targeted drug delivery would be prolonged drug exposure to tumor, which allow less frequent dosages. Effective targeted drug delivery systems require 1) efficient drug loading into carriers, 2) sufficient residence in the blood circulation, 3) enhanced retention in the target side, and 4) efficient drug release within a period for effective function of the drug[40]. Generally, there are two kinds of drug targeting approaches, passive targeting and active targeting.

1.3.1 Passive targeting. Passive targeting is the monitoring of the physicochemical properties of drug delivery systems to influence their distribution in vivo. One important application of passive targeting is the enhanced permeation and retention (EPR) effect of solid tumors. As we discussed above, most nano drug delivery systems (10 – 400 nm) with long

circulation time accumulate more in solid tumors than in normal tissues by permeating preferentially into tumor tissue through its leaky vasculature and retaining inside due to the lack of effective lymphatic drainage[18]. The long circulation time of the nanocarriers can be achieved by coating polyethylene glycol (PEG) to the surface of the delivery systems to minimize the adsorption of serum proteins that trigger immune responses that promote clearance. With the PEG coating water molecules can hydrogen bond with the oxygen molecules on PEG to form a film of hydration around the nanocarriers, thus hinder their detection and clearance by the mononuclear phagocyte system (MPS)[41]. It was found that the increased systemic circulation time is dependent upon the molecular weight of the PEG. Generally, higher average molecular weight of PEG leads to longer circulation time, except that the liver clearance is found to be enhanced when the average molecular weight of PEG reaches above 50,000[42]. Nanocarriers with a size between 10 – 100 nm have been found to have a longer systemic circulation time[43].

There are several challenges of passive targeting for anticancer drug delivery. First, the drug delivery systems must come in close proximity to the tumor site for the EPR effect to take place. Second, there is a severe lack of clinical data on the EPR effect. The tumor growth rate in animal models is not comparable to that in human. EPR effect has been found to differ from tumor to tumor xenografts[44]. Models being used to study EPR in laboratories are not sufficiently accurate in representing EPR effect in patients. Third, although PEGylated drug delivery systems have increased systemic circulation times, the actual percentage of PEGylated nanocarriers accumulating at the tumor site is still very limited. For example, it is shown in an animal study that only 5% of the administered PEGylated niosomes remained in the systemic circulation after 12 h and about 80% of the initial dose was eliminated in less than a few hours[45].

1.3.2 Active targeting. Active targeting enhances the drug accumulation at the target site by two strategies: ligand-receptor mediated active targeting and locally activated drug delivery. The former is achieved by incorporating ligands on the drug carriers' surface to selectively bind over-expressed receptors on target cells[46]. The latter is to trigger the drug release from the carriers either by a signal specific at the site or by external stimulus, such as light, temperature, magnetic field and ultrasound[47].

Tumor cells overexpress many specific biomarkers on their surface, making it possible to design ligands for specific binding[48]. Conjugation of tumor-specific ligands to nanocarriers is a common approach to achieve active targeting that further improves a nano drug delivery system already with proper physicochemical properties for passive targeting[49]. Following binding of the ligand with its receptor, the actively targeted nanocarriers can be internalized by tumor cells through receptor-mediated endocytosis[48]. Several ligands against various tumor biomarkers have been extensively studied. Some of the most commonly used targeting ligands that have been conjugated to nanoparticles are listed in Table 1.4, together with their advantages and challenges.

Table 1.4. Advantages and challenges of commonly used targeting ligands in nanoparticle conjugations[50]

Ligands conjugated NPs	Advantages	Challenges
Transferrin conjugated NPs	<ul style="list-style-type: none"> • Overexpression of Transferrin receptor on metastatic and drug resistant tumors • Easily conjugated to a variety of materials 	<ul style="list-style-type: none"> • Nonspecific distribution and targeting • A risk of overdose of iron transport into brain caused by an exogenously-supplied transferrin

	<ul style="list-style-type: none"> • High intracellular uptake • Prolonged circulation time and significantly increased tumor accumulation 	
Cell-penetrating peptides (CPPs) conjugated NPs	<ul style="list-style-type: none"> • Be able to cross cell membrane independent of energy • Efficiently internalize the associated biomolecules with no decreased biocompatibility • Be able to protect the bioactive conjugates from degradation and increase the serum half-life of cargoes • Low cytotoxicity 	<ul style="list-style-type: none"> • The transmembrane mechanism is unclear • The biological activity of conjugates may change in some cases
Low-Density Lipoproteins conjugated NPs	<ul style="list-style-type: none"> • Natural carrier with high biocompatibility • Non-immunogenic • Be able to encapsulate both hydrophobic and amphiphilic drugs • LDL receptor is highly expressed in most tumor cells 	<ul style="list-style-type: none"> • Existence of LDL receptors on normal cells • Concern of introduction of pathogens
Integrin modified NPs	<ul style="list-style-type: none"> • Some integrins are highly over-expressed on many cancer cells • Integrin signaling control diverse functions in tumor cells 	<ul style="list-style-type: none"> • Existence of integrins on normal cells

	<ul style="list-style-type: none"> • Highly accessible cell surface receptors 	
Carbohydrates modified NPs	<ul style="list-style-type: none"> • Effective oral delivery system • Improved bioavailability 	<ul style="list-style-type: none"> • Some degree of toxicity
Folate modified NPs	<ul style="list-style-type: none"> • Folate receptor is overexpressed on the majority of cancer cells • Folate is small and stable • Inexpensive and nonimmunogenic 	<ul style="list-style-type: none"> • Uptake of folate can sometimes promote cancer cell proliferation and migration

There are a number of challenges in ligand-receptor mediated active targeting. First, the binding can only occur when the two components are close enough (< 0.5 nm). Current drug delivery systems do not have the ability to guide themselves to a target beyond the scope[49]. Second, some studies showed that the presence of targeting ligand did not always result in enhanced accumulation of the drug inside the target site[51, 52]. Third, the expression of a specific receptor may not be homogeneously distributed in a tumor and is subject to change on the surface over time[53]. Finally, the expression of the receptor in cultured cancer cells in vitro may not represent the properties in a patient's tumor.

The locally activated drug delivery system can respond to specific stimuli to trigger the release of the entrapped drug, leading to an increased accumulation inside the tumor. For example, activate targeting systems were designed to release the cargo in response to hypoxia inside the tumor site[54]. Another specific active targeting system was developed to trigger the payload release based on the lowered pH inside the tumor[55].

1.3.3 Targeted drug delivery systems. Targeted drug delivery systems have been developed to treat many diseases, such as cardiovascular diseases and diabetes, but the most important application of them is to treat cancerous tumors. It has been reported that the pore cut-off size of several tumor models is within the range of 380 and 780 nm[16, 56]. In order to take the advantage of EPR effect, nano-sized drug delivery systems are extensively studied. Many terms have been used to describe these nano drug delivery systems including: nanocarrier, nanovehicle, nanosystem, etc. An ideal nanocarrier must be biocompatible, non-toxic and non-immunogenic[57]. Most commonly used targeted drug delivery nanocarriers can be classified into four categories: organic nanocarriers, inorganic nanocarriers, organic/inorganic hybrid nanocarriers and virus-based nanoparticles[58].

1.3.3.1 Organic nanocarriers. There are many types of organic nanocarriers based on their compositions and structures. The most commonly used organic nanocarriers include solid lipid nanoparticles, liposomes, dendrimers (Figure 1.3), polymeric nanoparticles and polymeric micelles (Table 1.5).

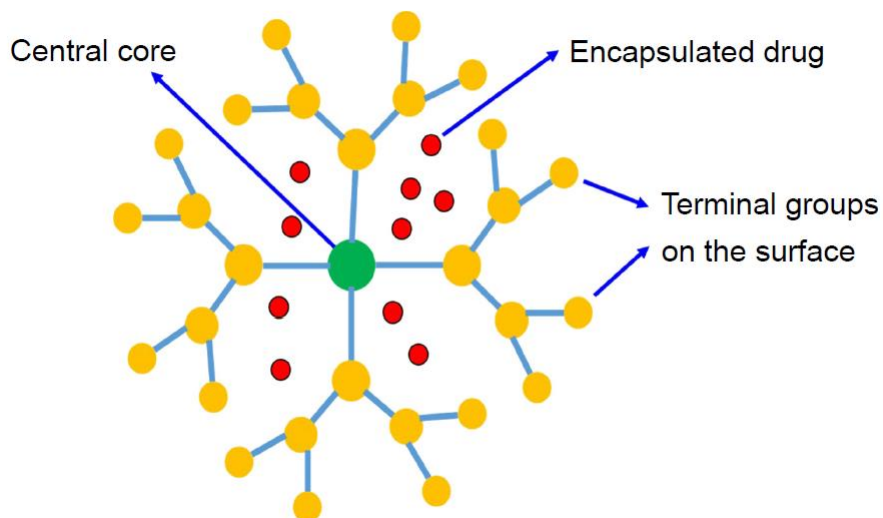


Figure 1.3. Structure of Dendrimers[58]

Table 1.5. Commonly used Organic Nanocarriers[58]

Organic nanocarriers	Feature	Preparation method
Solid lipid nanoparticles	<ul style="list-style-type: none"> • Size range of 50 – 1,000 nm • Highly lipophilic lipid matrix for lipophilic drug encapsulation • Economical large-scale production 	<ul style="list-style-type: none"> • Dispersing melted solid lipid in water with stabilizer of emulsifiers by high pressure homogenization and microemulsification
Liposomes	<ul style="list-style-type: none"> • Spheroid shape with aqueous core and bilayer shell • Capable of encapsulating both lipophilic and hydrophilic drugs • Biodegradable and biocompatible 	<ul style="list-style-type: none"> • Lipid film hydration • Ethanol injection
Dendrimers	<ul style="list-style-type: none"> • Frequently branched macromolecules 	<ul style="list-style-type: none"> • Stepwise synthesis

	<ul style="list-style-type: none"> • Distinctive molecular weight • Average size range of 1.5 – 14.5 nm • Extraordinarily controlled shape 	
Polymeric nanoparticles	<ul style="list-style-type: none"> • Solid colloidal particles of 10 – 1,000 nm in size • Biodegradable polymers • High encapsulation capacity • Good stability on storage and in vivo • Prolonged circulation time. 	<ul style="list-style-type: none"> • Dispersion of preformed polymers • Direct polymerization of monomers
Polymeric micelles	<ul style="list-style-type: none"> • Self-assembled copolymers of di- or tri-block • Small size of 10 – 100 nm • Capable of encapsulating both lipophilic and hydrophilic drugs • Formation above critical micelle concentration 	<ul style="list-style-type: none"> • Dialysis • Oil-in-water emulsion • Solvent evaporation • Co-solvent evaporation • Freeze-drying method

1.3.3.2 Inorganic nanocarriers. Certain inorganic materials can be used to make nanocarriers for drug delivery due to their distinctive physicochemical and biological characteristics. Carbon nanotubes and mesoporous silica nanoparticles are two examples with many applications in delivery anticancer drugs, such as paclitaxel[59, 60], doxorubicin[61, 62] and methotrexate[63, 64].

- Carbon nanotubes (CNTs): CNTs are tube-like structures of carbon atoms that are formed by rolling up graphene sheets[65]. Single-walled or multi-walled carbon nanotubes

(Figure 1.4) can be formed with an outer diameter of 0.4 – 2 nm and 2 – 100 nm, respectively[66]. CNTs can be produced using a variety of techniques such as discharge, laser ablation and thermal chemical vapor deposition[67]. Some of the unique features of CNTs include nanoneedle shape, high mechanical strength, high electrical and thermal conductivities. The major limitations of CNTs are their poor water solubility and toxicity[66].

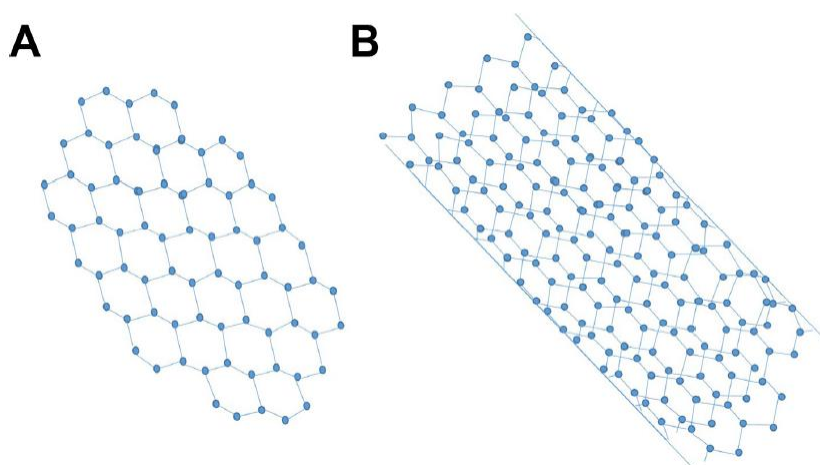


Figure 1.4. Graphical representation of single-walled CNTs (A) and multi-walled CNTs (B)[58]

- Mesoporous silica nanoparticles (MSNs): MSNs are honeycomb-like particles (Figure 1.5) with pores of 2 to 50 nm in size[68]. Both hydrophilic and lipophilic drugs can be loaded into these pores, which make them promising inorganic nanocarriers. Furthermore, MSNs possess many other advantages including large specific surface area, good biocompatibility and convenience for mass production[69]. In addition, their

surface can be easily modified with active targeting ligands to enhance therapeutic efficacy and to reduce side effects[70].

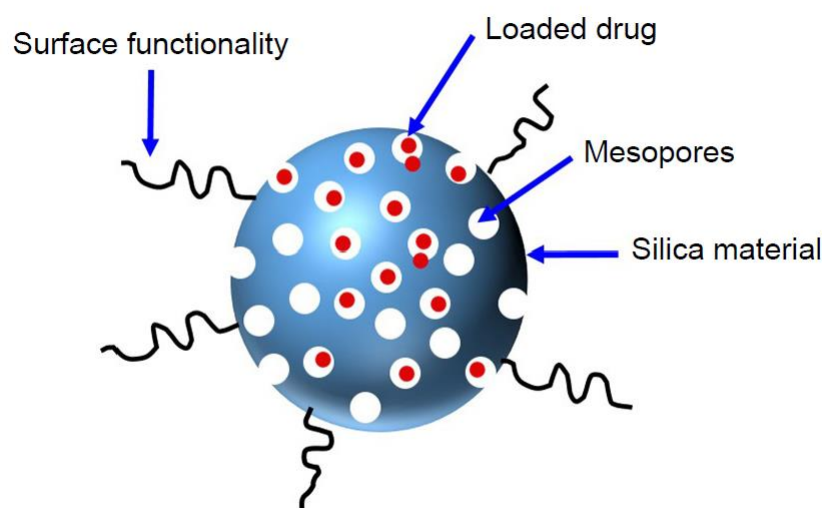


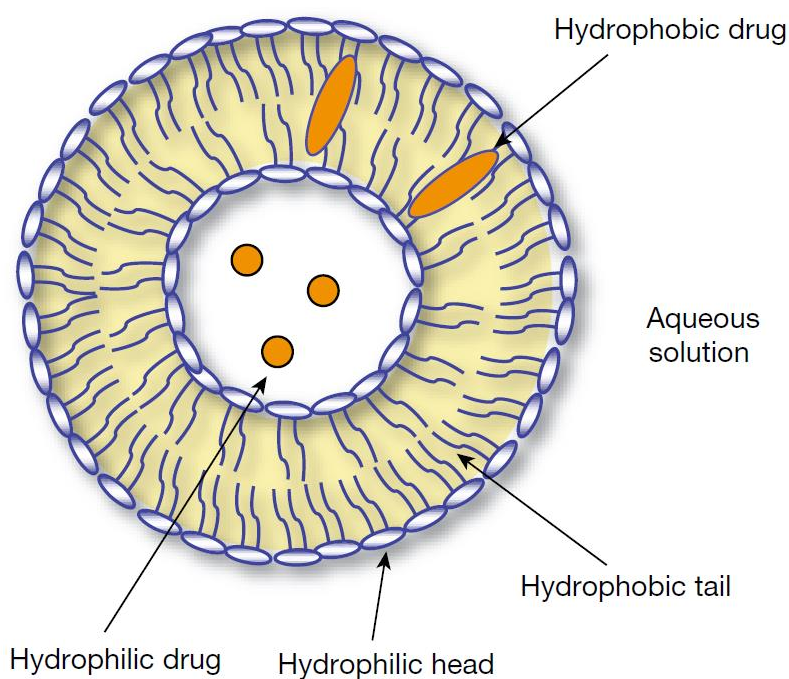
Figure 1.5. Schematics of MSNs[58]

1.3.3.3 Organic/inorganic hybrid nanocarriers. Organic/inorganic hybrid nanocarriers are designed to take advantage of both types of nanocarriers and to overcome their limitations. For example, inorganic nanocarriers of mesoporous silica nanoparticles (MSNs) were coated with polyethyleneimine (PEI) to form new hybrid nanocarriers that showed enhanced cellular uptake[71]. In another study, a MSNs/lipid bilayer hybrid system was developed to encapsulate zoledronic acid for an improved drug retention in a breast cancer model[72]. Han et al, also reported an increased DOX uptake using a lipid-capped MSNs hybrid system compared with control groups[73].

1.3.3.4 Virus-based nanoparticles. Most virus capsids are about 20 – 500 nm in diameter. They are considered as naturally formed protein cages with uniform nanostructures and well-defined geometry[74, 75]. Recently, studies of virus-based nanocarriers have been widely explored for drug delivery, gene therapy, vaccination and targeting[76]. Virus-based nanoparticles (VNPs) or virus-like particles (VLPs) from different sources have been investigated because of their attractive features including biocompatibility, morphological uniformity and high stability[77]. Drugs can either be physically encapsulated in VNPs or chemically linked to the surface[78]. As a targeted drug delivery nanocarrier, VNPs can be functionalized for active targeting by either genetic modification or by chemical bioconjugation. Many studies have suggested that VNPs could be very promising nanocarriers for tumor targeting[79, 80].

1.4 Liposomes

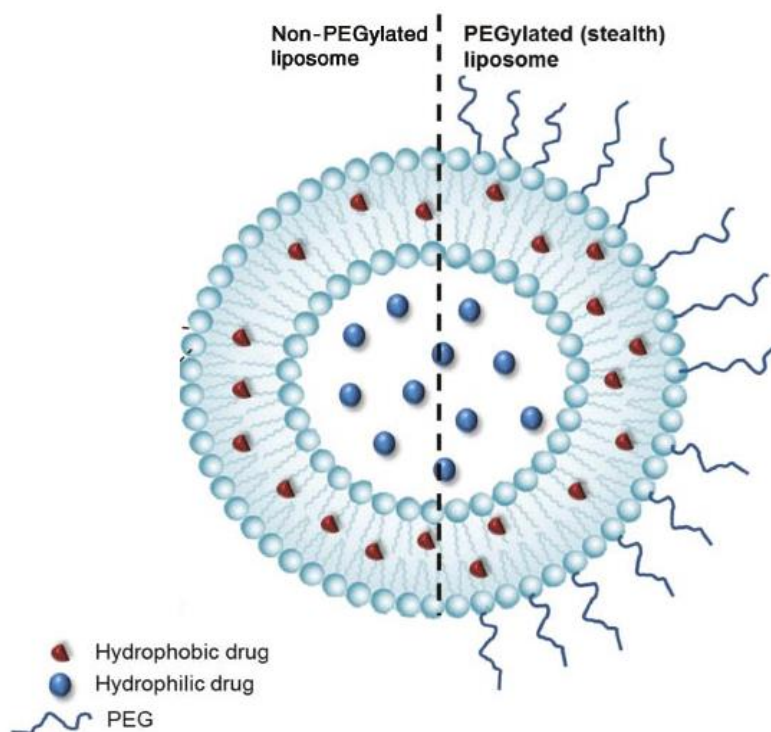
Liposomes (Scheme 1.1) are colloidal systems composed of amphiphilic molecules, most often phospholipids, that assemble in aqueous media into spherical structures with one or several concentric membranes[81]. They have spheroid shape structures with the size ranging from 20 to 10,000 nm. They are the most commonly used carriers for targeted drug delivery with the advantages of low toxicity, low immunogenicity and biocompatibility[82]. Liposomes can encapsulate both lipophilic drugs in the lipid bilayer and hydrophilic drugs in the aqueous core. The major types of liposomes are multilamellar vesicle (MLV), small unilamellar vesicle (SUV) and large unilamellar vesicle (LUV).



Scheme 1.1. A Liposome Formed by Amphiphilic Molecules in Aqueous Phase[83]

1.4.1 Conventional liposomes. Conventional liposomes are made up of phospholipids. Upon intravenous administration, they are rapidly captured by the mononuclear phagocyte system (MPS) and eliminated from the blood circulation, leading to a very short half-life[84]. This feature of conventional liposome was exploited for efficient delivery of antiparasitic and antimicrobial drugs to the MPS to treat infections[85, 86]. However, their use is limited when the target site is beyond MPS. Furthermore, it was reported conventional liposomes could interact with high and low density lipoproteins in the plasma resulting in rapid release of the encapsulated drug[87]. It was also found that the enhanced MPS uptake of conventional liposomes by the liver is size-dependent. Larger liposomes are eliminated by the MPS much faster than smaller ones[88].

1.4.2 Stealth liposomes. A stealth liposome (Scheme 1.2), also called a PEGylated liposome, is a liposome with a poly ethylene glycol (PEG) coating on the outer membrane. PEG is the most widely used polymeric steric stabilizer that is biocompatible, low toxic and very low immunogenic. PEG can be incorporated on the liposomal surface in several ways such as 1) physical adsorption onto the surface of the liposome, 2) covalent attachment onto the surface of liposome, 3) incorporation of a PEG-lipid conjugate during liposome preparation. The presence of PEG on the liposome surface significantly reduces the MPS uptake, thus prolongs the half-life in the blood circulation[89]. In addition, a reduced interaction of stealth liposomes with plasma proteins also increases the blood circulation time[90]. Furthermore, it was reported that PEG could stabilize liposome preparations by providing a strong inter-bilayer repulsion that counters the attractive Van der Waals forces that facilitates liposome aggregation[91].



Scheme 1.2. A Scheme of PEGylated (Stealth) Liposome

Stealth liposomes are important in cancer therapy. As an example of stealth liposomes, DOXIL was the first FDA approved PEGylated liposomal formulation containing Doxorubicin. Stealth liposomes can be further modified by a variety of targeting ligands for active targeting. Moreover, it is reported that stealth liposomes with a cell-penetrating peptide can be used for intracellular targeting[87].

1.4.3 Triggered release from liposomes. In order to increase the efficacy of the anticancer drug payload of liposomes after their accumulation at the target side, many liposome formulations have been developed to elevate the release of the payload drug in response to

specific stimuli at the target site (aka triggered release). Common strategies to achieve triggered release are discussed hereafter.

1.4.3.1 *pH-sensitive liposomes.* pH-sensitive liposomes (pHSLs) are designed to elevate the release of the encapsulated drug in response to the pH decrease from blood (pH 7.4) to tumor interstitium (pH 5.7 – 7.8) or to endosomes/lysosomes (pH 4.5 – 5.5)[92, 93]. Mechanistically, pH-sensitive liposomes are rapidly destabilized under acidic conditions. pH-sensitivity has been shown as the most biocompatible strategy for triggered release into cytoplasm[94]. The pH-sensitive liposomes have been designed to deliver a variety of agents intracellularly and intercellularly, such as anticancer drugs, DNA, antisense oligonucleotides, proteins, peptides, and contrasting agents[95]. More details about pH-sensitive liposomes are discussed in Section 2.1.

1.4.3.2 *Thermo-sensitive liposomes.* Thermo-sensitive liposomes (TSLs) are designed to release cargo in response to local hyperthermia[94]. It has the advantage that it is not dependent on the EPR effect due to its rapid release of the drug in the microvessels of the tumor during hyperthermia treatment[96]. TSLs must be stable at 37°C and yet be able to release the drug in a slightly higher temperature range of 39-42°C[97]. There are many studies on TSLs containing DPPC, which possesses a phase transition temperature of 41.9°C. The anticancer activity of DOX-loaded TSL can be further enhanced by modifying the surface of TSL with cRGD ligands that bind to $\alpha_v\beta_3$ integrin, which is overexpressed in many cancer cells. The in vivo accumulation of DOX from a cRGD modified TSL at tumor site was shown to be 5-fold higher than that from the corresponding non-targeted TSL[98].

1.4.3.3 *Ultrasound-sensitive liposomes.* Echogenic (ultrasound-triggered) liposomes (Els) are designed to co-encapsulated air and drug, which allow them to react to ultrasound

stimuli[99]. The hypothesis to explain it is that the ultrasound waves can cause an air pocket expansion to disrupt the lipid bilayer. It is possible to obtain a bolus release with only a single high amplitude ultrasound pulse and a sustained release with a series of low amplitude pulses[100]. Kee et al. developed a papaverine hydrochloride encapsulated Echogenic liposome that greatly reduced side effects while maintained the inhibitory activity of the drug[101]. In another study, a perfluoropentane and DOX co-encapsulated echogenic liposome containing 1,2-dipalmitoyl-sn-glycero-3-phosphocholine (DPPC) released 80% of the DOX after low-intensity ultrasound exposure[102].

1.4.3.4 Magnetic liposomes. Magnetic liposomes (MLs) contain Fe_3O_4 or $\gamma\text{-Fe}_2\text{O}_3$ and are designed to release the cargo drug in response of an external magnetic field[103]. MLs can be used as diagnostic agents such as MRI contrast agents[104] as well as heat mediators in hyperthermia therapy that uses an alternating magnetic field[105]. The goal of using MLs in anticancer therapy is to enhance drug accumulation at the tumor site while reducing the side effects. Saiyed et al. developed a ML delivery system encapsulating azidothymidine 5-triphosphate (AZTTP), which elevated the permeability of AZTTP by 3-fold under an external magnetic stimulus in an in vitro blood brain barrier model of HIV-infected peripheral blood mononuclear cells[103]. Generally, when a high-frequency alternating magnetic field is applied, hyperthermia is often triggered as well, which suggests an potential of developing a combined trigger release system for anticancer therapy[106]. Surface modification by targeting ligands can improve the affinity of MLs to tumor cells. For example, RGD-coated MLs were prepared to deliver sodium diclofenac into cerebral inflammatory sites. The resultant delivery system showed much higher drug distribution in brain than the free drug (9.1 fold), the conventional RGD-coated liposomes (6.62 fold) and the uncoated ML formulation (1.5 fold)[107].

1.4.3.5 Light-sensitive liposomes. Light-sensitive liposomes (LSLs) are constructed with light-sensitive lipids, which trigger the drug release upon exposure to appropriate photon stimulus. The mechanisms of sensitivity to light include photoisomerization, photocleavage and photopolymerization[108]. Near-infrared light penetrates deeper into tissues than UV and visible light, and is thus more desirable for tumor treatment. One of the most used light-sensitive lipid is the meta-tetra (hydroxyphenyl) chlorin (mTHPC), which is a component of the approved formulation Foscan® for palliative treatment of advanced squamous cell carcinoma[109]. As another example, an LSL system containing DPPC, 1,2-didecanoyl-sn-glycero-3-phosphocholine (DCPC) and DSPE-PEG (2000) was developed for DOX delivery, where DOX was released after laser exposure at 514 nm to enhance cancer cell death[110]. Gold-coated liposomes were evaluated as both thermo- and light- sensitive systems because of they can absorb near-infrared light irradiation to generate heat, which in turn triggers their leakage[111]. One of such liposome system that was reported in 2014 demonstrated more rapid DOX release than the control groups[112].

1.5 Hypothesis

Based on the foregoing review of the literature, we hypothesize that incorporation of pH-sensitive lipids with long saturated lipid tails can improve the anticancer activities of stealth liposomes. Accordingly, a series of new lipids carrying a pH-sensitive conformational switch are proposed and prepared. The corresponding PEGylated pH-sensitive liposomes (fliposomes) are prepared as an anticancer drug delivery system to deliver doxorubicin. The proposed fliposomes are characterized in both 2D monolayer cancer cells and in 3D MCS of cancer cells in culture.

Chapter 2: Design of pH-Sensitive Lipids with a Conformational Switch to Improve the Anticancer Activities of their Liposome Formulations

2.1 Introduction: Strategies of pH-triggered Release Liposomes

pH-sensitive liposomes are designed to release the encapsulated cargo in response to the pH change in the surrounding. It is well known that tumors carry lower pH than normal tissues because of their lower level of oxygen and hence higher level of glycolysis from anaerobic metabolism. It is reported the pH in tumors ranges from 5.7 to 7.8 compared to the pH around 7.4 in most other tissues[113, 114]. Furthermore, at subcellular level the pH in endosomes and lysosomes can reach as low as 4.5-5.5[115]. This variety of pH provides a great opportunity in developing delivery systems that are sensitive to pH changes to achieve a better therapeutic efficiency against cancer.

Various strategies for constructing pH-sensitive liposomes have been reported. Their mechanisms of triggered release mainly depend upon acid-induced destabilization of lipid bilayers. Most pH-sensitive liposomes fall into four categories based on their components and mechanism[95]. The first category uses a combination of polymorphic lipids and unsaturated phosphatidylethanolamine (PE), such as diacetylenic-phosphatidyl-ethanolamine (DAPE), palmitoyl-oleoyl-phosphatidyl-ethanolamine (POPE) and dioleoyl-phosphatidyl-ethanolamine (DOPE)[116]. At lowered pH the anionic headgroups of the polymorphic lipids become protonated and decrease in size, which then destabilizes the liposome[117]. The second category of pH-sensitive liposomes contain “cage” lipid derivatives of PE or annular lipid with alkyl ether[118]. Such liposomes can reversibly form non-bilayer phase that releases the encapsulated liposome contents. The third category of liposomes contain synthetic fusogenic

peptides or proteins. The pH-sensitive peptides or proteins, such as GALA, are stable at neutral pH, but can promote the fusion between the liposome bilayer and cell membrane at lowered pH[119]. The fourth category of pH-sensitive liposomes are constructed with pH-sensitive polymers. The commonly used polymers for this purpose include poly (alkyl acrylic acid)s, succinylated PEG, and N-isopropylacrylamide (NIPAM) copolymers[120], which can interact with the lipid membranes in response to pH stimulation to induce the fusion between liposomes and endosomes[121].

Many applications of pH-sensitive liposomes have been reported to deliver various cargo molecules to different target sites (Figure 2.1).

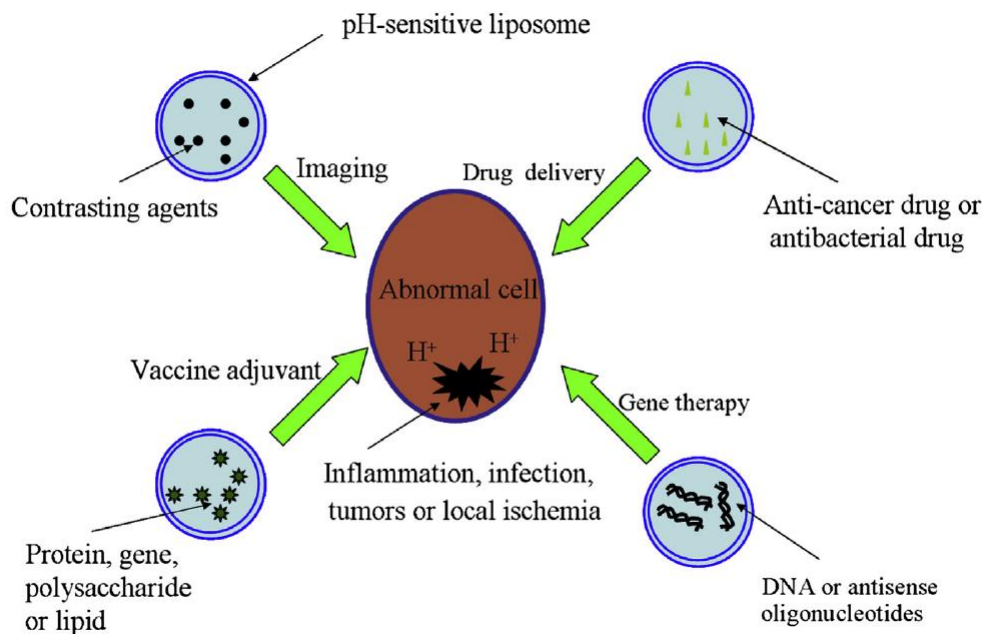


Figure 2.1. Clinical applications of pH-sensitive liposomes[95]

2.2 Design of pH-sensitive Lipids with a Conformational Switch

Another strategy to render liposomes pH-sensitive has been reported by our group and collaborators[122, 123]. A pH-sensitive lipid was developed with a trans-2-aminocyclohexanol ring that undergoes a conformational switch upon protonation. This conformational switch can perturb the lipid bilayer to release the liposome content (Figure 2.2). The lipids with this kind of conformational switch are named “flipids” and the liposomes containing the flipids are called “fliposomes”[123-125]. Flipids with different head groups and hydrocarbon tails were designed and synthesized. The pH-sensitivity of fliposomes were evaluated and the conformational switch of the flipids in response to the pH change was verified by NMR titration. In this study, a series of flipids with saturated long hydrocarbon tails and different head groups of estimated pKa of 2.6 – 8.5 are designed and synthesized.

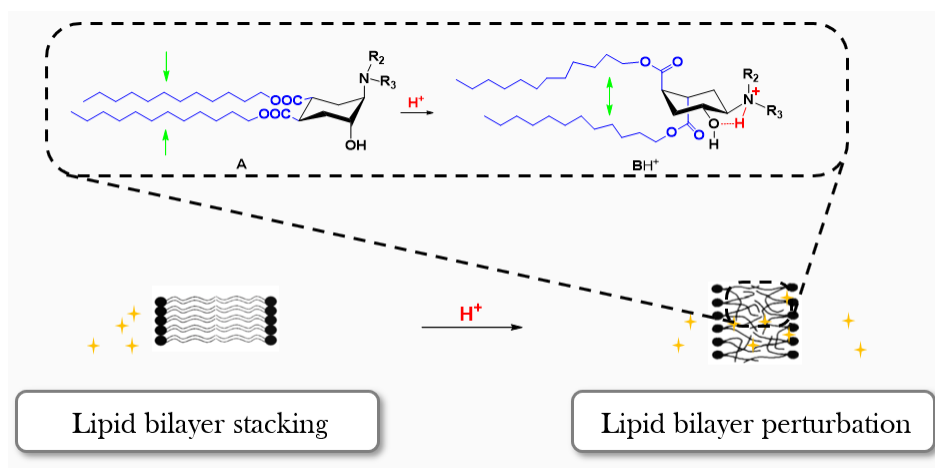
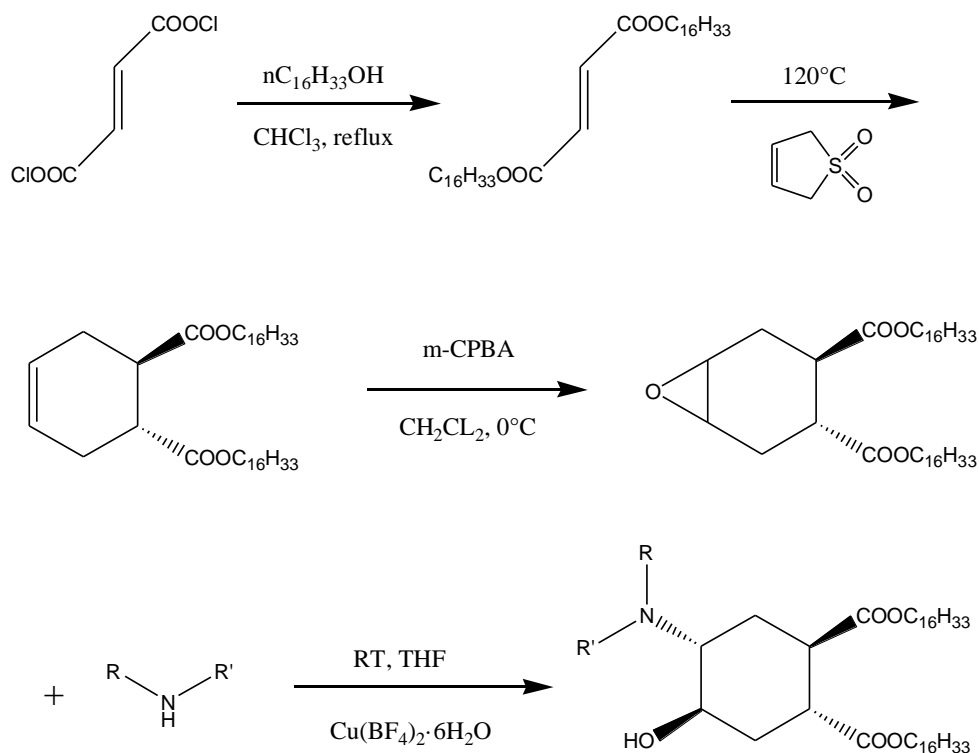


Figure 2.2. Perturbation of lipid bilayer by an acid-induced conformational switch

2.3 Materials and Methods

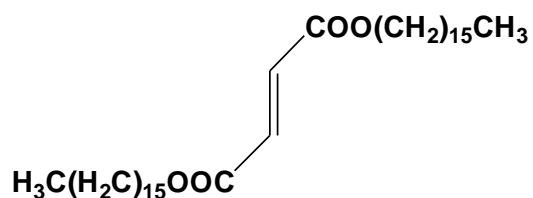
2.3.1 Materials. Fumaryl chloride, 1-hexadecanol, Butadiene sulfone, Hydroquinone, Azetidine, Pyrrolidine and Ethylamine were purchased from Sigma-Aldrich. *meta*-Chloroperoxybenzoic acid (m-CPBA), 2,2,2-trifluoroethylamine, morpholine, 3-aminopropionitrile, copper (II) tetrafluoroborate were purchased from Thermo Fisher Scientific. All organic solvents were purchased from Sigma, Fisher or VWR.

2.3.2 Synthesis of pH-sensitive lipids with a conformational switch (flipids). *Trans*-2-aminocyclohexanol-based amphiphiles were synthesized using the previously described method[126] (Scheme 2.1). ¹H-NMR were acquired with a JEOL ECA 600 MHz FT-NMR spectrometer (Redding, CA, USA). High resolution mass spectra were acquired by with a JEOL Accu-TOF LC time of flight mass spectrometer (JEOL, Peabody, MA, USA) equipped with a DART ion source (IonSense, Saugus, MA, USA).



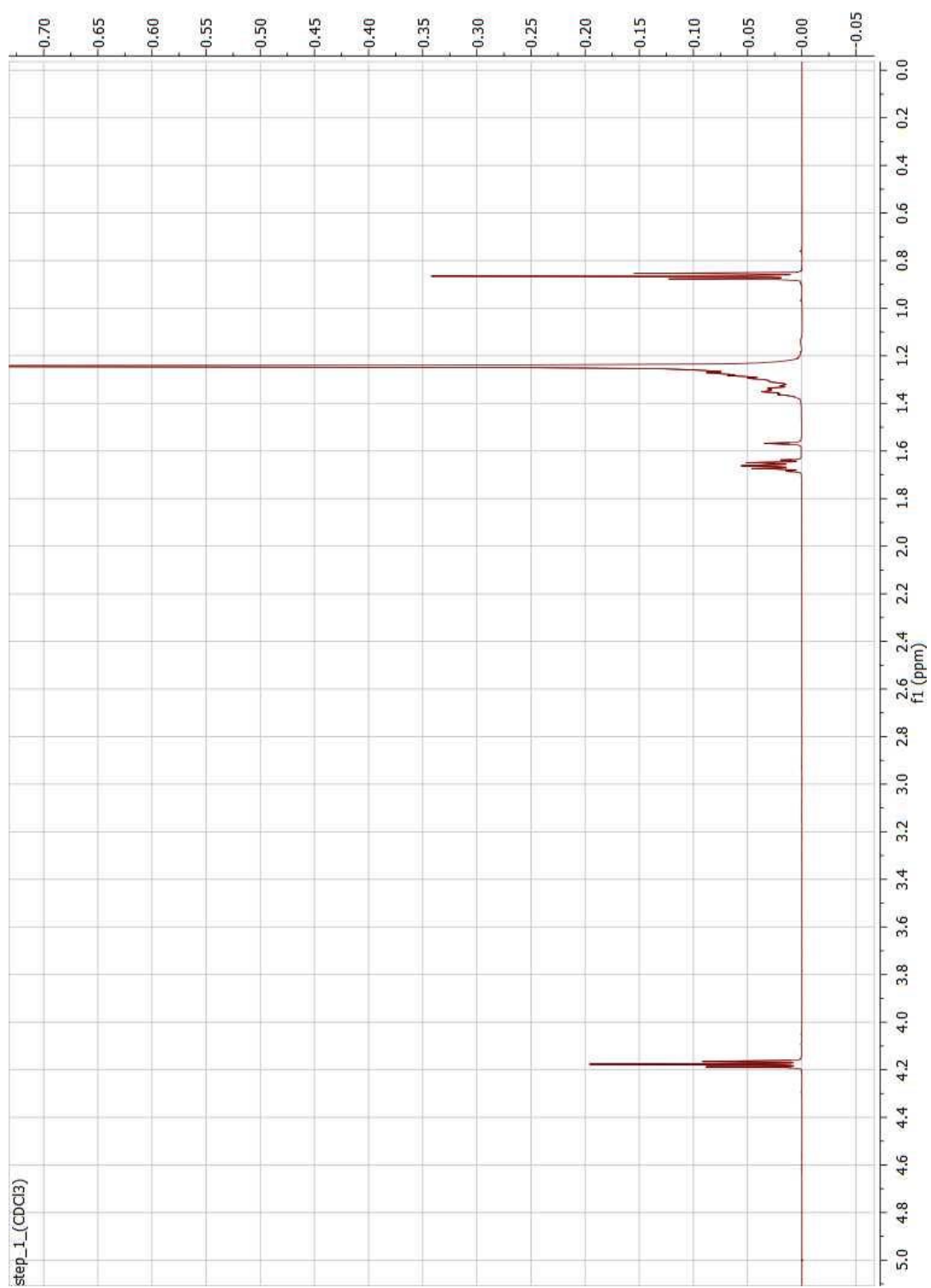
Scheme 2.1. Synthesis of pH-sensitive lipids with a conformational switch[126]

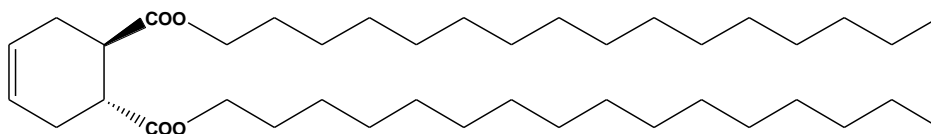
Dihexadecyl fumarate:



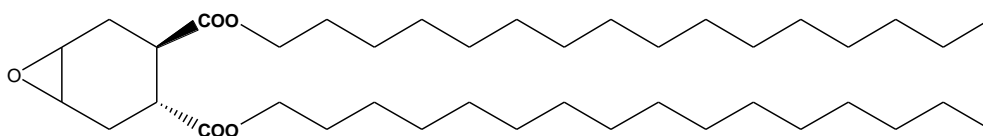
Fumaryl chloride (3.22g, 20 mmol) was refluxed for 12 h with 10.2 g (42 mmol) of 1-hexadecanol in 30 ml of dry chloroform. The reaction mixture was diluted with 60 mL of CH_2Cl_2 and washed with 2×20 mL NaOH (5% sol). The organic layer was washed with 2×10 mL of hydrochloric acid (5% sol), 10 mL of brine, dried over CaCl_2 and concentrated in vacuo. The residue was purified by column chromatography (Hexane: EtOAc, 60:1) to yield 6.7g (60%)

of oily solid. Rf: 0.33 (Hexane: EtOAc, 60:1). ^1H NMR (600 MHz, CDCl_3): δ 0.86 (t, $J = 6.9$ Hz, 6H, CH_3), 1.19-1.37 (m, 52H, CH_2 , hexadecyl), 1.65 (quin, $J = 6.7$ Hz, 4H, CH_2 , hexadecyl), 4.17 (t, $J = 6.7$ Hz, 4H, COOCH_2), 6.824 (s, 2H, $\text{HC}=\text{CH}$). HRMS: $\text{C}_{36}\text{H}_{68}\text{O}_4$ requires m/z $[\text{M}+\text{H}]^+$ 565.5196, found 565.5135.



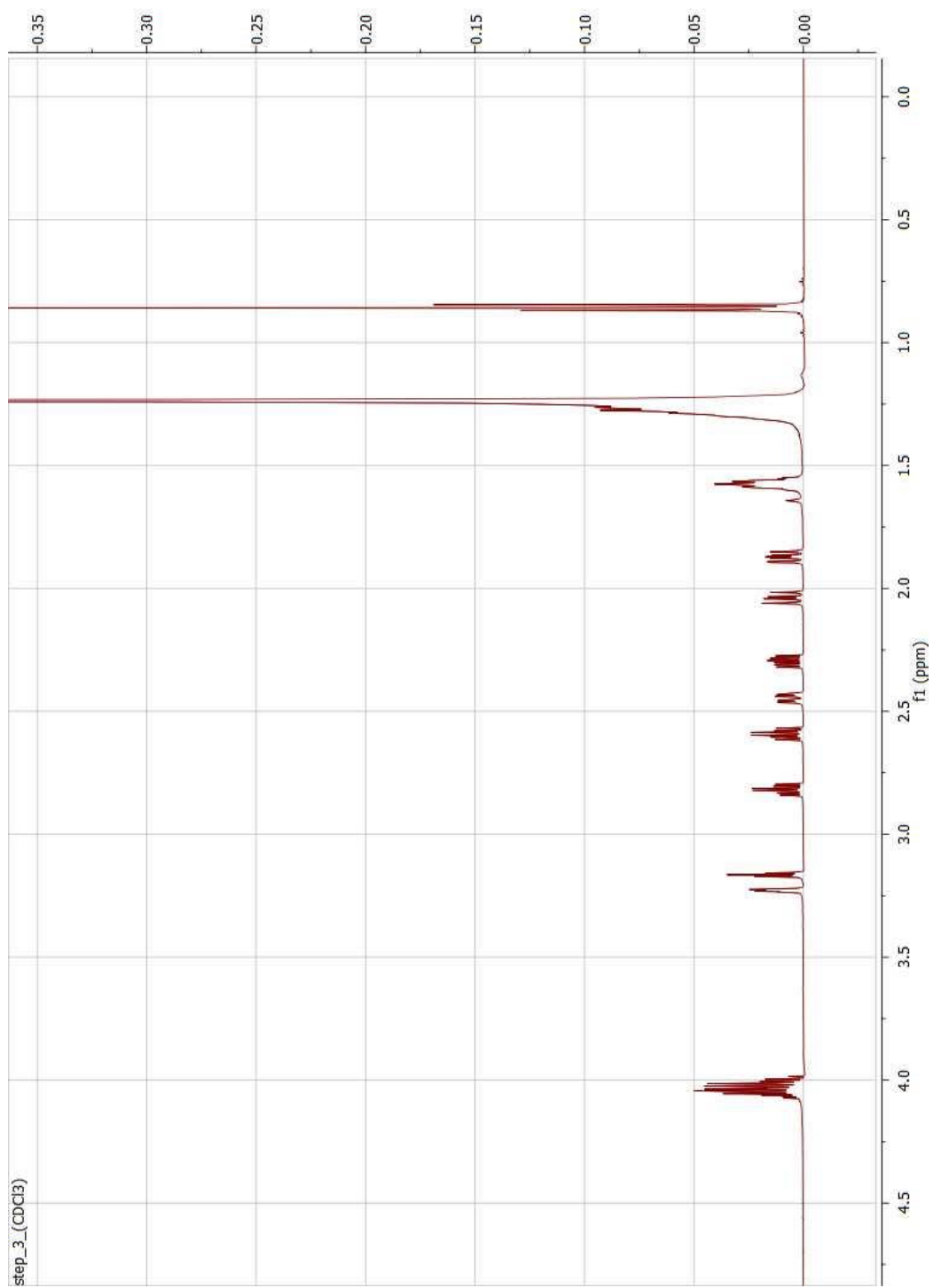
Dihexadecyl 4-cyclohexene-trans-1,2-dicarboxylate:

Butadiene sulfone (2.0 g, 17.3 mmol, 50% excess), dihexadecyl fumarate (6.5g, 11.5 mmol) and hydroquinone (86 mg, 0.8 mmol) were mixed and diluted with 20 mL of isopropyl alcohol. The mixture was heated in a sealed reactor at 120°C for 48 h. After cooling down, the reaction mixture was combined with, 120 mL of H₂O and 90 mL of CHCl₃ and then neutralized by stirring with crystalline NaHCO₃ (~35g). The organic layer was separated, washed with 2 × 40 mL of water and 60 mL of brine, dried over CaCl₂ and concentrated in vacuo. The residue was further purified by column chromatography (Hexane: EtOAc, 60:1) to yield 5.3g (71%) of white solid. Rf: 0.36 (Hexane: EtOAc, 40:1). ¹H NMR (600 MHz, CDCl₃): δ 0.86 (t, *J* = 7.1 Hz, 6H, CH₃), 1.19-1.37 (m, 52H, CH₂, hexadecyl), 1.59 (br. quin, *J* = 6.8 Hz, 4H, CH₂, hexadecyl), 2.11-2.21 (m, 2H, H3a+H6a), 2.36-2.46 (m, 2H, H3e+H6e), 2.84 (m, 2H, H1+H2), 4.055 (m, 4H, COOCH₂), 5.67 (m, 2H, H4+H5). HRMS: C₄₀H₇₄O₄ requires *m/z* [M+H]⁺ 619.5665, found 619.5644.

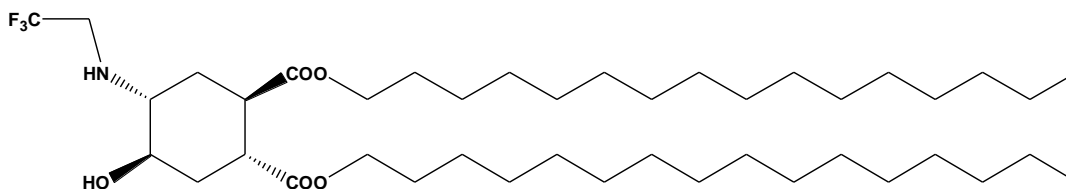
Dihexadecyl 7-oxabicyclo[4.1.0]heptane-trans-3,4-dicarboxylate:

Dihexadecyl 4-cyclohexene-trans-1,2-dicarboxylate (5 g, 8 mmol) was dissolved in 15 mL of dry CH₂Cl₂, and m-CPBA (3 g of 70 % tech. grade, 12 mmol) was added in small portions at 0 °C while stirring. The reaction mixture was kept at this temperature for 14 h. After

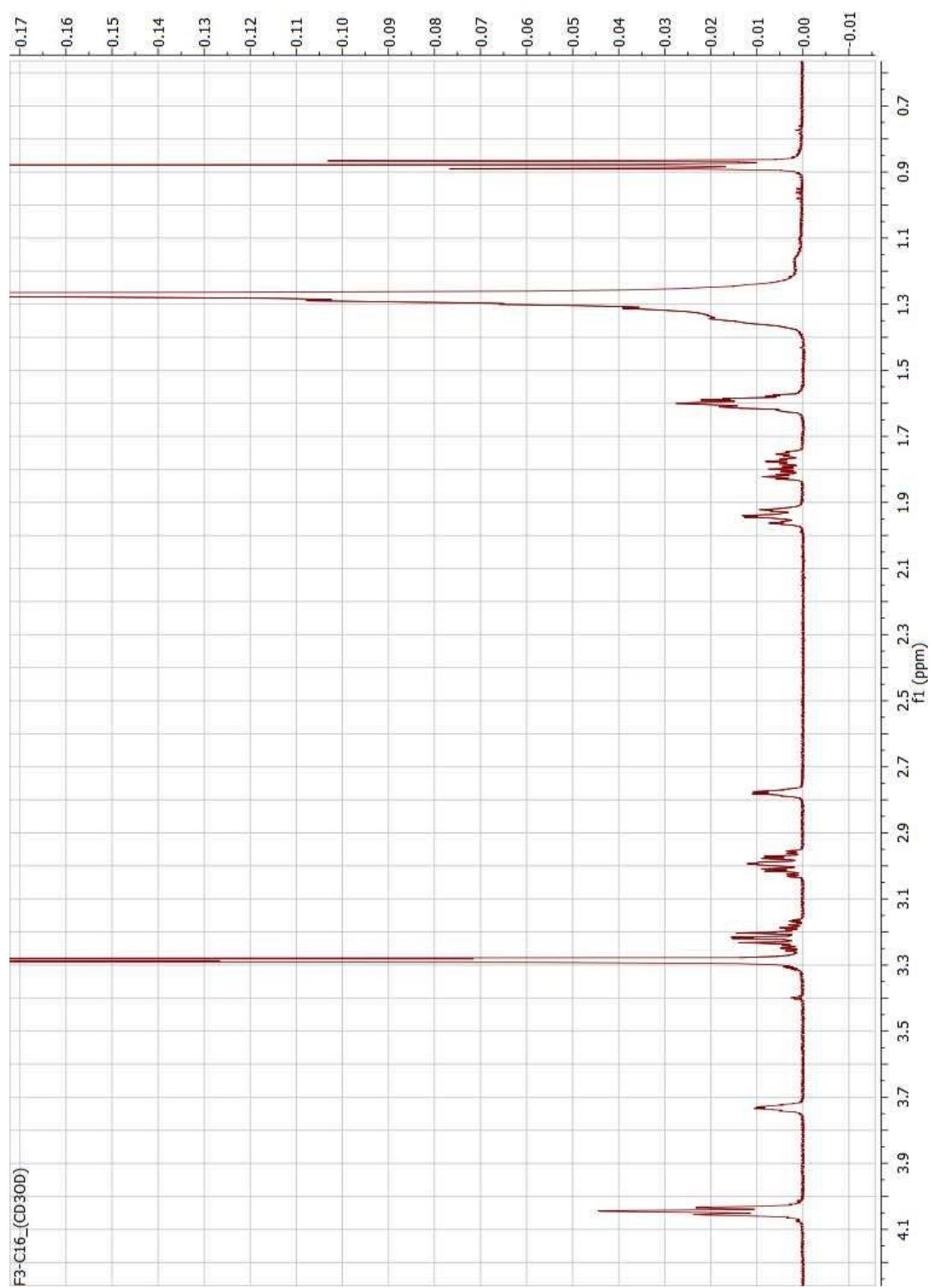
the consumption of the starting material (TLC, Hexane: EtOAc, 20:1), 30 mL of chloroform was added followed by 40 mL of saturated Na₂CO₃. The mixture was stirred for 30 min and then the organic phase was washed with 4 x 20 mL of Na₂CO₃. The organic layer was dried for 12 h over anhydrous Na₂SO₄ and concentrated in vacuo. The residue was isolated as a white solid by column chromatography (Hexane: EtOAc, 12:1): yield 4.2 g (82 %). Rf: 0.31 (Hexane: EtOAc, 8:1). ¹H NMR (600 MHz, CDCl₃): δ 0.854 (t, *J* = 7.0 Hz, 6H, CH₃), 1.17-1.37 (m, 52H, CH₂, hexadecyl), 1.57 (m, 4H, CH₂, hexadecyl), 1.87 (ddd, *J* = 14.9, 10.8, 2.1 Hz, 1H, H5a), 2.034 (dd, *J* = 15.5, 10.8 Hz, 1H, H2a), 2.29 (ddd, *J* = 15.5, 6.6, 4.8 Hz, 1H, H2e), 2.44 (ddd, *J* = 14.9, 4.8, 1.8 Hz, 1H, H5e), 2.59 (dt, *J* = 6.6, 10.7 Hz, 1H, H3), 2.814 (dt, *J* = 4.9, 10.6 Hz, 1H, H4), 3.16 (t, *J* = 4.3 Hz, 1H, H1), 3.23 (dt, *J* = 3.8, 1.9 Hz, 1H, H6), 4.03 (m, 4H, COOCH₂). HRMS: C₄₀H₇₄O₅ requires *m/z* [M+H]⁺ 635.5615, found 635.5548.



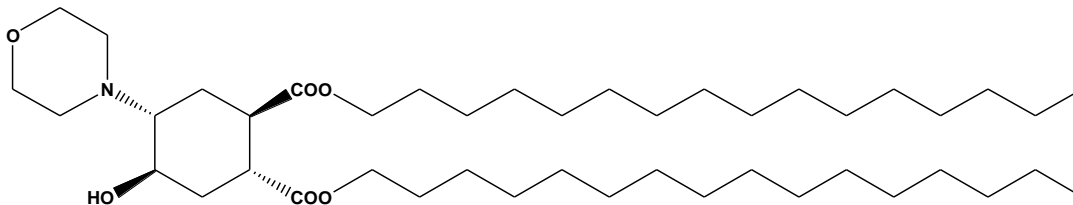
Dihexadecyl cis-4-hydroxy-trans-5-(2,2,2-trifluoroethylamino)cyclohexane-trans-1,2-dicarboxylate:



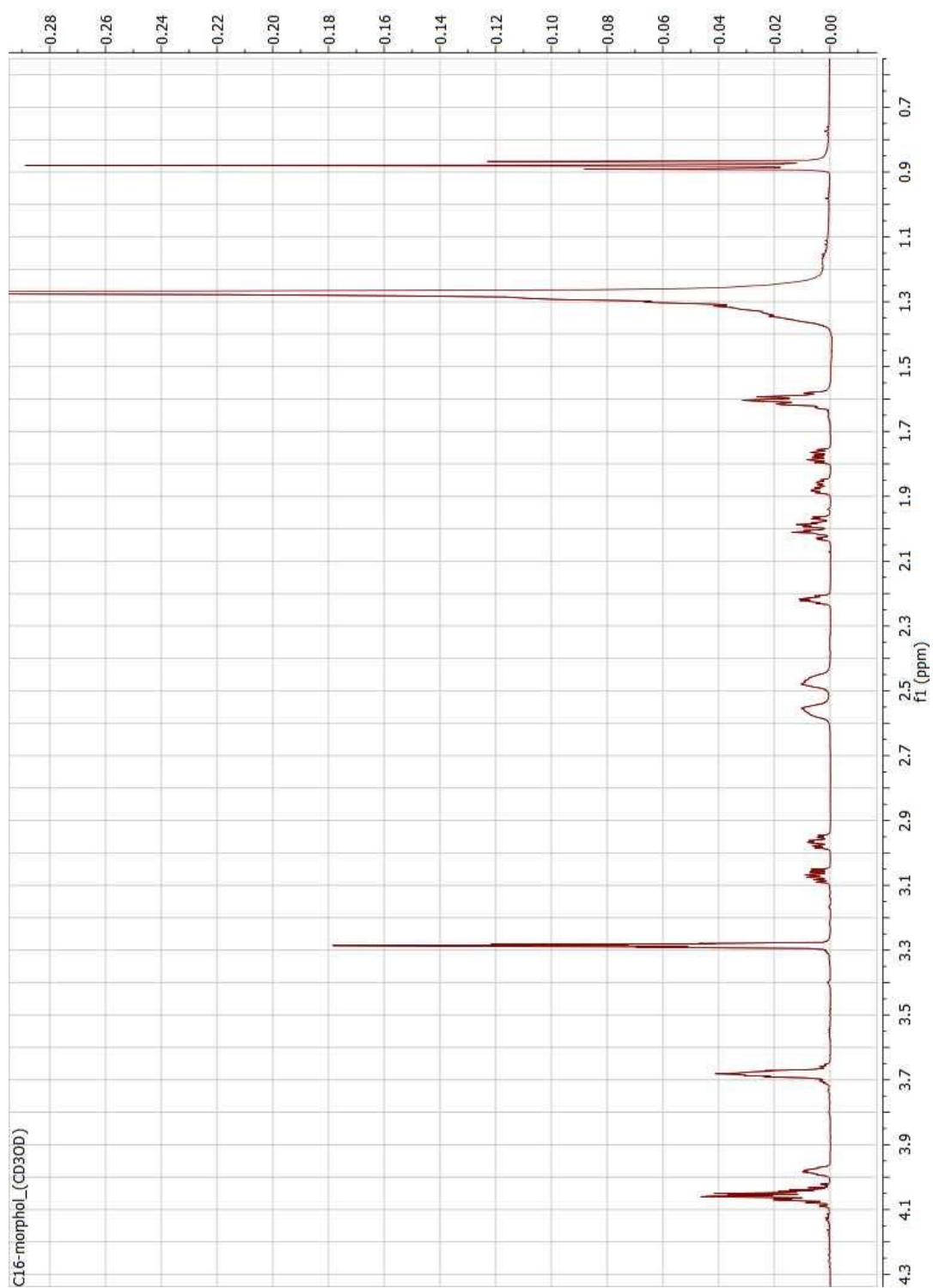
Dihexadecyl 7-oxabicyclo[4.1.0]heptane-trans-3,4-dicarboxylate (0.45 g, 0.71 mmol) and 2,2,2-Trifluoroethylamine (0.56 mL, 7.1 mmol) were stirred for 3 days with the catalyst Copper(II) tetrafluoroborate hexahydrate (24.52 mg, 0.071 mmol) at room temperature in 2 mL of THF. The reaction mixture was concentrated on a rotary evaporator. The residue was isolated as a white solid by column chromatography (Hexane: EtOAc, 5:1): yield 0.34 g (66.1%). Rf: 0.25 (Hexane: EtOAc, 4:1). $^1\text{H NMR}$ (600 MHz, CD_3OD): δ 0.87 (t, $J = 7$ Hz, 6H, CH_3), 1.20-1.39 (m, 52H, CH_2 , hexadecyl), 1.6 (m, 4H, CH_2 , hexadecyl), 1.78 (dt, $J = 13.7, 4.1$ Hz, 1H, H6e), 1.82 (dt, $J = 13.7, 4.1$ Hz, 1H, H3e), 1.94 (m, 1H, H6a), 1.96 (m, 1H, H3a), 2.78 (q, $J = 3.8$ Hz, 1H, H5), 2.99 (dt, $J = 3.6, 9.6$ Hz, 1H, H1), 3.01 (dt, $J = 4, 9.8$ Hz, 1H, H2), 3.22 (m, 2H, CH_2N), 3.73 (dt, $J = 2.9, 4.6$ Hz, 1H, H4), 4.05 (m, 4H, COOCH_2). HRMS: $\text{C}_{42}\text{H}_{78}\text{F}_3\text{NO}_5$ requires m/z $[\text{M}+\text{H}]^+$ 734.5832, found 734.5798.



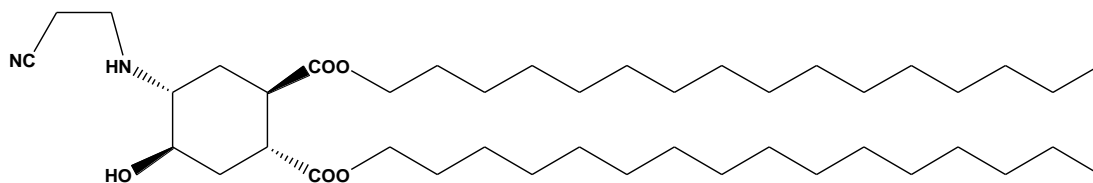
Dihexadecyl cis-4-hydroxy-trans-5-morpholinocyclohexane-trans-1,2-dicarboxylate[127]:



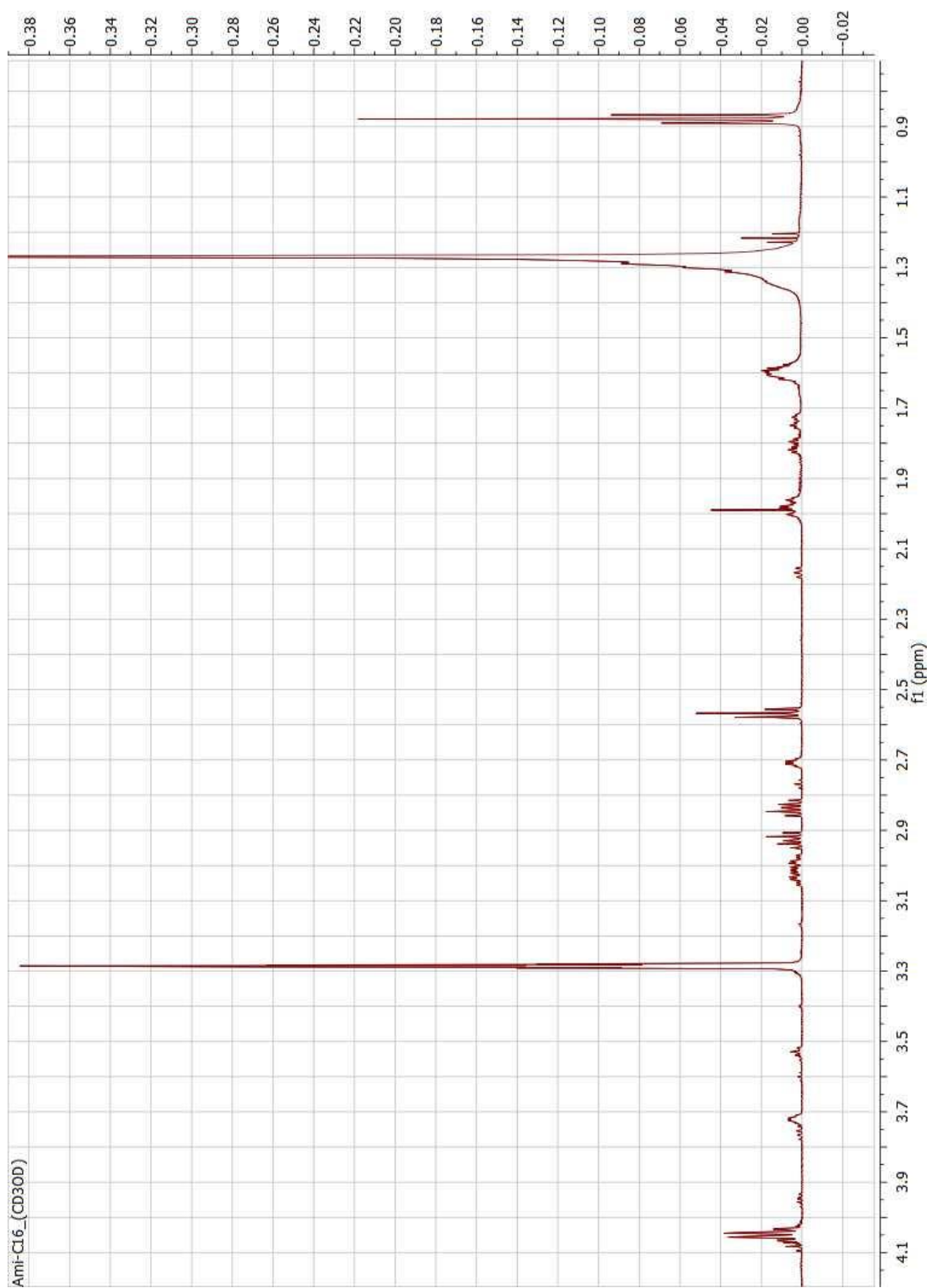
Dihexadecyl 7-oxabicyclo[4.1.0]heptane-trans-3,4-dicarboxylate (0.45 g, 0.71 mmol) and morpholine (0.62 mL, 7.1 mmol) were stirred for 2 days with the catalyst Copper(II) tetrafluoroborate hexahydrate (24.52 mg, 0.071 mmol) at room temperature in 2 mL of THF. The reaction mixture was concentrated on a rotary evaporator. The residue was isolated as a white solid by column chromatography (Hexane: EtOAc, 5:1): yield 0.41 g (79.4%). Rf: 0.35 (Hexane: EtOAc, 3:1). $^1\text{H NMR}$ (600 MHz, CD_3OD): δ 0.89 (t, $J = 7.1$ Hz, 6H, CH_3), 1.23-1.40 (m, 52H, CH_2 , hexadecyl), 1.62 (br. quin, $J = 6.9$ Hz, 4H, CH_2 , hexadecyl), 1.79 (ddd, $J = 13.4$, 5.0, 4.8 Hz, 1H, H3e), 1.89 (ddd, $J = 14.1$, 5.4, 3.9 Hz, 1H, H6e), 2.00 (m, 1H, H6a), 2.02 (m, 1H, H3a), 2.23 (dt, $J = 3.0$, 5.3 Hz, 1H, H5), 2.49 (m, 2H, CH_2N , morpholyl), 2.57 (m, 2H, CH_2N , morpholyl), 2.98 (dt, $J = 3.6$, 9.5 Hz, 1H, H1), 3.08 (dt, $J = 4.4$, 9.5 Hz, 1H, H2), 3.70 (m, 4H, OCH_2 , morpholyl), 4.00 (dt, $J = 2.8$, 5.2 Hz, 1H, H4), 4.07 (m, 4H, COOCH_2). HRMS: $\text{C}_{44}\text{H}_{83}\text{NO}_6$ requires m/z $[\text{M}+\text{H}]^+$ 722.6299, found 722.6113.



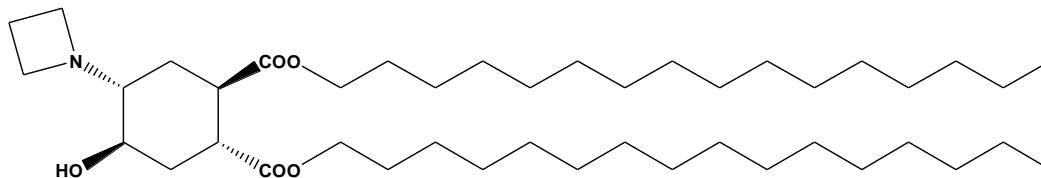
Dihexadecyl cis-4-hydroxy-trans-5-(2-cyanoethylamino)cyclohexane-trans-1,2-dicarboxylate:



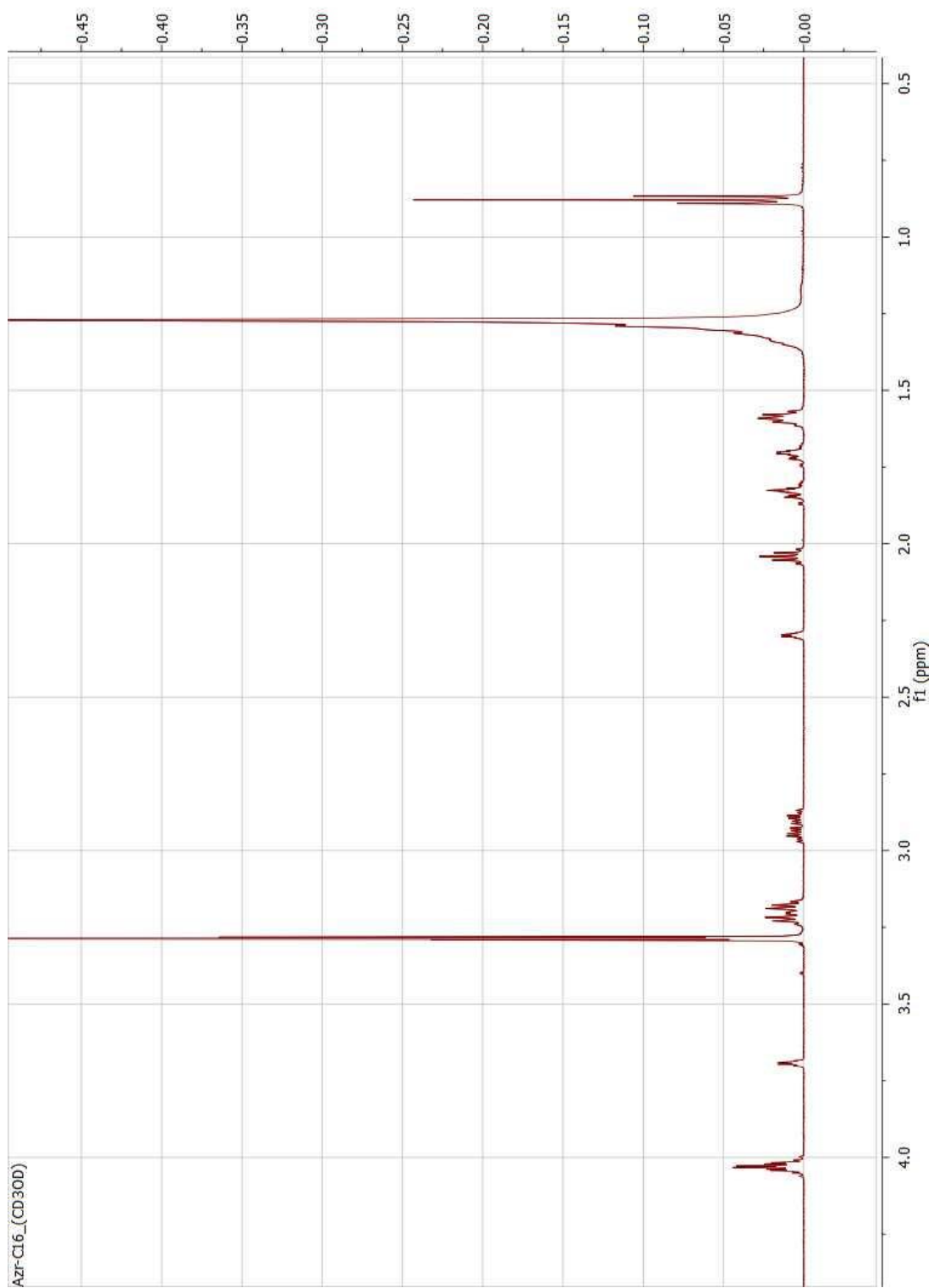
Dihexadecyl 7-oxabicyclo[4.1.0]heptane-trans-3,4-dicarboxylate (0.45 g, 0.71 mmol) and 3-Aminopropionitrile (0.52 mL, 7.1 mmol) were stirred for 3 days with the catalyst Copper(II) tetrafluoroborate hexahydrate (24.52 mg, 0.071 mmol) at room temperature in 2 mL of THF. The reaction mixture was concentrated on a rotary evaporator. The residue was isolated as a white solid by column chromatography (Hexane: EtOAc, 3:1): yield 0.36 g (71.2%). R_f: 0.31 (Hexane: EtOAc, 3:1). ¹H NMR (600 MHz, CD₃OD): δ 0.88 (t, *J* = 7 Hz, 6H, CH₃), 1.20-1.42 (m, 52H, CH₂, hexadecyl), 1.6 (m, 4H, CH₂, hexadecyl), 1.75 (dt, *J* = 13.9, 4.6 Hz, 1H, H_{6a}), 1.82 (dt, *J* = 11.8, 4.3 Hz, 1H, H_{3a}), 1.98 (m, 2H, H_{6e}+H_{3e}), 1.99 (s, 1H, NH), 2.57 (m, 3H, H₅+CH₂CN), 2.72 (q, *J* = 4.3 Hz, 1H, H₁), 2.85 (dt, *J* = 12.2, 6.9 Hz, 1H, CH₂N), 2.94 (dt, *J* = 14.3, 6.8 Hz, 1H, CH₂N), 2.99 (td, *J* = 10.3, 3.7 Hz, 1H, H₂), 3.04 (td, *J* = 9.4, 4.3 Hz, 1H, H₄), 4.05 (m, 4H, COOCH₂). HRMS: C₄₃H₈₀N₂O₅ requires *m/z* [M+H]⁺ 705.6067, found 705.6085.



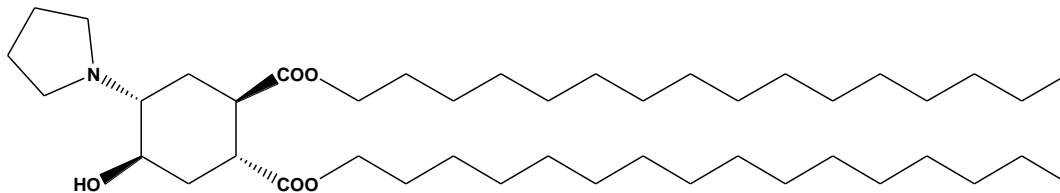
Dihexadecyl cis-4-hydroxy-trans-5-(azetidine-1-yl)cyclohexane-trans-1,2-dicarboxylate:



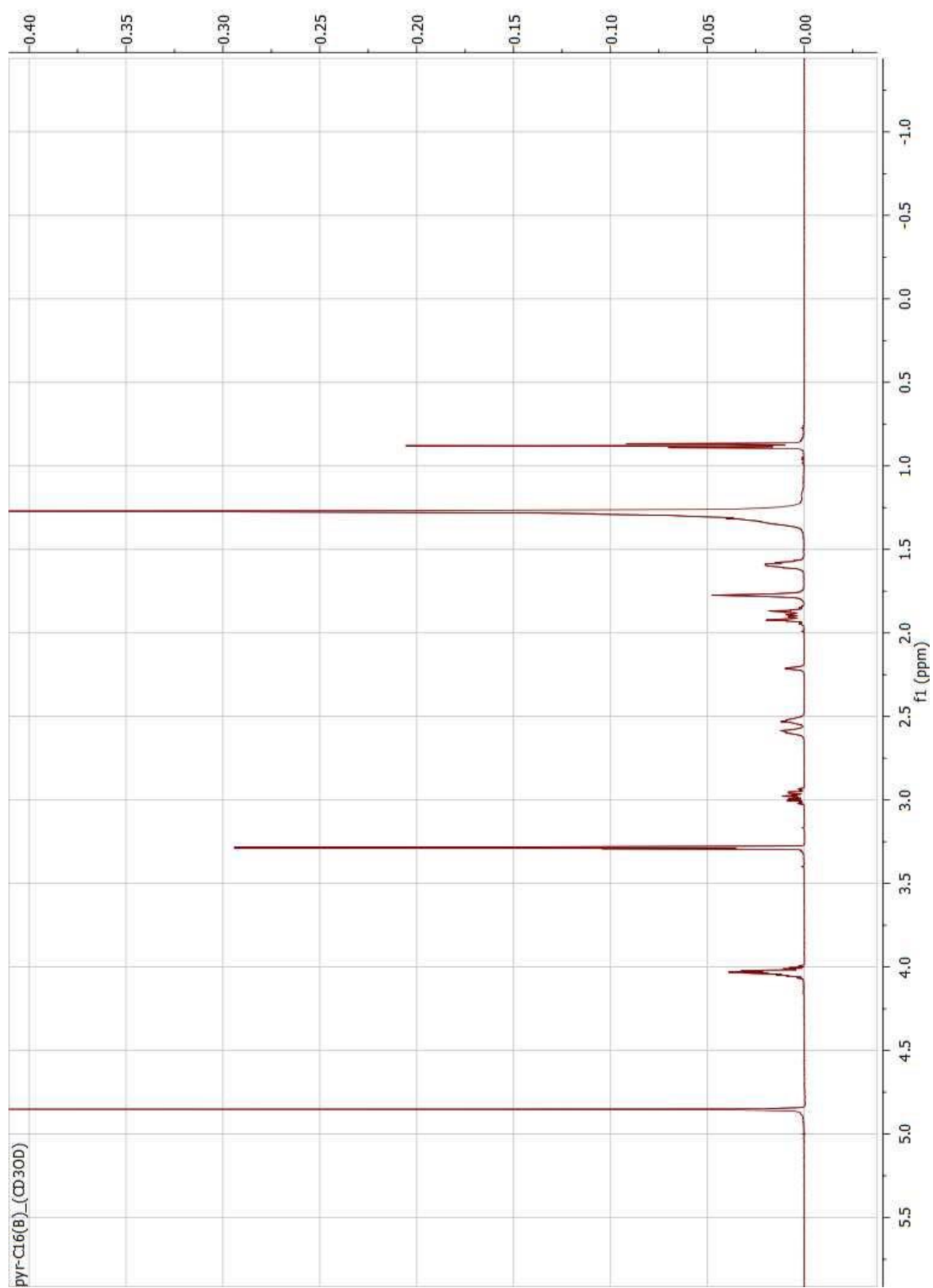
Dihexadecyl 7-oxabicyclo[4.1.0]heptane-trans-3,4-dicarboxylate (0.45 g, 0.71 mmol) and azetidine (0.48 mL, 7.1 mmol) were stirred for 3 days with the catalyst Copper(II) tetrafluoroborate hexahydrate (24.52 mg, 0.071 mmol) at room temperature in 2 mL of THF. The reaction mixture was concentrated on a rotary evaporator. The residue was isolated as a white solid by column chromatography (Hexane: EtOAc, 5:1): yield 0.39 g (78.8%). Rf: 0.35 (Hexane: EtOAc, 4:1). $^1\text{H NMR}$ (600 MHz, CD_3OD): δ 0.88 (t, $J = 7$ Hz, 6H, CH_3), 1.20-1.38 (m, 52H, CH_2 , hexadecyl), 1.6 (br. quin, $J = 7$ Hz, 4H, CH_2 , hexadecyl), 1.71 (m, 2H, $\text{H}_{6e}+\text{H}_{3e}$), 1.83 (m, 2H, $\text{H}_{6a}+\text{H}_{3a}$), 2.04 (quin, $J = 7$ Hz, 2H, $\text{CH}_2\text{CH}_2\text{N}$), 2.31 (dt, $J = 3.4, 3.3$ Hz, 1H, H_5), 2.89 (td, $J = 10.3, 5$ Hz, 1H, H_1), 2.95 (td, $J = 10.8, 5.3$ Hz, 1H, H_2), 3.21 (ddd, $J = 6.6, 13.2, 23.6$ Hz, 4H, $\text{CH}_2\text{CH}_2\text{N}$), 3.70 (dt, $J = 3.4, 3.2$ Hz, 1H, H_4), 4.03 (m, 4H, COOCH_2). HRMS: $\text{C}_{43}\text{H}_{81}\text{NO}_5$ requires m/z $[\text{M}+\text{H}]^+$ 692.6114, found 692.6121.

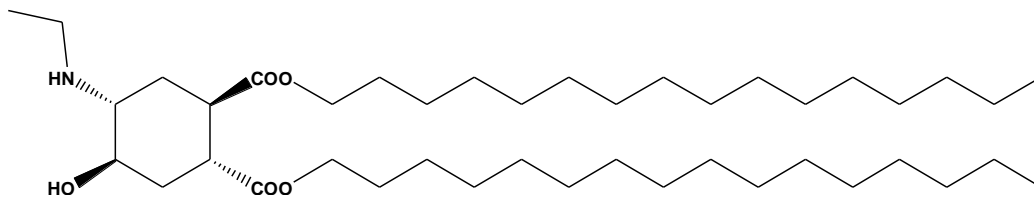


Dihexadecyl cis-4-hydroxy-trans-5-(pyrrolidine-1-yl)cyclohexane-trans-1,2-dicarboxylate:

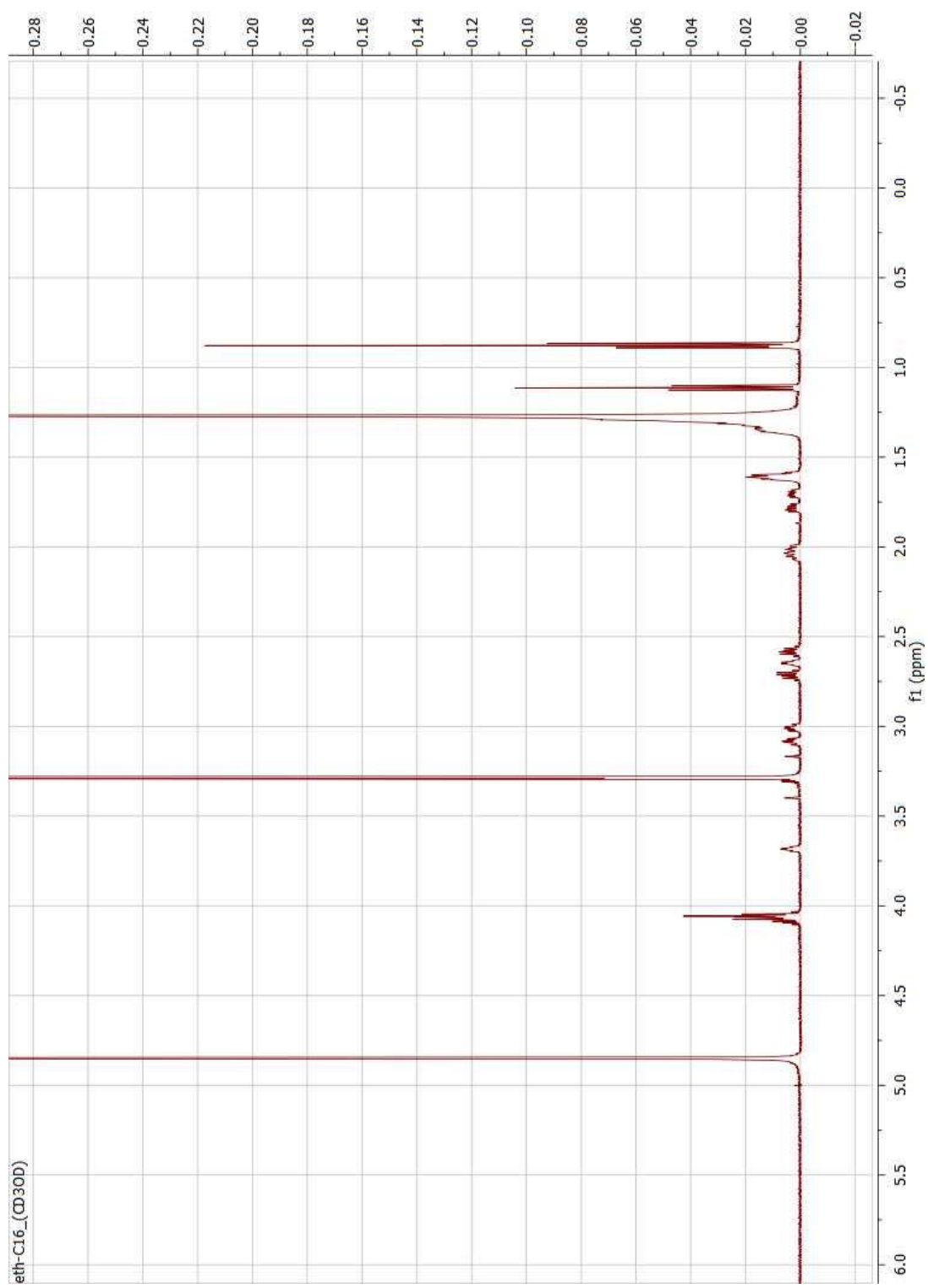


Dihexadecyl 7-oxabicyclo[4.1.0]heptane-trans-3,4-dicarboxylate (0.45 g, 0.71 mmol) and pyrrolidine (0.59 mL, 7.1 mmol) were stirred for 4 days with the catalyst Copper(II) tetrafluoroborate hexahydrate (24.52 mg, 0.071 mmol) at room temperature in 2 mL of THF. The reaction mixture was concentrated on a rotary evaporator. The residue was isolated as a white solid by column chromatography (Hexane: EtOAc, 5:1): yield 0.28 g (56.2%). Rf: 0.32 (Hexane: EtOAc, 4:1). ¹H NMR (600 MHz, CD₃OD): δ 0.88 (t, *J* = 7.1 Hz, 6H, CH₃), 1.20-1.40 (m, 52H, CH₂, hexadecyl), 1.6 (m, 4H, CH₂, hexadecyl), 1.77 (quin, *J* = 2.8 Hz, 4H, CH₂, CH₂CH₂N), 1.87 (m, 2H, H_{6e}+H_{3e}), 1.93 (m, 2H, H_{6a}+H_{3a}), 2.21 (m, 1H, H₅), 2.53 (m, 2H, CH₂CH₂N), 2.60 (m, 2H, CH₂CH₂N), 2.95 (td, *J* = 10.4, 4.4 Hz, 1H, H₁), 3.01 (td, *J* = 11.0, 5.1 Hz, 1H, H₂), 4.01 (m, 1H, H₄), 4.03 (m, 4H, COOCH₂). HRMS: C₄₄H₈₃NO₅ requires *m/z* [M+H]⁺ 706.6271, found 706.6276.



Dihexadecyl cis-4-hydroxy-trans-5-(ethylamino)cyclohexane-trans-1,2-dicarboxylate:

Dihexadecyl 7-oxabicyclo[4.1.0]heptane-trans-3,4-dicarboxylate (0.45 g, 0.71 mmol) and ethylamine (0.46 mL, 7.1 mmol) were stirred for 4 days with the catalyst Copper(II) tetrafluoroborate hexahydrate (24.52 mg, 0.071 mmol) at room temperature in 2 mL of THF. The reaction mixture was concentrated on a rotary evaporator. The residue was isolated as a white solid by column chromatography (Hexane: EtOAc, 1:1): yield 0.3 g (62.7%). Rf: 0.21 (Hexane: EtOAc, 2:3). ¹H NMR (600 MHz, CD₃OD): δ 0.88 (t, *J* = 7.0 Hz, 6H, CH₃), 1.12 (t, *J* = 7.1 Hz, 3H, CH₃, ethylamino), 1.21-1.40 (m, 52H, CH₂, hexadecyl), 1.61 (m, 4H, CH₂, hexadecyl), 1.71 (ddd, *J* = 13.5, 6.0, 4.1 Hz, 1H, H_{6e}), 1.78 (ddd, *J* = 13.8, 6.4, 4.6 Hz, 1H, H_{3e}), 2.01 (m, 1H, H_{3a}), 2.05 (m, 1H, H_{6a}), 2.58 (dq, *J* = 11.4, 7.0 Hz, 1H, CH₂N), 2.66 (dt, *J* = 4.0, 5.7 Hz, 1H, H₅), 2.72 (dq, *J* = 11.5, 7.2 Hz, 1H, CH₂N), 3.01 (td, *J* = 8.8, 4.0 Hz, 1H, H₁), 3.08 (td, *J* = 8.6, 4.4 Hz, 1H, H₂), 3.69 (dt, *J* = 2.9, 10.9 Hz, 1H, H₄), 4.05 (m, 4H, COOCH₂). HRMS: C₄₄H₈₃NO₅ requires *m/z* [M+H]⁺ 680.6114, found 680.6105.



2.4 Results and Discussion

The products from each step was confirmed with MS and NMR studies. The final products of each pH-sensitive flipid were sent out to Complete Analysis Laboratories. Inc. (Highland Park, NJ, USA) to perform an elemental analysis (C, H, N). The results are listed in Table 2.1. The accepted deviation of the results from the calculated is 0.4% according to ACS standard[128] which is achieved by all samples.

Table 2.1. Elemental Analysis of C16 flipids

Sample	Calculated C%	Measured C%	Error	Calculated H%	Measured H%	Error	Calculated N%	Measured N%	Error
Eth-C16	74.17	74.06	0.11	12.00	12.11	-0.11	2.06	2.11	-0.05
Pyr-C16	74.84	74.94	-0.10	11.85	12.03	-0.18	1.98	2.24	-0.26
Aze-C16	74.62	74.78	-0.16	11.8	11.94	-0.14	2.02	2.11	-0.09
Ami-C16	73.25	73.39	-0.14	11.44	11.51	-0.07	3.97	4.17	-0.20
Mor-C16	73.18	73.26	-0.08	11.58	11.58	0.00	1.94	2.24	-0.30
Tri-C16	69.04	68.66	0.38	10.78	10.82	-0.04	1.87	2.03	-0.16

One important physicochemical property of the lipids is the phase transition temperature (T_m). It is defined as the temperature required to induce a change in the lipid physical state from the ordered gel phase to the disordered liquid crystalline phase[129]. It has a direct impact on the stability of liposomes where the entrapped material shows low permeability below T_m and an increase of permeability above T_m . There are several factors that directly affect T_m such as the polar head group, acyl chain length, degree of saturation of the hydrocarbon chains and the properties (e.g. ionic strength) of the suspension medium[130]. As the hydrocarbon length of the lipid tail increases, the van der Waals interactions between the lipid molecules get stronger to yield higher T_m . Introducing an unsaturated bond in the hydrocarbon chain decreases the energy

needed to disrupt the lipid tail packing to yield a lower T_m . Sufficient stability in blood circulation at 37°C is the required of a liposome delivery system for clinical applications. Table 2.2 shows five phospholipids with different T_m . From the table we can see that a saturated lipid with at least 16 hydrocarbon chain can be ideal for a liposome formulation in the clinic.

Table 2.2. Transition Temperature of Phospholipids[131]

Lipid	Hydrocarbon length	Unsaturated bond	T_m (°C)
DLPC	12	0	-1
DMPC	14	0	23
DPPC	16	0	41
DSPC	18	0	55
DOPC	18	1	-20

Previous studies showed that the pK_a of flipids were determined by the structure of hydrophilic head groups[122]. To cover the pH range of solid tumor (pH 6.5-7.2) and endosome (5.0-6.5), six amino headgroups were chosen based on the estimated pK_a value from titration curves of previous studies[122, 126]. The structure features of the newly designed flipids under my dissertation studies are summarized in Table 2.3.

Table 2.3. Flipids with Saturated C16 Hydrocarbon Tail and Different Amino Head Groups Designed for Studies for this Dissertation.

Name of flipids	Head Group	Hydrocarbon Tail	Estimated pK_a
Eth-C16	Ethylamine	Saturated C16	8.5
Pyr-C16	Pyrrolidine	Saturated C16	7.6
Aze-C16	Azetidine	Saturated C16	6.8

Ami-C16	Aminopropionitrile	Saturated C16	5.6
Mor-C16	Morpholine	Saturated C16	4.9
Tri-C16	Trifluoroethylamine	Saturated C16	2.6

The chemical synthesis of the designed lipids is summarized in Scheme 2.1. Briefly, Fumaryl chloride was refluxed with 1-hexadecanol in dry chloroform during an alcoholysis reaction. Then the purified product dihexadecyl fumarate was heated with butadiene sulfone in a sealed reactor at 120°C for 48 h. After purification the resulted compound was mixed with m-CPBA in dry CH₂Cl₂ at 0°C under stirring. The reaction was completed to yield epoxide in 14 h and the product was purified. Lastly, the designed lipids were obtained by mixing epoxide with different amines and the catalyst Copper (II) tetrafluoroborate hexahydrate for 2 – 4 days. The synthesis is based on the previously reported syntheses of similar lipids [122, 124] but carries an important modification of employing a catalyst in the epoxide ring-opening reaction in the last step. This nucleophilic addition reaction under previously reported conditions without the catalyst was very slow with low yields on the epoxides with C14 hydrocarbon chains. The reaction was found to be even slower on the epoxides with longer hydrocarbon chains. For example, Ditetradecyl cis-4-hydroxy-trans-5-morpholinocyclohexane-trans-1,2-dicarboxylate (C14) was prepared at a 59% yield after 5 days stirring the epoxide with morpholine in room temperature while the dihexadecyl cis-4-hydroxy-trans-5-morpholinocyclohexane-trans-1,2-dicarboxylate (C16) was made only at a 21.1% yield after 5 days reaction and 39.8% yield after 10 days reaction at room temperature. It has been reported that Copper (II) tetrafluoroborate can be used as a catalyst for epoxide ring-opening reactions to boost the yield and reduce the reaction time [127]. Including this catalyst at an appropriate molar ratio (epoxide: amine: catalyst = 1 : 10 : 0.1) resulted in a much higher yield of 76.2% after 2 days of reaction at room

temperature for dihexadecyl cis-4-hydroxy-trans-5-morpholinocyclohexane-trans-1,2-dicarboxylate (C16).

The yields of six designed flipids in the last step of nucleophilic addition are summarized in Table 2.4. All the flipids were successfully synthesized with relatively high yields within 2 – 4 days.

Table 2.4. Yield of Designed Flipids

Flipids	Eth-C16	Pyr-C16	Aze-C16	Ami-C16	Mor-C16	Tri-C16
Yield (%)	62.7	56.2	78.8	71.2	79.4	66.1

Chapter 3: Preparation and Characterization of pH-sensitive Fliposome

3.1 Introduction on Strategies to Prepare Liposomes

When amphiphilic molecules are placed in aqueous environment, they tend to form aggregated complexes in order to shield their hydrophobic moieties from water molecules while maintaining contact with the aqueous phase with their hydrophilic moieties. The formation of liposomes is not a spontaneous process. It requires sufficient amount of energy (sonication, homogenization, heating, etc.) to achieve a thermodynamic equilibrium and to form organized, closed bilayer vesicles[132]. Typically, liposomes can be prepared using mechanical dispersion methods or solvent dispersion methods[133, 134].

The mechanical dispersion methods involve the following procedures: lipid film hydration, sonication, freeze-thawing, and membrane extrusion. When liposomes are prepared with mixed lipids, the lipids must first be dissolved as a homogenous mixture in an organic solvent. The solvent is then to be removed under vacuum to yield a lipid film. Lipid film hydration is accomplished by adding a hydration buffer above the lipid transition temperature (T_m). A bath or probe tip sonicator is usually used for producing small unilamellar vesicles (SUV) with diameters in the range of 15-50 nm. The main disadvantages of sonication are low internal volume, low encapsulation efficacy and possible degradation of the lipids and encapsulated contents[134]. The process of freezing and thawing results in unilamellar vesicles by inducing the fusion of SUV[135, 136]. Extrusion is a process in which micrometric liposomes are extruded using polycarbonate filters with different pore size to yield liposomes of a smaller size. This process should be carried out above the transition temperature of the lipids.

Three commonly used methods of solvent dispersion for liposome preparation are ether injection, ethanol injection and reverse phase evaporation[133]. The ether injection method involves gradually injecting an ether solution of lipids into aqueous buffer at 55°C to 65°C or under reduced pressure. The elevated temperature or the reduced pressure removes ether to form the liposomes. The ethanol injection method involves rapidly injecting an ethanol solution of lipids into a much larger volume of aqueous buffer. Liposomes are formed upon the dilution of the ethanol, which can then be removed by dialysis. The disadvantage of both the ether injection method and the ethanol injection method is that the resultant population of liposomes is heterogeneous. The reverse phase evaporation method is based on the conversion of inverted micelles of lipid-coated organic solvent molecules in aqueous buffer into a viscous gel by evaporating the organic solvent. When the gel eventually collapses, some of the phospholipids form bilayer structures around the residual micelle to form liposomes[133]. Liposomes made from this method usually have a higher aqueous space-to-lipid ratio[137] than other methods of liposome preparation.

In this study, mechanical dispersion methods were used for liposome preparation due to the well-established procedures in our group. The preparation involved lipid film hydration, freeze-thawing, and membrane extrusion. The sonication was avoided in order to form liposomes with relatively high internal volume and encapsulation efficacy.

3.2 Materials and Methods

3.2.1 Materials. The lipids 1,2-dipalmitoyl-sn-glycero-3-phosphocholine (DPPC), N-palmitoyl-sphingosine-1-(succinyl[methoxy(polyethylene glycol)2000]) (PEG-ceramide), 1,2-dipalmitoyl-sn-glycero-3-phosphoethanolamine-N-[azido(polyethylene glycol)-2000 (DPPE-PEG (2000)) were purchased from Avanti Polar Lipids, Inc. (Alabaster, AL, USA). Cholesterol

was purchased from Fisher. Doxorubicin Hydrochloride was purchased from Biotang (Waltham, MA, USA). Calcein was purchased from Thermo Fisher Scientific. 2-[4-(2-hydroxyethyl)piperazin-1-yl]-ethanesulfonic acid (HEPES), octaethylene glycol monododecyl ether (detergent C₁₂E₈) and all other chemicals were purchased from Sigma, Fisher or VWR.

3.2.2 Preparation of liposome.

3.2.2.1 Preparation of DOX-loaded liposome. Lipids were dissolved in dichloromethane or chloroform as stock solutions. Liposomes were prepared using the thin-film hydration technique based on prior reports[122, 123]. Ratios of lipid components were in mole units. Lipids of different compositions (Table 3.1) were mixed in a pear-shaped recovery flask. The solvent was removed by a rotary evaporator to form a thin film at the bottom of the flask. The lipid film was further dried in a vacuum for at least four hours before hydration with 30 mM HEPES buffer (pH 7.4) containing 300 mM MnSO₄ in a 60 °C water bath. The flask was filled with argon and sealed with parafilm. The total lipid concentration was 20 mM. After all the lipid film was detached from the flask, the milky liposome suspension was then sequentially immersed in liquid nitrogen. The flask was then immersed in ice-and-water mixture for two minutes before being immersed back in 60 °C water bath until the temperature was equilibrated. The freeze-thawing process was repeated seven times. Then the liposome suspension was extruded twenty-one times each through polycarbonate membrane with pores of 400, 200 and 100 nm in diameter (Nucleopore, Pleasanton, CA, USA) sequentially, using a hand-held extrusion device (Avanti Polar Lipids, Alabaster, AL, USA). The resultant liposome suspension was run through a Sephadex G-75 size exclusion column pre-equilibrated with 5 mM HEPES and 145 mM NaCl at pH 7.4 to remove the unencapsulated manganese sulfate and thus to establish the transmembrane manganese sulfate gradient. Doxorubicin was dissolved in the same

5 mM HEPES and 145 mM NaCl buffer at pH 7.4 to a concentration of 4 mM. The solution was then mixed with the liposomes carrying the transmembrane manganese sulfate gradient in 1:1 volume ratio and incubated at 60 °C for 50 minutes [138]. The unencapsulated doxorubicin was then removed by gentle shaking with Dowex[®] Resins (prewashed with 2 M NaOH and equilibrated with 1 M NaCl[139], resin: Doxorubicin = 60 :1, wt : wt) for 25 minutes. The resultant liposome preparations were stored at 4 °C in brown glass vials that were filled with argon until further studies.

Table 3.1. Lipid Compositions of pH-Sensitive Flipsomes A-F and non pH-Sensitive Control Liposome G

Liposome molar %	A	B	C	D	E	F	G
Tri-C16	25	x	x	x	x	x	x
Mor-C16	x	25	x	x	x	x	x
Ami-C16	x	x	25	x	x	x	x
Aze-C16	x	x	x	25	x	x	x
Pyr-C16	x	x	x	x	25	x	x
Eth-C16	x	x	x	x	x	25	x
DPPC	70	70	70	70	70	70	55
PEG-Ceramide	5	5	5	5	5	5	5
Cholesterol	x	x	x	x	x	x	40

3.2.2.2 Preparation of liposomes encapsulating calcein. DPPC, Mor-C16 TACH lipid, PEG-Ceramide (70: 25: 5) and DPPC, Cholesterol, PEG-Ceramide (55: 40: 5) were mixed in a pear-shaped recovery flask. The solvent was removed by a rotary evaporator to form a thin film at the bottom of the flask. The lipid film was further dried in a vacuum for at least four hours before hydration with 100 mM Calcein (pH 7.4) in a 60 °C water bath, when the flask kept filled

with argon and sealed with parafilm. The total lipid concentration was 20 mM. After all the lipid film was detached from the flask, the liposome suspension was immersed sequentially in liquid nitrogen, ice-and-water mixture for two minutes, and back in a 60 °C water bath until the temperature was equilibrated. The freeze-thawing process was repeated seven times. Then the liposome suspension was extruded twenty-one times each through polycarbonate membranes with pores at 400, 200 and 100 nm in diameter (Nucleopore, Pleasanton, CA, USA) sequentially, using a hand-held extrusion device (Avanti Polar Lipids, Alabaster, AL, USA). The resultant liposome suspension was passed through a Sephadex G-75 size exclusion column pre-equilibrated with 5 mM HEPES and 145 mM NaCl at pH 7.4 to remove the unencapsulated calcein. The liposome preparations were stored at 4°C in brown glass vials that were filled with argon.

3.2.3 Physicochemical characterizations of liposomes. The sizes and ζ -potential of the liposome formulations were measured using a Malvern Zeta 3000 Photon Correlation Spectrometry instrument (Malvern Instruments Ltd., Worcestershire, UK).

3.2.4 Encapsulation efficiency of liposomes. An aliquot (10 μ L) of DOX-loaded liposome was mixed with 190 μ L lysing buffer containing 90% isopropanol and 0.075 M HCl[140]. The fluorescence of DOX was read on a fluorometric 96 well plate reader (Ex. = 485 nm and Em. = 590 nm). The concentration of DOX was quantified from a calibration curve of DOX standard solutions (1, 2, 5, 10, 20, 50, 100 μ g/ml). The encapsulation efficiency of DOX-loaded liposome can be determined by the ratio of the amount of encapsulated DOX and the amount of DOX incubated with the liposome for the drug-loading.

3.2.5 pH-Triggered release of liposomes.

3.2.5.1 pH-Triggered release of DOX-loaded liposomes. Four buffers of different pH were prepared as the following: pH 7.4 (100 mM HEPES, 92.6 mM glucose), pH 7.0 (100 mM HEPES, 92.6 mM glucose), pH 6.5 (100 mM MES, 92.6 mM glucose), pH 6.0 (100 mM MES, 92.6 mM glucose). Liposome formulations were gently shaken with sufficient amount of resin (resin : Dox = 60 : 1, wt : wt) in each of the four buffers at 37°C. At given time points (0, 1, 3, 6, 12, 24, 36, 72 h, 10 µl of each formulation were transferred into a clear bottom black 96 well plate containing 190 µl 90% isopropanol with 0.075 M HCl in each well. After 5 minutes of gentle shaking to fully lyse the liposomes the fluorescence of the released doxorubicin was measured in a fluorescence 96 plate reader. The fluorescence reading at time zero was considered as the total encapsulated DOX in each formulation. All measurements were in triplicates. The amount of doxorubicin was estimated from the calibration curve as described before and the release percentage was calculated as:

$$\text{release \%} = \left(1 - \frac{M_{\text{time}}}{M_{\text{total}}}\right) \times 100$$

3.2.5.2 pH-Triggered release of calcein-loaded liposomes. An aliquot (20 µl) of a liposome formulation was added into 180 µl of a buffer of defined pH at 7.4, 7.0, 6.5 or 6.0 as described above in a 96 well plate. The plate was incubated at 37°C. At different time points (1, 3, 6, 12, 24, 36, 72 h), the fluorescence of each well was measured on fluorometric 96 well plate reader (Ex. = 495 nm and Em. = 515 nm). After the fluorescence measurement at the last time point, 10 µl detergent (C₁₂E₈) was added to fully lyse the calcein-loaded liposomes. All measurements are in triplicates. The release percentage was calculated as following, where F_t is the fluorescence reading of certain time point and F_{last} is the fluorescence reading of last time point.

$$\text{release \%} = \frac{F_t}{F_{last}} \times 100$$

3.3 Results and Discussion

3.3.1 Lipid compositions in liposome formulations. We successfully formulated liposomes that consisted of lipids, a PEG-Ceramide conjugate and DPPC. The lipid compositions of such liposome formulations are listed in Table 3.1. PEG-Ceramide, which contains a C16 hydrocarbon tail, facilitates the lipid film hydration and is expected to yield long-circulating stealth liposomes[87]. DPPC is a common commercially available lipid that also contains C16 hydrocarbon tails as in PEG-Ceramide and the lipids to facilitate the mixing of the lipids in the liposome membrane[141]. Previously lipids with C12 hydrocarbon tails were used to readily prepare liposomes consisting of 50 mol% lipids, 45 mol% POPC and 5 mol% PEG-Ceramide[123], wherein POPC, which carries on saturated and one unsaturated C16 hydrocarbon chain, is a highly compatible lipid with many types of other lipids to form lipid bilayer[142]. During the preparation of liposomes consisting of saturated C16 lipids, the resistance against liposome extrusion was exceptionally high when 50 mol% lipids were applied, which generated highly heterogeneous lipid suspensions. The high resistance against extrusion was probably due to the higher transition temperature and thus less fluidity of the lipid bilayers. As a compromise, lower mol% of lipids was attempted in this thesis work, which allowed the construction of liposomes consisting of 25 mol% of a lipid, 70 mol% DPPC and 5 mol% PEG-Ceramide. A non pH-sensitive stealth liposome containing 55 mol% DPPC, 40% Cholesterol and 5 mol% PEG-Ceramide was prepared as a control based on the FDA approved liposomal DOX formulation Doxil which contains 56.56 mol% fully hydrogenated soy phosphatidylcholine (HSPC), 38.18 mol% Cholesterol and 5.26 mol% N-(carbonyl-methoxypolyethylene glycol

2000)-1,2-distearoyl-sn-glycero-3-phosphoethanolamine sodium salt (MPEG-DSPE)[143].

HSPC contains two saturated hydrocarbon chains with different length (C16 and C18). MPEG-DSPE contains two saturated hydrocarbon chains of C18. In order to compare the pH-sensitivity of liposomes with control liposome, HSPC and MPEG-DSPE were replaced with DPPC and PEG-Ceramide to formulate the control liposome to avoid the influence from the length of the tails. Cholesterol is a membrane constituent found in many biological systems and widely used in liposomal formulations[144].

3.3.2 Sizes, ζ -potential and polydispersity index (PDI) of liposome formulations.

After freeze-thawing and extrusion through polycarbonate membranes with 100 nm pores, the liposomes showed average sizes smaller than 200 nm. The Polydispersity Index (PDI) of all formulations were lower than 0.3, indicating homogeneous liposomal suspensions. ζ -potential are not detectable for all measurements suggesting that liposome formulations are neutral. The average sizes and PDI of DOX-loaded liposomes are shown in Table 3.2. The average size of calcein-loaded Mor-C16 liposome was 144.3 nm with a PDI of 0.15.

Table 3.2. Size and Polydispersity Index of DOX-loaded Liposomes

Fliposome	Molar Ratio	Size (nm)	PDI.
Tri-C16/DPPC/PEG-Ceramide	25/70/5	152.2	0.126
Mor-C16/DPPC/ PEG-Ceramide	25/70/5	170.5	0.064
Ami-C16/DPPC/ PEG-Ceramide	25/70/5	134.4	0.169
Aze-C16/DPPC/ PEG-Ceramide	25/70/5	119.8	0.165
Pyr-C16/DPPC/ PEG-Ceramide	25/70/5	120.8	0.174

Eth-C16/DPPC/ PEG-Ceramide	25/70/5	141.1	0.253
Cholesterol/DPPC/PEG-Ceramide	40/55/5	156.4	0.083

It is well known that the size of drug delivery systems impacts their pharmacokinetics and tissue distribution[145]. Only nanocarriers with a size lower than 150 nm are able to exit fenestrated capillaries into the tumor interstitium[146, 147]. However, some literature suggests that delivery systems below 200 nm in size could take advantage of the EPR effect for passive targeting to tumor tissues[148, 149]. It is reported that in blood circulation nanocarriers with a size ranging 100-150 nm do not easily leave the capillaries that perfuse normal tissues in kidney, lung and heart[145, 150]. Because the fliposomes under this study are all below 200 nm in size and mostly in the range of 100-150 nm, they could serve as nanocarriers for anticancer drugs.

3.3.3 Encapsulation efficiency (EE) of DOX-loaded fliposomes. As shown in Table 3.3, the encapsulation efficiencies of DOX-loaded fliposomes were in the range of 76% to 100% with the remote loading method.

Table 3.3. Encapsulation Efficiency of Dox-loaded fliposomes

Fliposome	Molar Ratio	EE (%)
Tri-C16/DPPC/PEG-Ceramide	25/70/5	100
Mor-C16/DPPC/ PEG-Ceramide	25/70/5	100
Ami-C16/DPPC/ PEG-Ceramide	25/70/5	88

Aze-C16/DPPC/ PEG-Ceramide	25/70/5	86
Pyr-C16/DPPC/ PEG-Ceramide	25/70/5	95
Eth-C16/DPPC/ PEG-Ceramide	25/70/5	76

Remote loading, also known as active loading, was used for loading DOX into fliposomes because of its higher encapsulation efficiency compared to the passive loading method. Remote loading relies on a transmembrane gradient to trap the payload molecules inside the liposome after they diffuse across the liposomal bilayer. Several remote loading methods have been reported for DOX encapsulation including pH gradient, ammonium sulphate gradient and manganese gradient[100]. In this project we use manganese gradient for remote loading because it is compatible with the pH-sensitivity of the fliposomes and is believed to have a higher encapsulation efficiency based on previous studies[151].

3.3.4 pH-Dependent leakage of fliposomes. We studied the pH-dependent leakage of fliposomes by measuring their release of DOX and Calcein at pHs 7.4, 7.0, 6.5 and 6.0, 37°C over time. The pH range of 6.0 - 7.4 was chosen because of the reported pH range of 5.7 - 7.8 inside tumor tissues[113, 114]. The fluorescence of DOX or Calcein was measured and converted to percentage of release by normalization against the fluorescence of the same sample after lysing the liposomes with detergent (100% release). pH-triggered release of DOX over 12 h and pH-triggered release of calcein at 12h from fliposomes are showed in Figure 3.1 and 3.2, respectively.

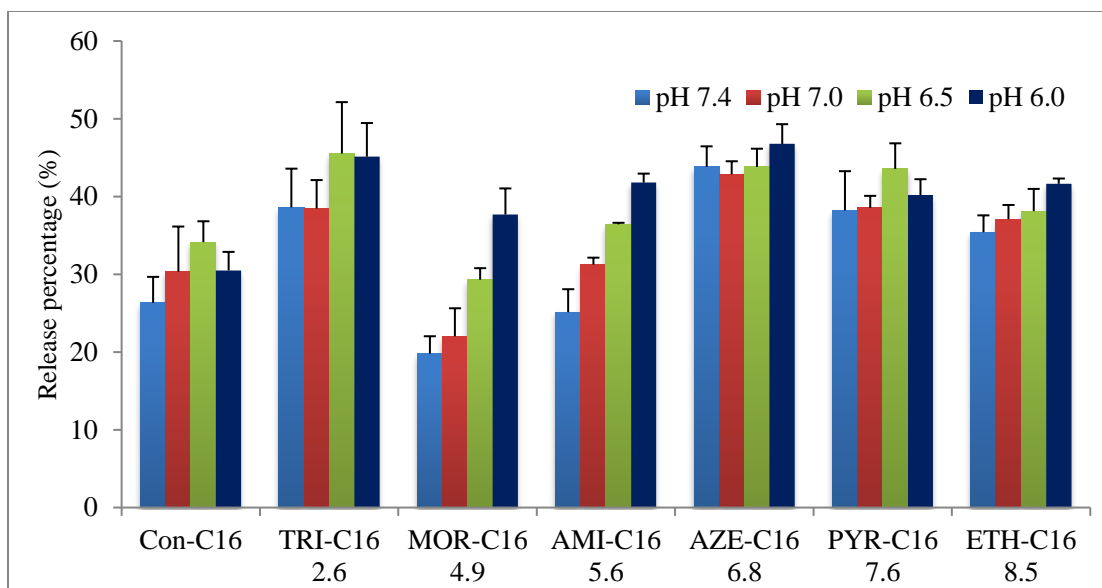


Figure 3.1. Release Percentage of DOX-loaded liposomes over 12h at four different pHs, 37°C. (n=3) The calculated pKa of each flipid is listed beneath the flipid name

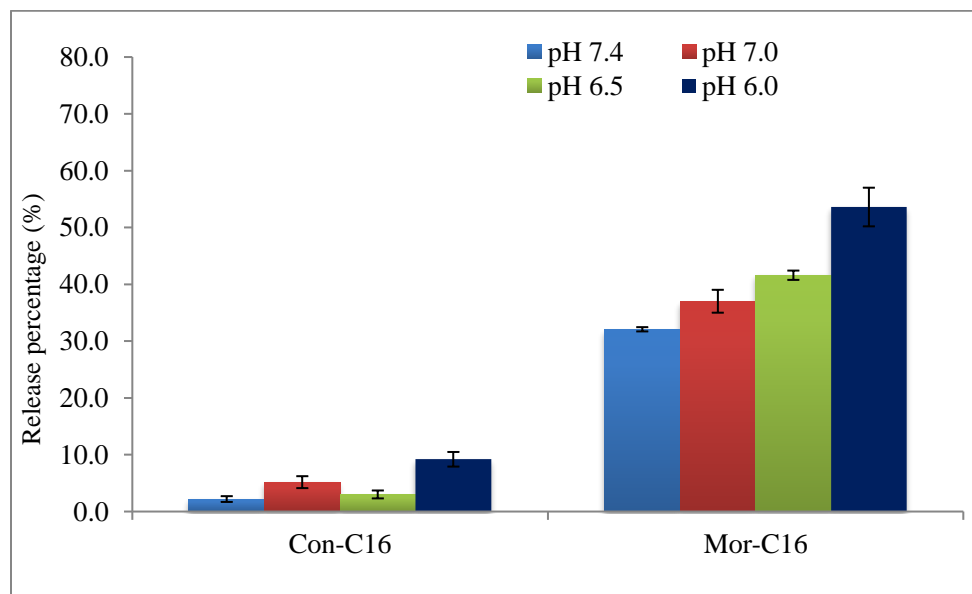


Figure 3.2. pH-Dependent Release of Calcein-loaded Fliposomes over 12h at 37°C. (n=3)

Figure 3.1 shows that several lipids under this study showed enhanced release as the pH decreased compared to the control liposome group. This result is consistent with the proposed mechanism of the pH-sensitivity of the lipids and the liposomes: upon protonation the formation of an intramolecular hydrogen bond between the nitrogen of the amino group and the oxygen of the hydroxy group triggers a conformational flip of the trans-2-amino-cyclohexanol moiety, which increases the separation of the two hydrocarbon chains of the lipid tail, which in turn disrupts the lipid bilayer to trigger the release of the liposome contents [55, 126]. With the same mechanism, a pH-induced expansion (up to 25%) was observed in Langmuir monolayers containing lipids with C12 hydrocarbon tails [152].

Among all the lipids under this study, C16 trans-2-morpholylcyclohexanol-based lipid (Mor-C16) has the lowest release (19.8%) at pH 7.4 and the largest increase of release as the pH dropped from pH 7.4 to 6.0 (17.9%). The estimated pK_a of Mor-C16 lipid is 4.9 based on the change of signal width in an NMR titration in CD_3OD in a previous study [153]. However, the same study estimated a pK_a value of 6.7 for the same lipid in aqueous solution using the ACD/Labs software. This would explain Mor-C16's largest enhancement of release in response to the drop of pH compared to other lipids. The difference of 1.8 ± 0.7 units between the two pK_a values may be attributed to the solvent effect, where the more polar water solvent would favor the protonated, charged form of the lipid more than the less polar CD_3OD , thus the higher pK_a in water [153]. A comparison of calculated pK_a in water versus NMR-estimated pK_a in CD_3OD for all lipids is shown in Table 3.4.

Table 3.4. NMR-estimated pKa in CD₃OD versus Calculated pKa in water of flipids[153]

Flipids	Estimated pKa	Calculated pKa
Eth-C16	8.5	9.7
Pyr-C16	7.6	9.4
Aze-C16	6.8	9.4
Ami-C16	5.6	7.4
Mor-C16	4.9	6.7
Tri-C16	2.6	3.7

The pH-dependent release of Calcein-loaded fliposome consisting of the Mor-C16 lipid was found to carry the same trend as that of the DOX-loaded fliposome, (Figure 3.3) thus strongly corroborating the pH-sensitivity of the fliposomes under this study.

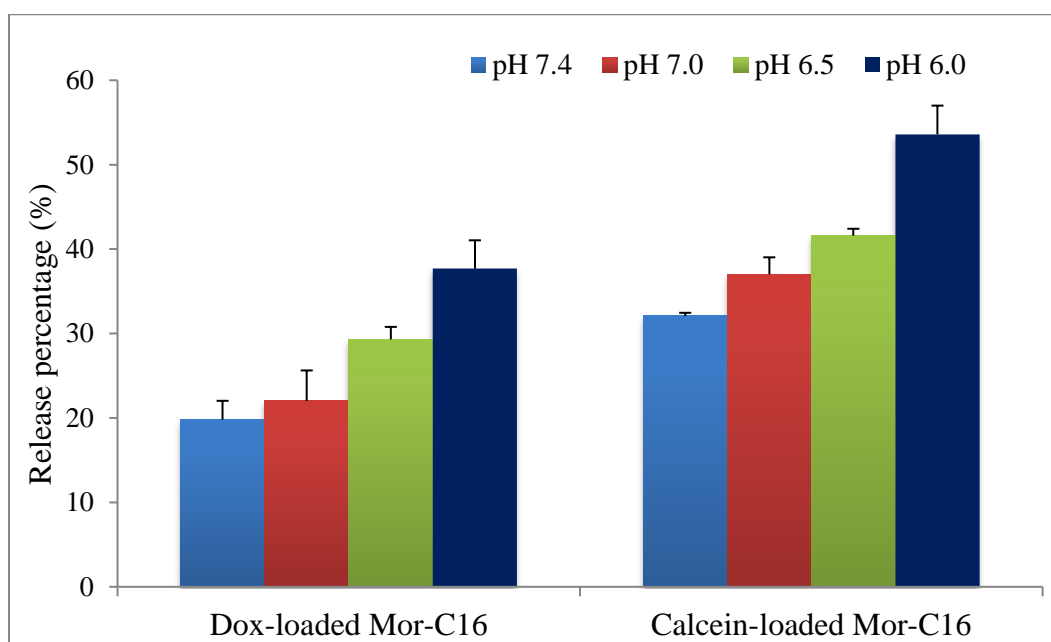


Figure 3.3. pH-Dependent Release of Mor-C16 fliposomes over 12 h at 37°C. (n=3)

Chapter 4: Development of 3D Multi-Cellular Spheroids

4.1 Introduction on 3D multi-cellular spheroids (MCS)

Screening of novel anti-cancer agents are usually performed on cancer cells cultured as two-dimensional(2D) monolayers. Monolayer cells are easy to propagate and amenable to well established high-throughput studies. However, 2D cancer cell models inadequately reflect in vivo tumor growth due to the lack of cell-cell and cell-extracellular matrix (ECM) interactions[154]. The 2D cells do not provide a complex and dynamic microenvironment that is essential for the unique functions of tumors, such as cell proliferation, differentiation, migration and intracellular signal transduction[155-157]. Furthermore, 2D cells may display counterfeit polarity, cell metabolism and protein expression[158].

3D multicellular spheroids (MCS) have been developed to bridge the gap between conventional 2D systems and in vivo tumor models. 3D MCS are self-assembled under conditions where the cancer cells are allowed to grow and interact with their surroundings in three dimensions. 3D MCS have been proven to better mimic the native and complex tumor microenvironment[159].

The advantages of 3D MCS in presenting a more physiological platform for drug delivery include the following:

- 3D MCS have the architecture of tissues in vivo including multicellular arrangement and extracellular matrix, which are absent in 2D models.
- The cell-extracellular matrix interactions can be found in 3D MCS, which is important for the response of cells to drug[160].

- Similar to tissues in vivo, 3D MCS impose diffusional limits to various molecules including drugs, nutrients, oxygen, and protons.
- Rare cells such as cancer stem cells can be cultured in small number of cells in 3D MCS platforms, which is difficult to achieve in conventional 2D cell cultures.
- 3D MCS with a certain size can develop necrotic core, quiescent zone and proliferation zone due to the oxygen and nutrient gradients. It is one cause of drug resistance and can be used for accurate testing of drug efficacy[161-163].

It is reported that 3D MCS smaller than 200 μm in diameter mostly include proliferating cells. When they grow as big as 300 μm in diameter, a normoxic quiescent zone in the middle can be differentiated with the proliferative zone at the surface. Finally, when 3D MCS are larger than 500 μm , the formation of necrotic core can usually be observed[164-166]. A typical configuration of 3D MCS ($> 500 \mu\text{m}$) with different areas is shown in Figure 4.1.

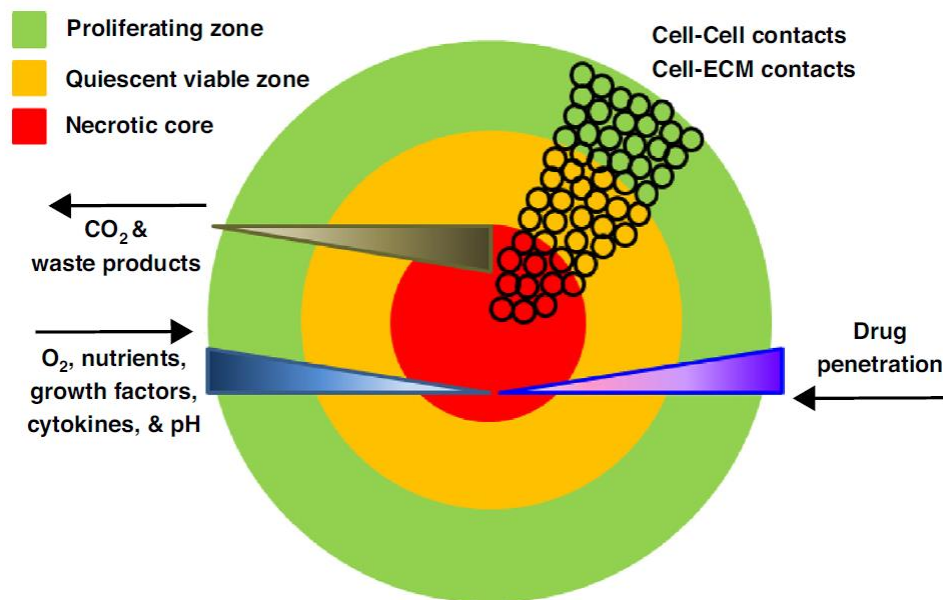


Figure 4.1. 3D MCS over 500 μm in diameter[167]

4.2 Introduction on strategies of generating 3D MCS

Many strategies have been developed to generate 3D MCS in vitro. In general, the techniques of culturing 3D MCS fall into two categories: scaffold techniques and scaffold-free techniques.

Scaffold techniques utilize engineered scaffolds to provide structural support for cells growing in 3D. The most widely used scaffold is hydrogels, which mimic the natural extracellular matrix (ECM) to allow cells to adhere, proliferate, spread and migrate[154, 168]. Hydrogels with interconnected pores enable efficient transport of nutrients and gases. There are several challenges in this technique such as: batch to batch variation, reproducibility and heterogeneity of 3D MCS in size and shape[167].

Scaffold-free techniques have been developed to generate 3D MCS without scaffold support in different kinds of mechanisms. The most commonly used methods include liquid overlay, hanging drop, spinner flask cultures, rotary cell cultures (Figure 4.2) and ultra-low attachment (ULA) plates.

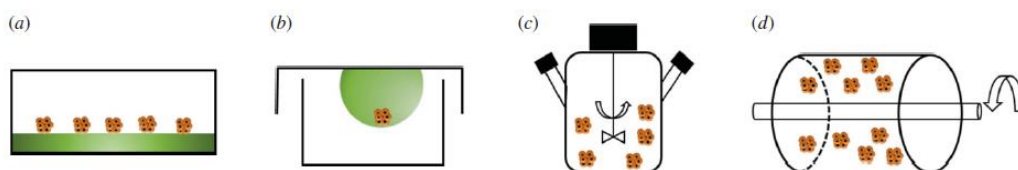


Figure 4.2. Scaffold-free methods for MCS formation. (a) liquid overlay, (b) hanging drop, (c) spinning flask cultures, (d) rotary cell cultures[169]

The liquid overlay method relies on the inhibition of cell adhesion to a pre-coated surface. Hanging drop method allows the cells to aggregate spontaneously in the bottom of a droplet of culture media. Spinning flask and rotary cell cultures keep the cells spinning to form 3D MCS by using continuous stirring. The ULA plates facilitate 3D MCS formation on a hydrophilic, neutrally charged coating that is covalently bound to the polystyrene well surface[167]. The advantages and disadvantages of these methods are summarized in Table 4.1.

Table 4.1. Comparison of scaffold-free techniques used for 3D MCS formation

Method	Advantages	Disadvantages
Liquid overlay	<ul style="list-style-type: none"> • Long culture period • Low cost 	<ul style="list-style-type: none"> • Variation in size and shape

	<ul style="list-style-type: none"> • Easy to handle 	<ul style="list-style-type: none"> • Hard to observe and harvest • Low throughput
Hanging drop	<ul style="list-style-type: none"> • Uniform size and shape control • Low cost • High reproducibility 	<ul style="list-style-type: none"> • Intensive labor • Limited culture period • Low throughput
Spinning flask/Rotary cell	<ul style="list-style-type: none"> • Production of a big number of MCS • Long culture period • Production of large MCS 	<ul style="list-style-type: none"> • Variation in size and shape • Require specialized equipment • Explosion to shear stress
ULA plates	<ul style="list-style-type: none"> • Long culture period • Uniform size and shape • Scalable for high throughput screening 	<ul style="list-style-type: none"> • Various seeding conditions • Costly

4.3 Introduction on the methods of imaging 3D MCS

Microscopy techniques that are commonly used to image monolayer cultured cells are sometimes unsuitable for imaging 3D MCS due to their thick structures that prevent light from penetrating deep without significant distortion[170]. Imaging techniques for thicker biological specimens with high resolution have been more recently developed such as confocal laser scanning microscopy (CLSM) and multiphoton microscopy[170].

Confocal laser scanning microscopy is a high-resolution imaging technique that is based on point illumination with a laser on a sample and spatial filtering of the returning light by a pinhole in an optically conjugated plane in front of the detector. CLSM can be used in both fluorescence mode and reflectance mode. Because only light from the sample that are very closed to the focal plane can be detected, the resolution is much better than wide-field

microscopes. The three-dimensional structures of a sample can be reconstructed with two-dimensional images captured at different depths. The penetration depth in thick samples is limited because the light scattering in such samples causes the illuminating beam to defocus[170]. The amount of light that passes through the pinhole will also decrease as the sample depth gets deeper, effectively limiting the resolution. Penetration depth of the light also depends on the nature of the sample, the NA of the objective and the wavelength of the laser[170]. Generally, excitation laser of longer wavelength can penetrate deeper into samples due to less absorption and scattering. It is reported that the penetration depth of CLSM on 3D MCS is limited to roughly 100 μm [171, 172].

Multiphoton microscopy is based on the principle that two or more photons of lower energy than the energy that is needed for one photon excitation can jointly excite a fluorophore in one quantum event[173]. Such multi photons have to be absorbed simultaneously at the focal point during the excitation, resulting in a high spatial resolution without the need for spatial filtering. In addition, because multi photons used for excitation have longer wavelengths, the penetration depth is improved up to about 1 mm[174].

4.4 Materials and Methods

4.4.1 Materials. HeLa, Hep3b, MDA-MB-231, MDA-MB-468 and A549 cell lines were purchased from ATCC (Manassas, VA, USA). HeLa-eGFP cells were purchased from Cell Biolabs, Inc. (San Diego, CA, USA). Dulbecco's Modification of Eagle's Medium (DMEM), Minimum Essential Medium (MEM) were purchased from Corning (Corning, NY, USA). RPMI 1640 medium, Non-Essential Amino Acid (NEAA) and Trypsin-EDTA were purchased from Thermo-Fisher. Ultra-low Attachment 96 well plates were purchased from Corning. Collagen; 3D viability assay kit and Snarf-1 were purchased from Fisher.

4.4.2 3D MCS formation under different conditions. The formation and growth of 3D MCS depend on many factors such as cell types, seeding densities, external forces and extracellular matrix. In this study, we tried to grow 6 cancer cell lines in three-dimensional configuration using Corning ultra-low attachment (ULA) 96 well plate and tested the effects of three different conditions, namely seeding number, centrifugation, and collagen on the formation of 3D MCS for each cell line.

4.4.2.1 3D MCS formation by different cell types. Some types of cells tend to self-assemble into spheroids in the Corning ultra-low attachment well plates while others tend to form loose clusters of cells under the same condition. In order to investigate the formation of 3D MCS by different cell types, HeLa, HeLa-eGFP, Hep3b, MDA-MB-231, MDA-MB-468 and A549 cells were seeded in the Corning ultra-low attachment 96 well plates at a seeding density of 1000 cells per well. The growth media was changed every other day by replacing 100 μ L of the media in the well with 100 μ L fresh media to maintain a 200 μ L total media volume. The morphology of 3D MCS of each cell line was observed on an inverted microscope.

4.4.2.2 3D MCS formation with different seeding densities. The seeding density of cells at the beginning of growth is a fundamental factor that affects the size of the spheroids. Typically, a spheroid larger than 500 μ m in diameter would develop a necrotic core, which better reflects in vivo tumor growth. In order to investigate the influence of seeding density on the formation and size of 3D MCS, HeLa, HeLa-eGFP, Hep3b, MDA-MB-231, MDA-MB-468 and A549 cells were seeded in the Corning ultra-low attachment 96 well plates at a series of seeding densities of 500, 1000, 2000, 5000 and 10000 cells per well. The cell growth media was changed every other day by replacing 100 μ L media in the well with 100 μ L fresh media to

maintain a 200 μ L total media volume. The morphology of 3D MCS of each cell line was observed on an inverted microscope.

4.4.2.3 3D MCS formation with and without centrifugation. External force, most often centrifuge, is required to facilitate 3D MCS formation for some types of cells. The recommended spin speed from the vendor is 200 g for 5 min at seeding. In order to investigate the influence of external force on the formation of 3D MCS, HeLa, HeLa-eGFP, Hep3b, MDA-MB-231, MDA-MB-468 and A549 cells were seeded in the Corning ultra-low attachment 96 well plates at a seeding density of 1000 cells per well with or without centrifuge. Cell growth media was changed every other day by replacing 100 μ L media in the well with 100 μ L fresh media to maintain a 200 μ L total media volume. The morphology of 3D MCS of each cell line was observed on an inverted microscope.

4.4.2.4 3D MCS formation with and without extracellular matrix (ECM). Extracellular Matrix (ECM) is an important component of the tumor environment in vivo. It provides structural support for cell-cell interactions. Some cell types of 3D MCS cultured in vitro need a long time to develop ECM so adding a small portion of ECM (collagen or fibroblast) at seeding can greatly improve the formation of 3D MCS by increasing the attachment among cells. In order to investigate the influence of ECM on the formation and growth of 3D MCS, HeLa, HeLa-eGFP, Hep3b, MDA-MB-231, MDA-MB-468 and A549 cells were seeded in the Corning ultra-low attachment 96 well plates at a seeding density of 1000 cells per well with or without 1% collagen. The cell growth media was changed every other day by replacing 100 μ L media in the well with 100 μ L fresh media to maintain a 200 μ L total media volume. The morphology of 3D MCS of each cell line was observed on an inverted microscope.

4.4.3 Viability assay for 3D MCS. The LIVE/DEAD Viability/Cytotoxicity kit from ThermoFisher was used to assess the viability of the cells inside 3D MCS. Briefly, HeLa cells or A549 cells were seeded in the Corning ultra-low attachment 96 well plate to form 3D MCS using the method described above. At day 8-10 when the 3D MCS were at $\sim 500 \mu\text{m}$ in diameter, three 3D MCS were transferred to a glass bottom dish containing $200 \mu\text{L}$ of total growth media for each cell line. An equal volume of the LIVE/DEAD kit reagents were added to the 3D MCS which were incubated for 45 mins at room temperature. 3D MCS were then washed 3 times with PBS and imaged using a Leica DMIRE2 confocal microscopy. Fluorescence at $\lambda_{\text{ex}} = 494 \text{ nm}$ and $\lambda_{\text{em}} = 517 \text{ nm}$ was monitored for live cells, while Fluorescence at $\lambda_{\text{ex}} = 528 \text{ nm}$ and $\lambda_{\text{em}} = 618 \text{ nm}$ monitored for dead cells. Images were acquired using the MetaMorph software and analyzed using the ImageJ software.

4.4.4 pH gradient inside 3D MCS. A fluorescent dye SNARF-1 was used to test the pH gradient inside 3D MCS. SNARF-1 is typically used by exciting the dye at one wave length between 488 nm and 530 nm while simultaneously monitoring the emission at two wave lengths, typically about 580 nm and 640 nm . The pH can be determined by the ratio of these two fluorescent signals. HeLa cells or A549 cells were seeded in the Corning ultra-low attachment 96 well plate to form 3D MCS using the methods described above. At day 8-10 when the 3D MCS were at $\sim 500 \mu\text{m}$ in diameter, three 3D MCS were transferred to a glass bottom dish containing $200 \mu\text{L}$ of total growth media for each cell line. SNARF-1 was dissolved in anhydrous DMSO at concentration of 100 M and added to 3D MCS in the glass bottom dish to a final concentration of $10 \mu\text{M}$. The 3D MCS were then incubated for 45 mins at 37°C , washed 3 times with PBS and imaged using a Leica DMIRE2 confocal microscopy.

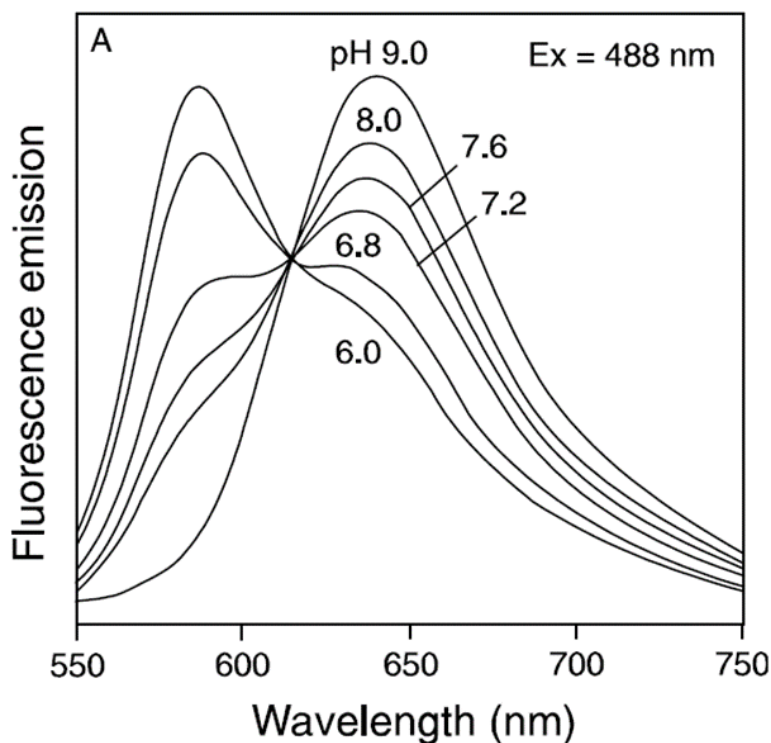


Figure 4.3. The emission of SNARF indicates pH is correlated to the ratio of fluorescence at 580/640 nm[175]

$$\text{pH} = \text{pK}_a - \log\left[\frac{R - R_B}{R_A - R} \times \frac{F_B(\lambda_2)}{F_A(\lambda_2)}\right]$$

The pH at a given point in the fluorescent images can be estimated using the above equation, where pK_a of SNARF-1 is ~ 7.5 , $\lambda_1 = 580 \text{ nm}$, $\lambda_2 = 640 \text{ nm}$, R is the ratio of the fluorescence intensities at the two wave lengths ($F_{\lambda_1}/F_{\lambda_2}$). Subscripts A and B represent the limiting values at the acidic and basic endpoints, respectively. From the equation we can see pH is directly correlated to the R value. The higher R is, the lower pH would be. However, the background signal needs to be subtracted before the calculation of R . Images were acquired using the MetaMorph software and analyzed using the ImageJ software. One z-stack picture at

100 μm above the base of each 3D MCS was selected for the analyses and divided into seven areas using concentric circles. Each of the seven areas was numbered 1 to 7 from the center to the edge. The mean value of the 2 emission fluorescence signals of each region was measured. The R value of each region was then calculated after subtracting the background noise.

4.5 Results and Discussion

4.5.1 3D MCS formation under different growth conditions. Different conditions of culturing 3D MCS in Corning ultra-low attachment 96 well plate is described in the above method sections. The impact of such different conditions on the formation of 3D MCS are showed below.

Under the same culture conditions, different cell lines form 3D MCS of different morphology. For example, after 5 days in culture, Hep3b cells formed tight spheroids of 300 μm in diameter with smooth edges. Hela cells also formed spheroids of 500 μm in diameter with rough edges. However, MDA-MB-468 cells formed very loose spheroids while Hela-eGFP cells grew into only irregularly shaped aggregates (Figure 4.4, scale bar = 100 μm).

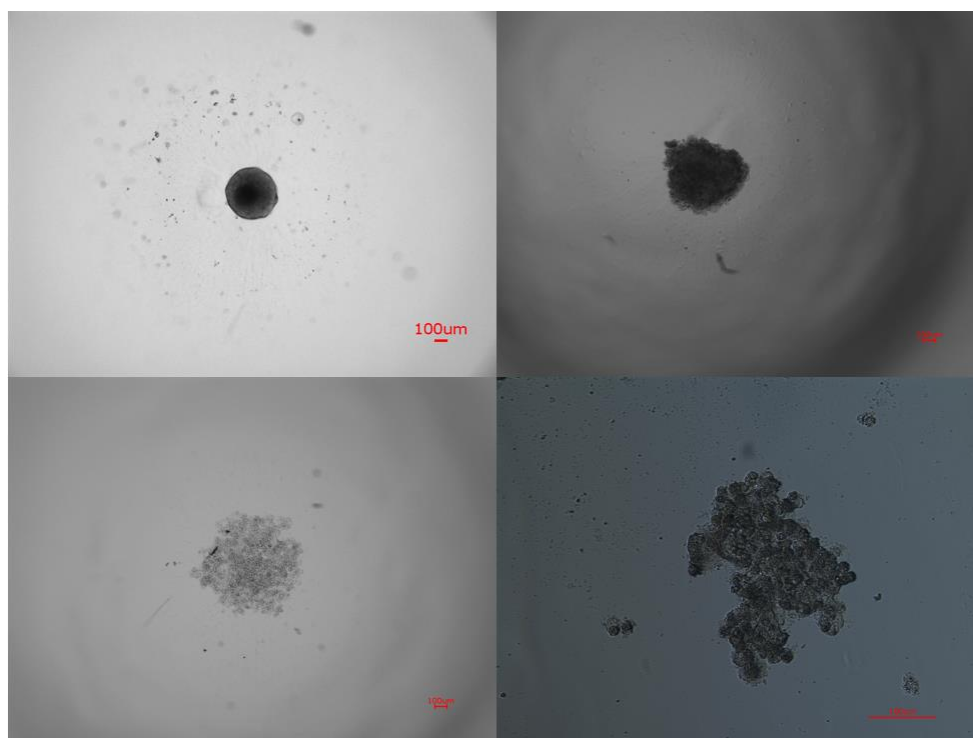


Figure 4.4. Morphology of Hep3b cells (upper left), HeLa cells (upper right), MDA-MB-468 cells (lower left) and HeLa-eGFP cells (lower right) after 5 days in culture in the ULA 96 well plates with same seeding conditions: 1000 cells/well seeding density, without collagen and centrifuge.

The seeding density fundamental impacts the growth and morphology of 3D MCS. For example, the morphology of MDA-MB-468 cells with seeding densities of 500, 1000, 2000, 5000 and 10000 cells per well in Corning ultra-low attachment 96 well plates is presented in Figure 4.5 (scale bar = 500 μm), which shows that a higher seeding density of MDA-MB-468 cells not only yielded larger spheroids after the same days of culturing, but also shortened the time needed for the 3D MCS to eventually turn from the tight round morphology to the more edgy and spread-out morphology.

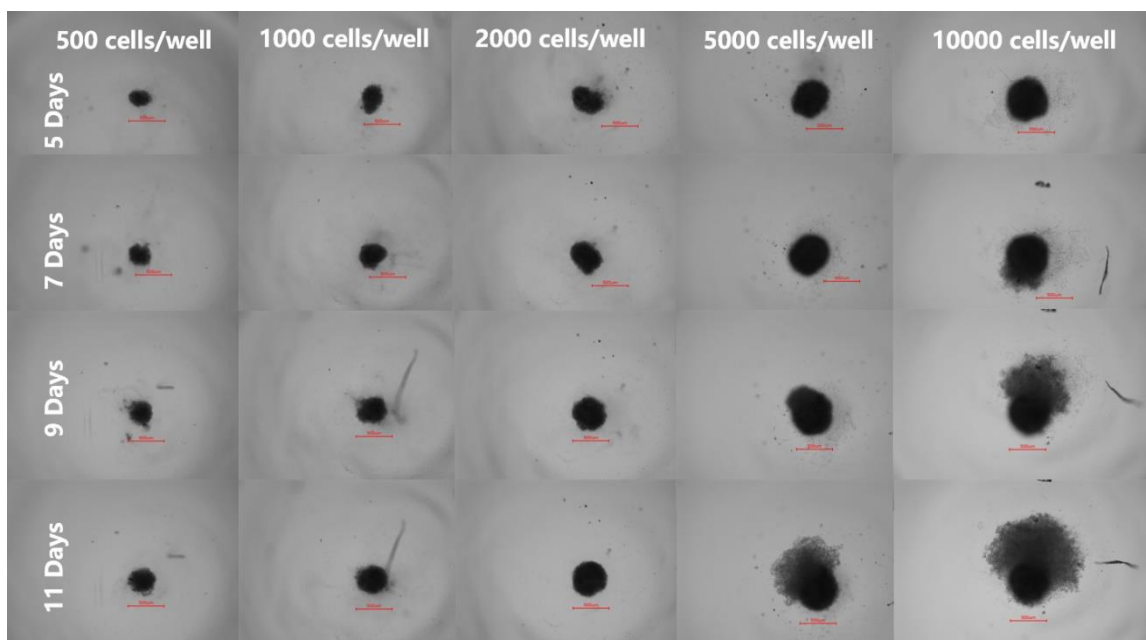


Figure 4.5. 3D MCS of MDA-MB-468 cells after 5, 7, 9 and 11 days of culturing in ULA 96 well plates, starting with different seeding densities

Figure 4.6 compares the growth of Hela-eGFP cells with and without centrifugation. With centrifugation at seeding, Hela-eGFP cells formed spheroids with thin branches of spread cells; without centrifugation at seeding, Hela-eGFP cells yielded no spheroids but only loose aggregates.

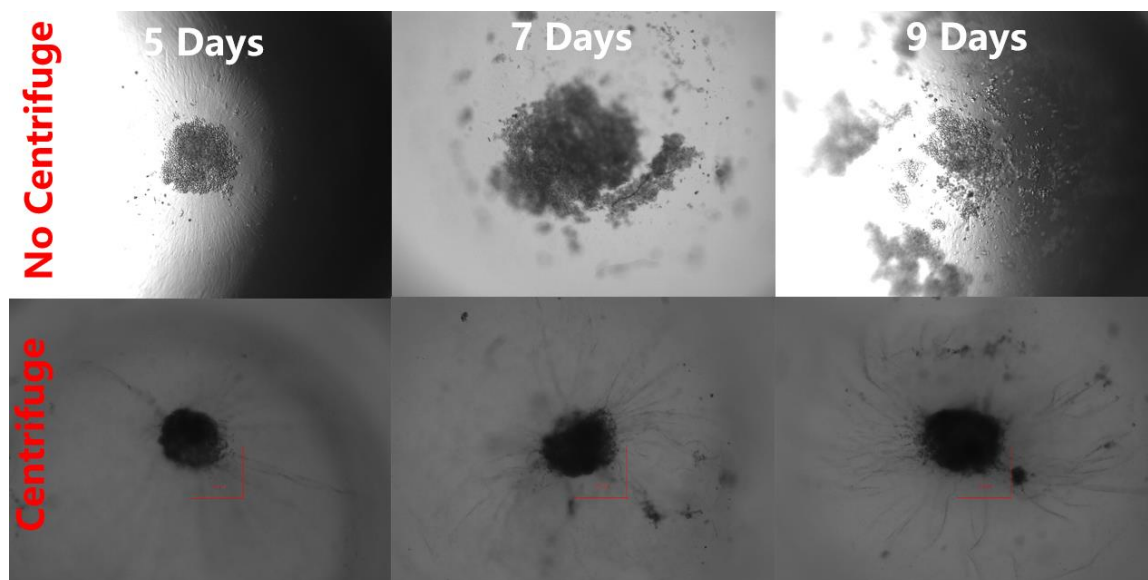


Figure 4.6. Helix-eGFP growth in ULA 96 well plates 5, 7- and 9-days after seeding with and without centrifugation.

A comparison of the morphology of MDA-MB-468 spheroids with and without collagen at seeding is shown in Figure 4.7. Without collagen at seeding, MDA-MB-468 cells formed looser spheroids compared to the group with 1% collagen (scale bar = 500 μm).

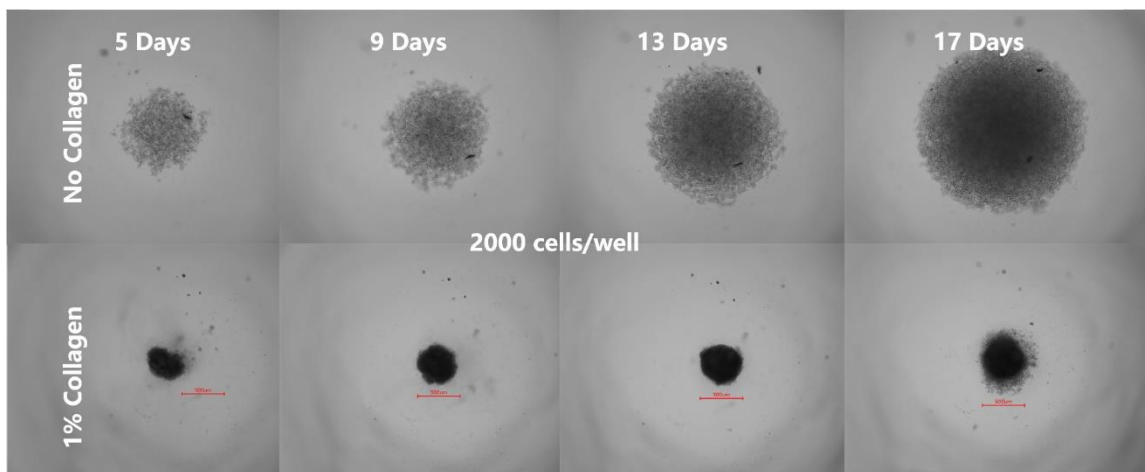


Figure 4.7. MDA-MB-468 3D MCS growth in ULA 96 well plates at day 5, 9, 13 and 17 after seeding with and without collagen.

In order to construct a tight multi-cellular spheroid of different cell lines with a diameter of 500 μm , the selection of seeding density, external centrifugation force and collagen must be taken into consideration. As we mentioned before, spheroids with diameters larger than 500 μm commonly have a necrotic core surrounded by a viable layer of quiescent zone and an outer shell of proliferating cells[176, 177]. The gradients of metabolites, oxygen, nutrients and pH inside the 3D MCS make them a more physiologically relevant platform for testing drug delivery systems than 2D cell models. 3D MCS as large as 500 μm can be obtained either by growing them for a long period of time or by increasing the seeding density.

The growth of 3D MCS are quite dependent on cell types as some cell lines tend to grow tighter rather than bigger whereas other cell lines are likely to form loose or twin spheroids when a high seeding density is applied. For example, Hep3b cells can form tight spheroids without centrifugation or collagen. They tend to grow tighter and tighter after incubating for a long period of time while the size of the spheroids increases very slowly (Figure 4.8).

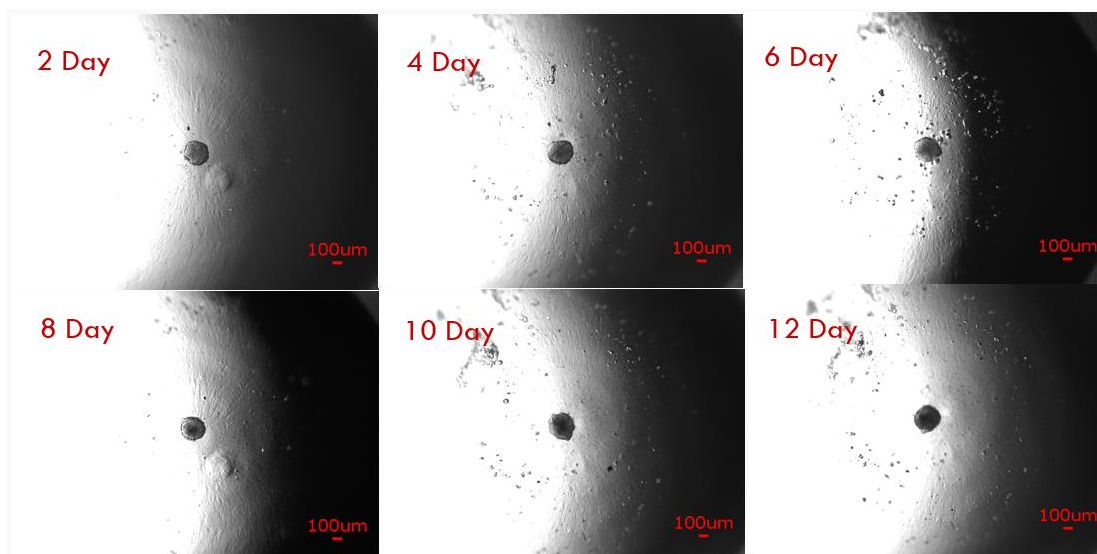


Figure 4.8. 3D MCS of Hep3b cells at seeding density of 2000 cells/well without centrifugation or collagen

In contrast, 3D MCS of MDA-MB-468 cells started to show scattering structures on the outer rim at day 11 after 5000 cells per well were seeded. The same scattering structure was observed at day 9 when 10,000 cells per well were seeded (Figure 4.5).

In this study, a library of 3D MCS of six human cancer cell lines were constructed. Table 4.2 lists the optimized conditions to obtain tight 3D MCS of 500 μm in 7-10 days of culturing for the six cell lines. These 3D MCS could serve as better models than monolayer cancer cell cultures to test drug delivery systems.

Table 4.2. Optimized Conditions to Construct 3D MCS of Six Different Human Cancer Cell Lines

Cell Line	Type of Cancer	Seeding Density on 96 well ULA plate	External Force (Centrifuge)	Extracellular Matrix (Collagen)
Hela	Human Cervical	500	N	N
Hela-eGFP	Human Cervical	500	Y	Y
Hep3b	Human Liver	4000	N	N
MDA-MB-231	Human Breast	3000	Y	Y
MDA-MB-468	Human Breast	2000	Y	Y
A549	Human Lung	3500	Y	N

4.5.2 Imaging the viability of cells in 3D MCS. Figure 4.9 shows the image of a 100 μm deep cross section near the core of 3D MCS of A549 (left) and Hela (right) cells. The green signals from the fluorophore Calcein-AM represent the live cells while the red signals from the fluorophore ethidium homodimer-1 represent the dead cells. The confocal images of both cell lines show that the green signals are concentrated in the peripheral areas, indicating a proliferation zone while the red signals distribute mainly in the core, indicating a necrotic zone.

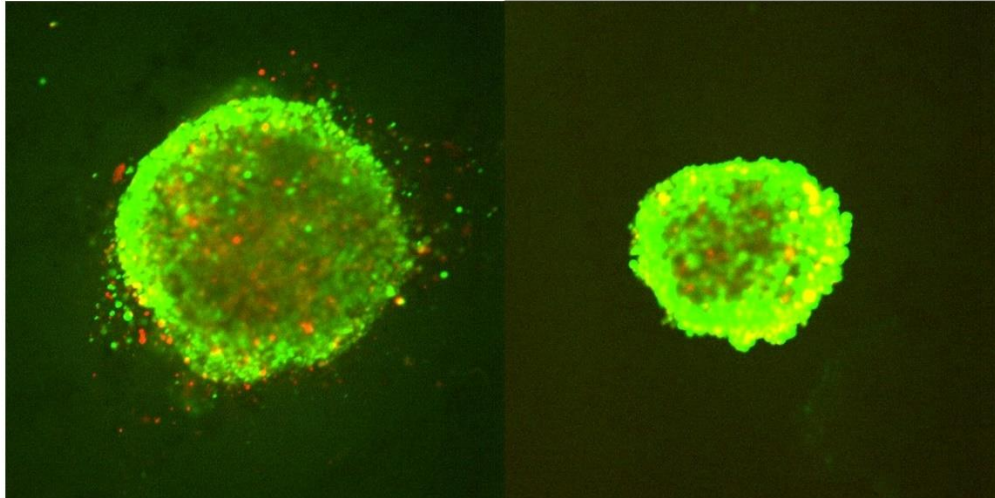


Figure 4.9. Confocal Image of the Viability of Cells in A549 (left) and HeLa (right) 3D MCS.

4.5.3 pH gradient in 3D MCS. pH gradient inside 3D MCS of HeLa cells is indicated by R values.

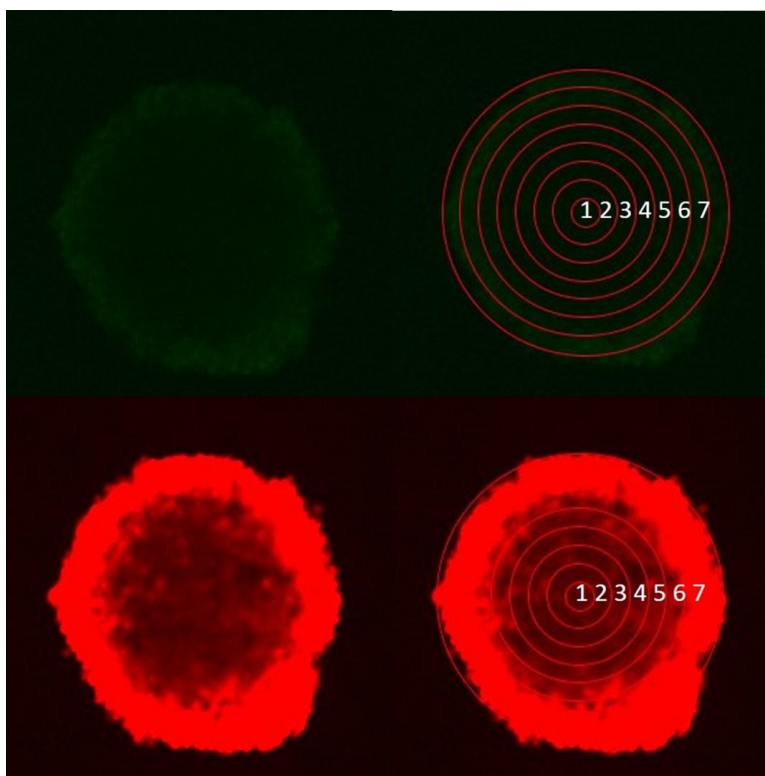


Figure 4.10. Confocal Images of HeLa 3D MCS with SNARF-1 at two channels (580 green, 640 red)

Area	1	2	3	4	5	6	7
R	0.098	0.073	0.071	0.066	0.043	0.037	0.028

pH gradient inside 3D MCS of A549 cells is indicated by R values.

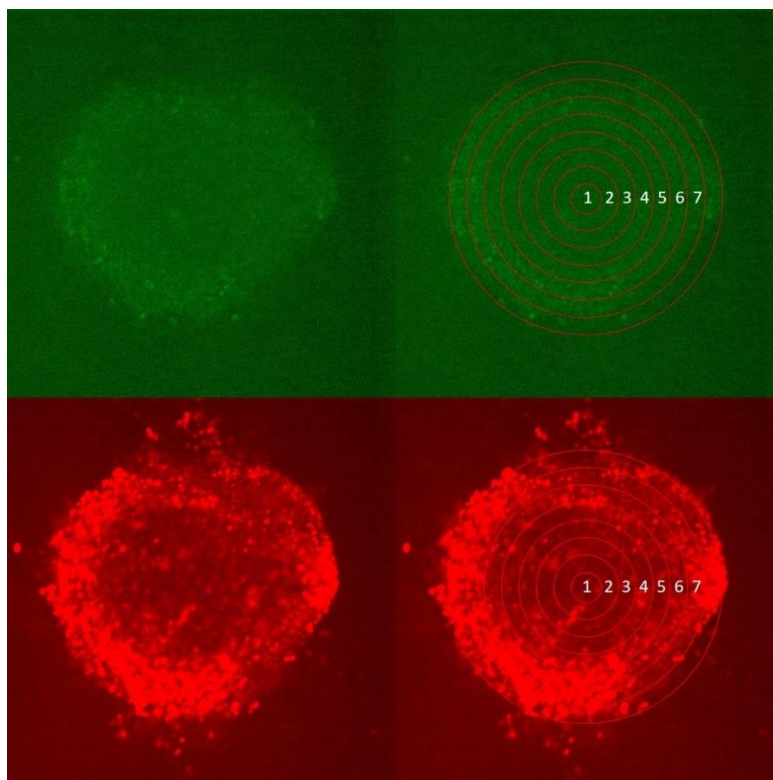


Figure 4.11. Confocal Images of A549 3D MCS with SNARF-1 at two channels (580 green, 640 red)

Area	1	2	3	4	5	6	7
R	0.335	0.274	0.212	0.161	0.108	0.074	0.042

From the equation

$$\text{pH} = \text{p}K_a - \log\left[\frac{R - R_B}{R_A - R} \times \frac{F_{B(\lambda_2)}}{F_{A(\lambda_2)}}\right]$$

where $\text{p}K_a$ of SNARF-1 is ~ 7.5 . $\lambda_1 = 580 \text{ nm}$, $\lambda_2 = 640 \text{ nm}$, R is the ratio of the fluorescent intensities at the two wave lengths ($F_{\lambda_1}/F_{\lambda_2}$). Subscripts A and B represent the limiting values at the acidic and basic endpoints, respectively. For the same sample R_A , R_B , $F_{A(\lambda_2)}$ and $F_{B(\lambda_2)}$ are constant, which means the pH is a function of a single variable R . The

higher R is, the lower the pH. Figure 4.12 shows that, in both cell lines, the R value increases from area 7 to area 1 of the concentric circles, indicating a decrease of pH from the peripheral area to the core area of the 3D MCS of both cell lines.

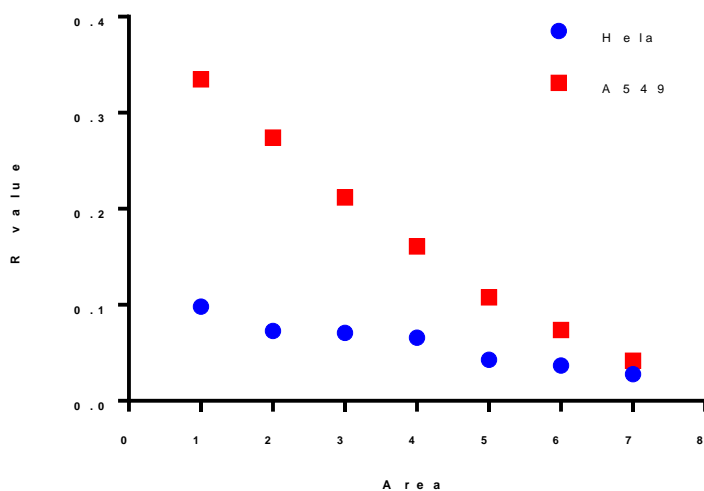


Figure 4.12. R values of different areas in HeLa and A549 3D MCS

The exact pH values were not calculable due to the lack of R_A , R_B , $F_{A(\lambda_2)}$ and $F_{B(\lambda_2)}$ values. It is reported that the value of R_A , R_B from limiting acidic and basic conditions, respectively, can be measured using nigericin calibration[178]. Nigericin is an antibiotic which help equilibrate the pH inside and outside of cells. The idea of using nigericin is to achieve an equilibration of pH inside 3D MCS after 45 min incubation in acidic or basic buffers, so that the R_A , R_B , $F_{A(\lambda_2)}$ and $F_{B(\lambda_2)}$ values can be constant. After trying nigericin calibration with pH 7.4 and 6.0 buffer on both HeLa and A549 cells, large variations on all R_A , R_B , $F_{A(\lambda_2)}$ and $F_{B(\lambda_2)}$ values

were observed. This is probably because of the light penetration and defocusing issues from the confocal microscopy.

Nevertheless, the R values of the areas defined by the concentric circles in each sample demonstrate a clear increasing trend from the peripheral to the core of the spheroids, demonstrating the acidification inside the 3D MCS under our studies.

Chapter 5: Anti-Cancer Activity of pH-Sensitive Fliposomes on 3D MCS

5.1 Introduction: Importance of Anti-cancer Activity Test on 3D MCS

Current studies and screening of anti-cancer drug activities mainly rely on two-dimensional models of cultured cells in vitro and animal models in vivo. In vitro 2D monolayer cell cultures lack the cell-cell and cell-matrix interactions. They also lack, the variations of oxygen level, metabolite concentrations and acidic extracellular pH, which are usually observed in solid tumors. Such deficiencies make the monolayer cells weak models to predict anticancer activities of drugs and drug delivery systems. Many outcomes of studies using 2D are different from those using 3D cell culture models[179-181]. For example, Colley et al. reported that it is critical to deliver drugs deep into the core of the 3D MCS model of head and neck squamous cell carcinoma cells to take effect while only a short contact of the drug with the corresponding 2D monolayer cells is required to show substantial decrease of the cancer cell viability[182]. Sprague et al. reported that dendritic cells cultured in 3D MCS can mimic the microenvironments of ovarian and breast cancer through their interaction with collagen proteins, which is not available in 2D models[183].

The in vivo animal models are not always predictive of human responses to anticancer drugs because of the following several reasons: 1) The widely used murine tumors do not behave like human tumors; 2) The stromal components are not of human origin; 3) The growth rates of xenograft tumors are often faster than primary human tumors[184-186]. The interspecies differences can be profound on extrapolation and interpretation of experimental results[187]. Animal studies sometimes can be complex, unpredictable and can have ethical issues[159]. For example, Zheng et al. found that after developing a novel human gastric tissue-derived

orthotopic and metastatic mouse model of human gastric cancer, it was difficult to achieve the normal function of the implanted human gastric tissue in mouse[188]. There are some other disadvantages of animal models such as cost of time/money and the low-throughput nature of such experiments.

3D MCS have been used for broad studies in anti-cancer drug development as they provide a good in vitro system to mimic the solid tumors more closely than 2D culture systems[189, 190]. Moreover, they can be used to represent the physiological conditions for some rare cells. For example, cancer stem cells are considered to be responsible for the relapse of cancers after treatment[191]. When cultured as spheroids in 3D these cells maintain key properties including gene expression level, tumorigenic activity, differentiation potential and resistance to chemotherapies[192-194]. For example, Fang et al. reported that primary human colon tumor cells in 3D MCS maintained CD133 expression and exhibited resistance to chemotherapy-induced apoptosis, which was not observed in their 2D cultures[193]. Similarly, cells within 3D MCS of ovarian cancer showed increased proliferation and migration potential compared to those that were cultured in 2D[195]. These examples illustrate that 3D MCS can serve as a better platform for cancer research by providing a more physiologically relevant microsystem[179, 196].

5.2 Materials and Methods

5.2.1 Materials. MDA-MB-231, HeLa and A549 cells were purchased from ATCC. CellTiter 96 AQueous OneSolution cell proliferation assay kit and CellTiter-Glo 3D cell viability assay kit were purchased from Promega. Dulbecco's Modification of Eagle's Medium (DMEM) and Minimum Essential Medium (MEM) were purchased from Corning. Ultra-low Attachment

96 well plates were purchased from Corning. Trypsin-EDTA and Collagen were purchased from Thermo-Fisher.

5.2.2 Cytotoxicity assays for DOX-loaded liposomes on 2D monolayer cells and on 3D MCS. CellTiter 96 AQueous OneSolution cell proliferation assay (Promega Corp., WI, USA) was used to test the cytotoxicity of DOX-loaded liposomes on monolayer cancer cells. MB231 cells (~ 10,000 cells/well) were seeded on 96 well plates and grown overnight. At about 80% confluence, the cells were treated with free DOX and liposomal DOX at dosages of 0.05, 0.1, 1, 2, 5, 10, 50, 100, 200 μg DOX per mL in complete medium. The cells were incubated at 37 °C with 5% CO₂ for 72 h before viability measurements. After incubation the cells were washed with 100 μL PBS three times and then supplemented with 100 μL /well of growth media and 20 μL /well of the CellTiter Assay Reagent. The cells were further incubated at 37 °C with 5% CO₂ for 2 h. The absorbance at 490 nm was measured by a 96 well-plate reader. The cells treated with growth media without free or liposomal doxorubicin were assayed in the same way and taken as the control for 100% viability. Each test was performed in triplicate.

CellTiter-Glo 3D cell viability assay (Promega Corp., WI, USA) was used to test the cytotoxicity of DOX-loaded liposomes on 3D MCS. MB231 cells (~ 3000 cells/well), A549 cells (~ 3500 cells/well) and Hela cells (~ 500 cells/well) were seeded on Corning ULA 96 well plate to form 3D MCS using the method described above. After 8-10 days when the spheroids grew to ~500 μm in diameter, they were treated with free Dox and liposomal Dox at dosages of 0.05, 0.1, 0.5, 1, 10, 50, 100, 400 and 800 μg DOX per mL in complete medium. The 3D MCS were incubated for 8 h and 72 h at 37°C with 5% CO₂. The CellTiter-Glo 3D Reagent was thawed at 4°C overnight before the experiment. On the day of experiment the reagent was equilibrated to RT by placing it in a 22°C water bath for approximately 30 minutes and gently

mixed well by inverting the contents. The 3D MCS of each treatment group were transferred to an opaque-walled 96 well plate with 100 μ l medium in each well. An equal volume of 3D reagent was added to each well of the plate. The plated was shaken for 5 minutes and incubated for additional 25 minutes at RT to stabilize the luminescent signal. The luminescence was measured by a 96 well plate luminescence reader. The cells treated with growth media without free or liposomal doxorubicin were assayed in the same way and taken as the control for 100% viability. Each test was performed in triplicate.

5.2.3 Confocal microscopic imaging of 3D MCS after treatment with DOX-loaded liposomes. MB231 cells (~ 3000 cells/well), A549 cells (~ 3500 cells/well) and Hela cells (~ 500 cells/well) were seeded on Corning ULA 96 well plate to form 3D MCS using the method described in Section 4.5.1. After 8-10 days when the spheroids were as large as ~500 μ m in diameter, they were treated with free Dox and liposomal Dox at 10 μ g Dox per mL in complete medium. The spheroids were incubated at 37°C with 5% CO₂ for 4 h and then washed three times with PBS. The spheroids were transferred to a glass bottom dish for imaging on a Leica DMIRE2 laser confocal microscope with the following setup: Exposure (1s), Gain (1x), Image Scaling (1000-3000) and z step (10 μ m). The excitation and emission were at 470 nm and 585 nm, respectively. Images were acquired using the MetaMorph software and analyzed using the ImageJ software.

5.3 Results and Discussion

5.3.1 Cytotoxicity of liposome formulations on 3D MCS of different cell lines.

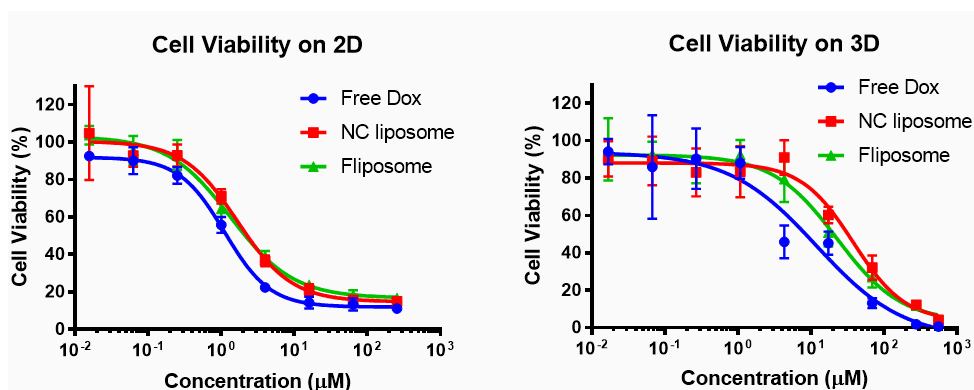


Figure 5.1. Viability of MB231 monolayer cells (left) and MB231 3D MCS (right) after 72 h drug exposure

Table 5.1. IC₅₀ of Different Dox Formulations on monolayer and 3D MCS of MDA-MB-231 cells after 72 h exposure.

IC ₅₀ (µM)	Free DOX	DOX-loaded Non pH-sensitive Control (NC) Liposome	DOX-loaded Fliposome
2D	1.11	1.68	1.35
3D	11.86	37.72	22.54

Fifty percent inhibitory concentration (IC₅₀) values of each Dox formulation was calculated from data shown in Figure 5.1 using the GraphPad Prism software. Against 2D monolayer of MDA-MB-231 cells free DOX showed the lowest IC₅₀ (1.11 µM); DOX-loaded Non pH-sensitive control liposome group gave the highest IC₅₀ (1.68 µM); IC₅₀ of DOX-loaded Fliposome was in the middle (1.35 µM). No statistically significant difference was found between these groups. Against 3D MCS of MDA-MB-231 cells same trend of IC₅₀ values was observed: free DOX gave lowest (11.86 µM), DOX-loaded Non pH-sensitive control liposome

gave highest (37.72 μM), DOX-loaded Fliposome was in the middle (22.54 μM). However, each of the three groups was significantly different ($p < 0.01$) from the other two groups.

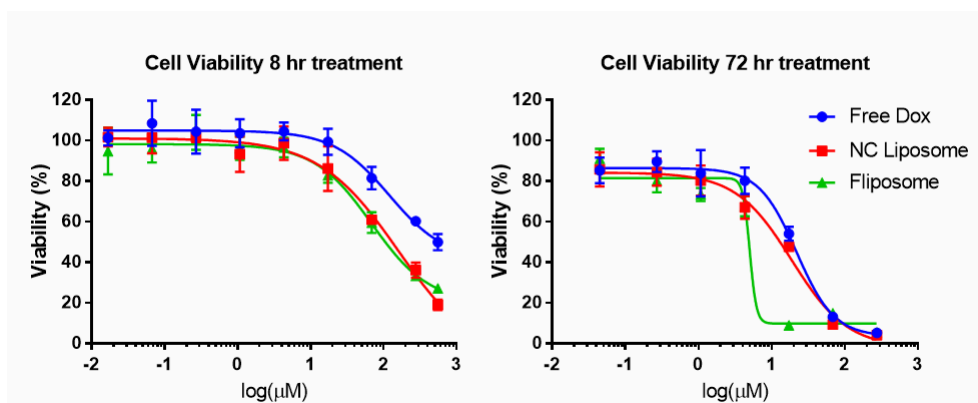


Figure 5.2. Cell Viability of A549 3D MCS at 8 h exposure (left) and 72 h exposure (right)

Table 5.2. IC₅₀ of Different Dox Formulations on A549 3D MCS after 8 h and 72 h exposure

IC ₅₀ (μM)	Free DOX	DOX-loaded Non pH-sensitive Control (NC) Liposome	DOX-loaded Fliposome
8 h	120	159.1	68.6
72 h	21.99	18.88	~5.02

The IC₅₀ values (Table 5.22) calculated from the raw data of Figure 5.2 indicated that after 8 h incubation with 3D MCS of A549 cells DOX-loaded Non pH-sensitive liposomes gave the highest IC₅₀ (159.1 μM) among the three Dox formulations. The DOX-loaded Fliposome group showed the lowest IC₅₀ (68.6 μM) and the IC₅₀ of the Free DOX group was in the middle

(120 μM). After 72 h incubation the free DOX group showed the highest IC_{50} (21.99 μM), followed by the DOX-loaded Non pH-sensitive liposome group (18.88 μM) while the DOX-loaded Fliposome group presented the lowest IC_{50} (~5.02 μM).

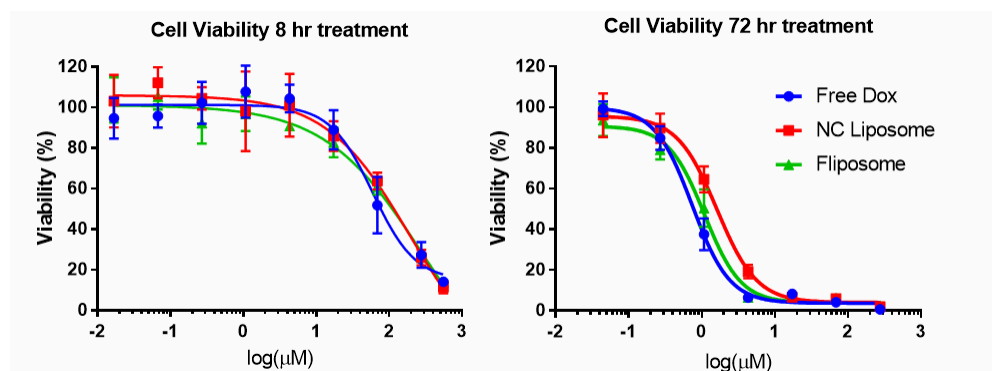


Figure 5.3. Cell Viability of HeLa 3D MCS after exposure to Dox formulations for 8 h (left) and 72 h (right)

Table 5.3. IC_{50} of Different Dox Formulations on HeLa 3D MCS after 8 h and 72 h exposure

IC_{50} (μM)	Free DOX	DOX-loaded Non pH-sensitive Control (NC) Liposome	DOX-loaded Fliposome
8 h	59.57	191.9	282.3
72 h	0.74	1.62	1.09

From the raw data presented in Figure 5.3 we can calculate IC_{50} values of each formulation on HeLa 3D MCS after 8 h and 72 h incubation (Table 5.3). After 8 h exposure the DOX-loaded Fliposome group presented the highest IC_{50} (282.3 μM); the Free DOX group gave

the lowest IC_{50} ($59.57 \mu\text{M}$); IC_{50} of DOX-loaded Non pH-sensitive liposome group was in the middle ($191.9 \mu\text{M}$) of the three. After 72 h incubation the DOX-loaded Non pH-sensitive liposome group showed the highest IC_{50} ($1.62 \mu\text{M}$), followed by the DOX-loaded Fliposome group ($1.09 \mu\text{M}$) while the Free DOX group gave the lowest IC_{50} ($0.74 \mu\text{M}$).

After 72 h drug exposure free DOX imposed more cytotoxicity than both liposomal DOX formulations in both monolayer and 3D MCS cell culture models. This could result from the extended killing effect of free DOX, which is more exposed to the cancer cells while part of the DOX of the liposomal formulations were still concealed inside the liposomes. Nonetheless, the DOX-loaded Fliposome gave a significantly smaller IC_{50} value than the DOX-loaded non pH-sensitive control liposome ($p < 0.01$) against 3D MCS. This is consistent with the proposed pH-triggered release of DOX from the DOX-loaded Fliposome in response to the low pH environment inside the 3D MCS, where more DOX would be released from the fliposomes than the non pH-sensitive control liposomes. The IC_{50} values of all 3D MCS groups were much higher than those of 2D monolayer cells under the same drug treatment, indicating a generally greater drug resistance of 3D MCS.

The cytotoxicities of different treatment groups on HeLa and A549 3D MCS over 8 h and 72 h showed some different patterns (Figure 5.2 and Figure 5.3). After 8 h drug exposure, Free DOX showed higher cytotoxicity than liposomal-DOX groups against HeLa 3D MCS, but lower cytotoxicity against A549 3D MCS. After 72h incubation an apparent increase in cytotoxicity can be observed on both cell lines from DOX-loaded Fliposome groups comparing with Non pH-sensitive liposome control group, which is parallel with the results from MDA-MBA-231 cells. These results suggest that, after long time exposure, the enhanced cytotoxicity in 3D MCS but

not in monolayer cancer cells could be attributed to the enhanced release of DOX from the liposomes in the acidic environment inside 3D MCS.

5.3.2 Distribution of DOX-loaded liposomes in 3D MCS.

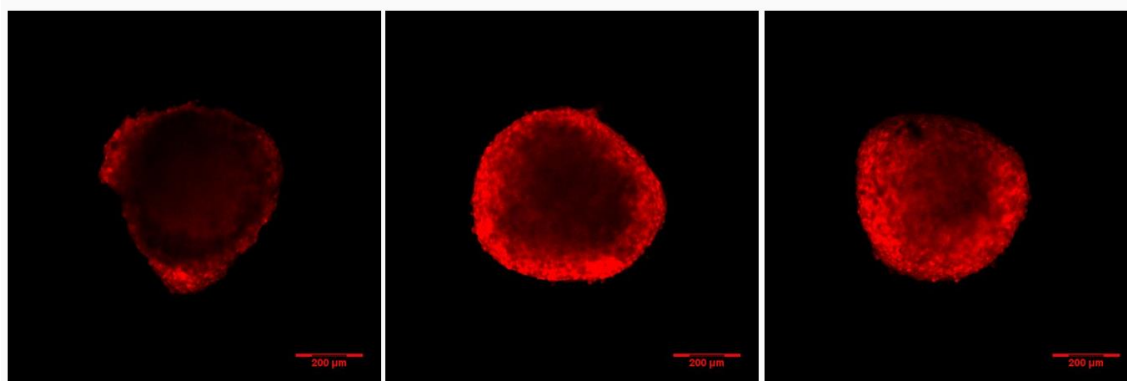


Figure 5.4. Confocal Images of MDA-MB-231 3D MCS (100 μm deep) Treated with Free Dox (left), Dox-loaded Non pH-sensitive liposome (middle) and Dox-loaded Fliposome (right) for 4 h

After 4 h incubation with Free DOX, Dox-loaded Non pH-sensitive control liposome or DOX-loaded fliposomes groups, confocal microscopy images at about 100 μm deep in MDA-MB-231 3D MCS show much stronger fluorescent signals of 3D MCS treated with liposomal DOX than those with Free DOX. An intense ring of DOX accumulated in the outer proliferative cells of each 3D MCS was observed, indicating limited penetration of all formulations after 4 h incubation.

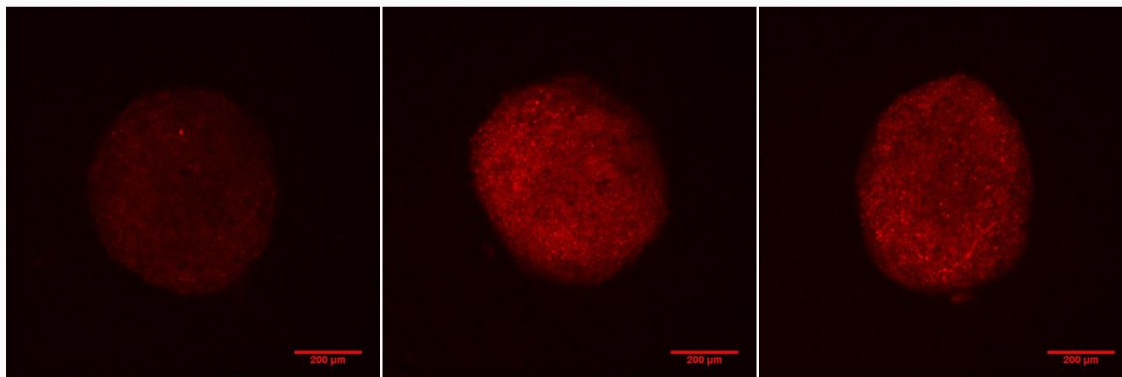


Figure 5.5. Confocal Image of A549 3D MCS (100 μm deep) Treated with Free Dox (left), Dox-loaded Non pH-sensitive liposome (middle) and Dox-loaded Fliposome (right) for 4 h

Figure 5.5 shows that DOX-loaded liposomal groups (middle and left) gave much greater fluorescence than the free DOX group in A549 3D MCS, indicating more accumulation of DOX inside 3D MCS at 100 μm depth after 4 h incubation. The fluorescent signal of A549 3D MCS was more evenly distributed in the 100 μm detection section compared to 3D MCS of MDA-MB-231 cells.

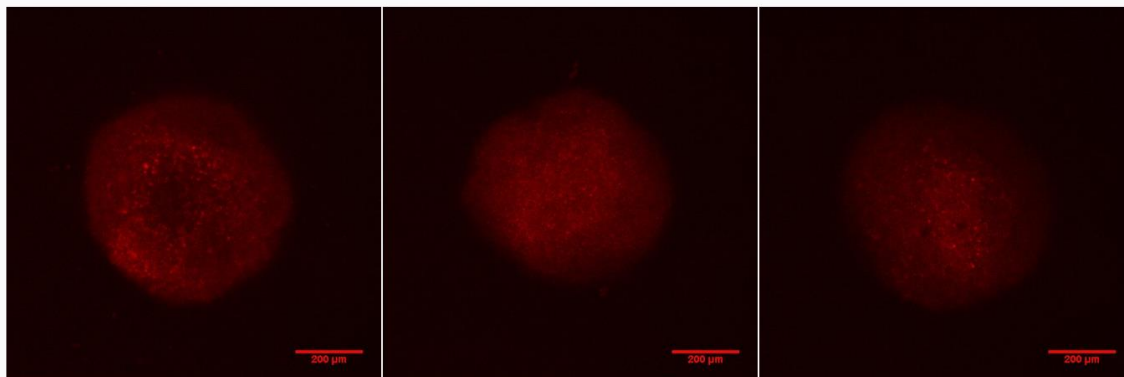


Figure 5.6. Confocal Image of HeLa 3D MCS (100 μm deep) Treated with Free Dox (left), Dox-loaded Non pH-sensitive liposome (middle) and Dox-loaded Fliposome (right) for 4 h.

No significant difference of fluorescent intensity was observed within groups of HeLa 3D MCS after treatment by free or liposomal DOX for 4 h. This result suggests that both free DOX and DOX-loaded liposomes could penetrate into HeLa 3D MCS with similar efficiency given 4 h of exposure time.

This study compares the penetration of free DOX, DOX-loaded Non pH-sensitive liposome and DOX-loaded Fliposome into 3D MCS of 3 cancer cell lines in 4 h of exposure time. Liposomal DOX groups showed more penetration than free DOX in 3D MCS of MDA-MB-231 and A549 cell lines, while no significant difference of penetration in HeLa 3D MCS was observed between liposomal DOX and free DOX. This result indicates a cell line dependence of DOX penetration into 3D MCS, which is consistent with the report by Namhuk, et al. [197]. Several studies have reported that cellular accumulation of the weakly-basic drug Doxorubicin (DOX) has been shown to decrease at low extracellular pH[198-200]. At low pH, the ionized DOX has low lipid solubility and high electrical resistance, leading to a greatly reduced membrane penetration. The insufficient penetration of free DOX into A549 spheroids can be a

reason for the higher cell viability of the free DOX treatment group compared to liposomal DOX groups after 8 h drug exposure (Figure 5.2). There was no significant difference of penetration between DOX-loaded Non pH-sensitive liposome and DOX-loaded Fliposome in 3D MCS of all 3 cell lines after 4 h incubation, suggesting that the enhanced cytotoxicity of the DOX-loaded fliposomes observed in 3D MCS of all 3 cell lines (Figure 5.1, 5.2 and 5.3) resulted from the triggered release of DOX from fliposome in response to the reduced pH inside the 3D MCS.

The confocal scanning of 3D MCS was performed with z-stack sectioning of 10 μm per step from the bottom to top. The 100 μm depth was chosen due to the limit of the confocal laser scanning technique[170]. Light penetration depth above 100 μm is greatly affected by the scattering in the sample and the defocusing of the illumination beam[171, 172]. The 100 μm depth was counted from the starting point where the fluorescent signal start to increase from the background (Figure 5.7). To improve the light penetration depth and thus to obtain images of higher resolution from thick 3D MCS, multiphoton microscopy can be used in the future studies[201]. Cryosection is another alternative way to address the light penetration issue by cutting the spheroids into sections of 10 – 20 μm in thickness. High resolution images of each section can then be easily obtained using confocal microscope. The disadvantage of this method is that the samples need to be fixed and sacrificed during the measurement[202].

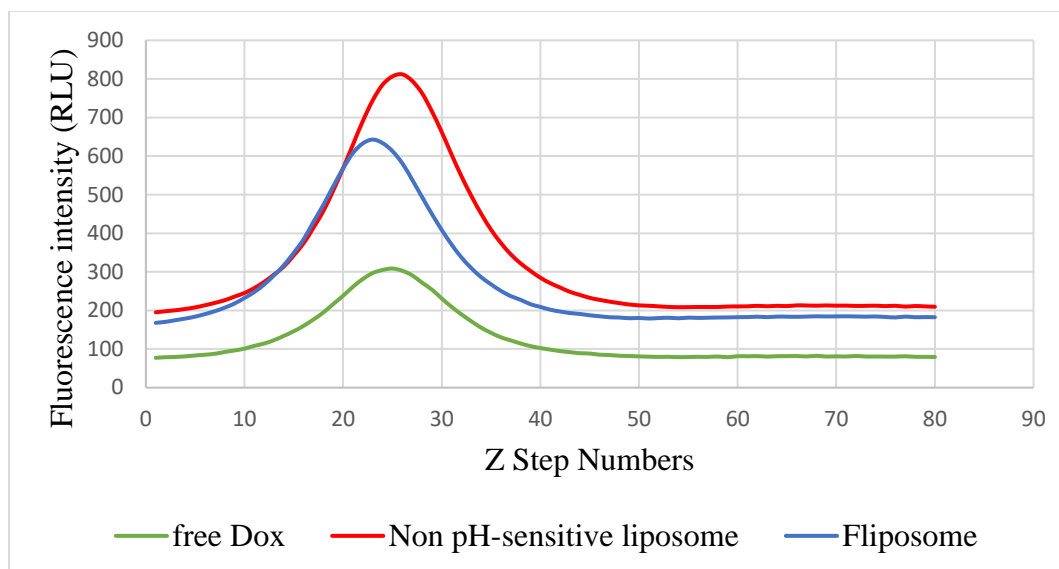


Figure 5.7. DOX Fluorescence in Different Depth of A549 3D MCS after 4 h Incubation

The exact mechanism of the penetration of DOX-loaded non pH-sensitive liposomes and pH-sensitive fliposome into 3D MCS is unclear. But the size and charge of the liposome formulations play an important role in the drug accumulation inside 3D MCS. Kostas et al, investigated the impact of the size and surface charge of liposomes on the penetration into LNCap-LN3 prostate cancer 3D MCS[203]. It was discovered that small liposomes (diameter < 150 nm) can penetrate up to approximately 80 μm deep after 2 h exposure time while larger liposomes (diameter > 800 nm) had minimal interaction with the MCS cells and very limited penetration. Also, cationic liposomes showed minimal intratumoral penetration into the 3D MCS due to the strong electrostatic binding of liposomes to the cancer cells at the peripheral region of the 3D MCS[203]. The neutral charged fliposomes with small size (100 – 200 nm) have been proved to be a promising pH-triggered drug delivery system.

References

1. Institute, N.C. *Understanding Cancer*. 2018; Available from: <https://www.cancer.gov/about-cancer/understanding/what-is-cancer>.
2. William E. Luttrell, W.W.J., Kenneth R. Still., *Toxicology Principles for the Industrial Hygienist*. 2008.
3. Siegel, R.L., K.D. Miller, and A. Jemal, *Cancer statistics, 2018*. CA Cancer J Clin, 2018. **68**(1): p. 7-30.
4. Organization, W.H. *Cancer Fact Sheets*. 2018; Available from: <http://www.who.int/en/news-room/fact-sheets/detail/cancer>.
5. Anand, P., et al., *Cancer is a preventable disease that requires major lifestyle changes*. Pharm Res, 2008. **25**(9): p. 2097-116.
6. Wiki. *Cancer*. 2018; Available from: <https://en.wikipedia.org/wiki/Cancer>.
7. Wilkins, L.W.a., *Stedman's medical dictionary (28th ed.)*. 2006.
8. Institute, D.-F.C. *what is the difference between cancer and a tumor*. 2018; Available from: <https://blog.dana-farber.org/insight/2018/05/difference-cancer-tumor/>.
9. Nordqvist, C. *what are the different types of tumors*. 2017; Available from: <https://www.medicalnewstoday.com/articles/249141.php>.
10. Papetti, M. and I.M. Herman, *Mechanisms of normal and tumor-derived angiogenesis*. Am J Physiol Cell Physiol, 2002. **282**(5): p. C947-70.
11. Fukumura, D., et al., *Tumor microvasculature and microenvironment: novel insights through intravital imaging in pre-clinical models*. Microcirculation, 2010. **17**(3): p. 206-25.
12. Ziyad, S. and M.L. Iruela-Arispe, *Molecular mechanisms of tumor angiogenesis*. Genes Cancer, 2011. **2**(12): p. 1085-96.
13. Konerding, M.A., A.J. Miodonski, and A. Lametschwandtner, *Microvascular corrosion casting in the study of tumor vascularity: a review*. Scanning Microsc, 1995. **9**(4): p. 1233-43; discussion 1243-4.
14. Jain, R.K., *Molecular regulation of vessel maturation*. Nat Med, 2003. **9**(6): p. 685-93.
15. Kobayashi, H., R. Watanabe, and P.L. Choyke, *Improving conventional enhanced permeability and retention (EPR) effects; what is the appropriate target?* Theranostics, 2013. **4**(1): p. 81-9.
16. Yuan, F., et al., *Vascular permeability in a human tumor xenograft: molecular size dependence and cutoff size*. Cancer Res, 1995. **55**(17): p. 3752-6.
17. Morikawa, S., et al., *Abnormalities in pericytes on blood vessels and endothelial sprouts in tumors*. Am J Pathol, 2002. **160**(3): p. 985-1000.
18. Maeda, H., *Tumor-selective delivery of macromolecular drugs via the EPR effect: background and future prospects*. Bioconjug Chem, 2010. **21**(5): p. 797-802.
19. Tredan, O., et al., *Drug resistance and the solid tumor microenvironment*. J Natl Cancer Inst, 2007. **99**(19): p. 1441-54.
20. Jain, R.K., *Determinants of tumor blood flow: a review*. Cancer Res, 1988. **48**(10): p. 2641-58.
21. Institute, N.C. *Types of Cancer Treatment*. 2018; Available from: <https://www.cancer.gov/about-cancer/treatment/types>.

22. Krumbhaar, E.B., *Rôle of the blood and the bone marrow in certain forms of gas poisoning: I. peripheral blood changes and their significance*. Journal of the American Medical Association, 1919. **72**(1): p. 39-41.
23. Joensuu, H., *Systemic chemotherapy for cancer: from weapon to treatment*. The Lancet Oncology, 2008. **9**(3): p. 304.
24. Espinosa, E., et al., *Classification of anticancer drugs—a new system based on therapeutic targets*. Cancer Treatment Reviews, 2003. **29**(6): p. 515-523.
25. Parasuraman, S. *Anticancer drugs I introduction and classification*. 2014; Available from: <https://www.slideshare.net/ParasuramanParasuraman/7-anticancer-drugs-1-introduction-and-classification>.
26. America, C.T.C.o., *Doxorubicin*. 2018.
27. Young, R.C., R.F. Ozols, and C.E. Myers, *The anthracycline antineoplastic drugs*. N Engl J Med, 1981. **305**(3): p. 139-53.
28. Burke, T.G. and T.R. Tritton, *Structural basis of anthracycline selectivity for unilamellar phosphatidylcholine vesicles: an equilibrium binding study*. Biochemistry, 1985. **24**(7): p. 1768-1776.
29. Bellarosa, D., et al., *Apoptotic events in a human ovarian cancer cell line exposed to anthracyclines*. J Pharmacol Exp Ther, 2001. **296**(2): p. 276-83.
30. Pharmacists, T.A.s.o.H.-S. *Doxorubicin Hydrochloride*. 2018; Available from: <https://www.drugs.com/monograph/doxorubicin-hydrochloride.html#moreResources>.
31. Tacar, O., P. Sriamornsak, and C.R. Dass, *Doxorubicin: an update on anticancer molecular action, toxicity and novel drug delivery systems*. J Pharm Pharmacol, 2013. **65**(2): p. 157-70.
32. Momparler, R.L., et al., *Effect of adriamycin on DNA, RNA, and protein synthesis in cell-free systems and intact cells*. Cancer Res, 1976. **36**(8): p. 2891-5.
33. Pang, B., et al., *Drug-induced histone eviction from open chromatin contributes to the chemotherapeutic effects of doxorubicin*. Nature Communications, 2013. **4**: p. 1908.
34. Wang, C.W., et al., *Cisplatin-, Doxorubicin-, and Docetaxel-Induced Cell Death Promoted by the Aqueous Extract of Solanum nigrum in Human Ovarian Carcinoma Cells*. Integr Cancer Ther, 2015. **14**(6): p. 546-55.
35. Vavrova, A., et al., *Catalytic Inhibitors of Topoisomerase II Differently Modulate the Toxicity of Anthracyclines in Cardiac and Cancer Cells*. PLOS ONE, 2013. **8**(10): p. e76676.
36. Organization, W.H. *WHO Medel List of Essential Medicines*. 2015; Available from: <http://www.who.int/medicines/publications/essentialmedicines/en/>.
37. Wang, S., et al., *Doxorubicin induces apoptosis in normal and tumor cells via distinctly different mechanisms. intermediacy of H(2)O(2)- and p53-dependent pathways*. J Biol Chem, 2004. **279**(24): p. 25535-43.
38. Ganz, W.I., et al., *Review of tests for monitoring doxorubicin-induced cardiomyopathy*. Oncology, 1996. **53**(6): p. 461-70.
39. Chatterjee, K., et al., *Doxorubicin cardiomyopathy*. Cardiology, 2010. **115**(2): p. 155-62.
40. Mills, J.K. and D. Needham, *Targeted drug delivery*. Expert Opinion on Therapeutic Patents, 1999. **9**(11): p. 1499-1513.

41. van Vlerken, L.E., T.K. Vyas, and M.M. Amiji, *Poly(ethylene glycol)-modified nanocarriers for tumor-targeted and intracellular delivery*. Pharm Res, 2007. **24**(8): p. 1405-14.
42. Yamaoka, T., Y. Tabata, and Y. Ikada, *Distribution and tissue uptake of poly(ethylene glycol) with different molecular weights after intravenous administration to mice*. J Pharm Sci, 1994. **83**(4): p. 601-6.
43. Gullotti, E. and Y. Yeo, *Extracellularly activated nanocarriers: a new paradigm of tumor targeted drug delivery*. Mol Pharm, 2009. **6**(4): p. 1041-51.
44. Yuan, F., et al., *Vascular permeability and microcirculation of gliomas and mammary carcinomas transplanted in rat and mouse cranial windows*. Cancer Res, 1994. **54**(17): p. 4564-8.
45. Hong, M., et al., *Efficient tumor targeting of hydroxycamptothecin loaded PEGylated niosomes modified with transferrin*. J Control Release, 2009. **133**(2): p. 96-102.
46. Deckert, P.M., *Current constructs and targets in clinical development for antibody-based cancer therapy*. Curr Drug Targets, 2009. **10**(2): p. 158-75.
47. Lentacker, I., et al., *New strategies for nucleic acid delivery to conquer cellular and nuclear membranes*. J Control Release, 2008. **132**(3): p. 279-88.
48. Farokhzad, O.C. and R. Langer, *Impact of Nanotechnology on Drug Delivery*. ACS Nano, 2009. **3**(1): p. 16-20.
49. Bae, Y.H. and K. Park, *Targeted drug delivery to tumors: myths, reality and possibility*. J Control Release, 2011. **153**(3): p. 198-205.
50. Bahrami, B., et al., *Nanoparticles and targeted drug delivery in cancer therapy*. Immunol Lett, 2017. **190**: p. 64-83.
51. Pirolo, K.F. and E.H. Chang, *Does a targeting ligand influence nanoparticle tumor localization or uptake?* Trends Biotechnol, 2008. **26**(10): p. 552-8.
52. Kirpotin, D.B., et al., *Antibody targeting of long-circulating lipidic nanoparticles does not increase tumor localization but does increase internalization in animal models*. Cancer Res, 2006. **66**(13): p. 6732-40.
53. Wen, D.Y., et al., *In vitro and in vivo variation in transferrin receptor expression on a human medulloblastoma cell line*. Neurosurgery, 1995. **36**(6): p. 1158-63; discussion 1163-4.
54. Noyhouzer, T., et al., *Ferrocene-Modified Phospholipid: An Innovative Precursor for Redox-Triggered Drug Delivery Vesicles Selective to Cancer Cells*. Langmuir, 2016. **32**(17): p. 4169-4178.
55. Zheng, Y., et al., *Fliposomes: trans-2-aminocyclohexanol-based amphiphiles as pH-sensitive conformational switches of liposome membrane - a structure-activity relationship study*. Chem Phys Lipids, 2018. **210**: p. 129-141.
56. Hobbs, S.K., et al., *Regulation of transport pathways in tumor vessels: role of tumor type and microenvironment*. Proc Natl Acad Sci U S A, 1998. **95**(8): p. 4607-12.
57. Scott, R.C., et al., *Aiming for the heart: targeted delivery of drugs to diseased cardiac tissue*. Expert Opin Drug Deliv, 2008. **5**(4): p. 459-70.
58. Din, F.U., et al., *Effective use of nanocarriers as drug delivery systems for the treatment of selected tumors*. Int J Nanomedicine, 2017. **12**: p. 7291-7309.
59. Lay, C.L., et al., *Delivery of paclitaxel by physically loading onto poly(ethylene glycol) (PEG)-graft-carbon nanotubes for potent cancer therapeutics*. Nanotechnology, 2010. **21**(6): p. 065101.

60. Lu, J., et al., *Mesoporous Silica Nanoparticles for Cancer Therapy: Energy-Dependent Cellular Uptake and Delivery of Paclitaxel to Cancer Cells*. *Nanobiotechnology*, 2007. **3**(2): p. 89-95.
61. Ji, Z., et al., *Targeted therapy of SMMC-7721 liver cancer in vitro and in vivo with carbon nanotubes based drug delivery system*. *J Colloid Interface Sci*, 2012. **365**(1): p. 143-9.
62. Lebold, T., et al., *Nanostructured silica materials as drug-delivery systems for Doxorubicin: single molecule and cellular studies*. *Nano Lett*, 2009. **9**(8): p. 2877-83.
63. Das, M., et al., *Augmented anticancer activity of a targeted, intracellularly activatable, theranostic nanomedicine based on fluorescent and radiolabeled, methotrexate-folic Acid-multiwalled carbon nanotube conjugate*. *Mol Pharm*, 2013. **10**(7): p. 2543-57.
64. Rosenholm, J.M., et al., *Cancer-cell-specific induction of apoptosis using mesoporous silica nanoparticles as drug-delivery vectors*. *Small*, 2010. **6**(11): p. 1234-41.
65. Iijima, S., *Helical microtubules of graphitic carbon*. *Nature*, 1991. **354**: p. 56.
66. Madani, S.Y., et al., *A new era of cancer treatment: carbon nanotubes as drug delivery tools*. *Int J Nanomedicine*, 2011. **6**: p. 2963-79.
67. Yan, Y., M.B. Chan-Park, and Q. Zhang, *Advances in Carbon-Nanotube Assembly*. *Small*, 2006. **3**(1): p. 24-42.
68. Slowing, II, et al., *Mesoporous silica nanoparticles as controlled release drug delivery and gene transfection carriers*. *Adv Drug Deliv Rev*, 2008. **60**(11): p. 1278-88.
69. Li, Y., et al., *Hollow Mesoporous Silica Nanoparticles with Tunable Structures for Controlled Drug Delivery*. *ACS Applied Materials & Interfaces*, 2017. **9**(3): p. 2123-2129.
70. Wang, Y., et al., *Mesoporous silica nanoparticles in drug delivery and biomedical applications*. *Nanomedicine: Nanotechnology, Biology and Medicine*, 2015. **11**(2): p. 313-327.
71. Xia, T., et al., *Polyethyleneimine coating enhances the cellular uptake of mesoporous silica nanoparticles and allows safe delivery of siRNA and DNA constructs*. *ACS Nano*, 2009. **3**(10): p. 3273-86.
72. Desai, D., et al., *Lipid Bilayer-Gated Mesoporous Silica Nanocarriers for Tumor-Targeted Delivery of Zoledronic Acid in Vivo*. *Mol Pharm*, 2017. **14**(9): p. 3218-3227.
73. Han, N., et al., *Hybrid lipid-capped mesoporous silica for stimuli-responsive drug release and overcoming multidrug resistance*. *ACS Appl Mater Interfaces*, 2015. **7**(5): p. 3342-51.
74. Manchester, M. and P. Singh, *Virus-based nanoparticles (VNPs): platform technologies for diagnostic imaging*. *Adv Drug Deliv Rev*, 2006. **58**(14): p. 1505-22.
75. Singh, P., et al., *Bio-distribution, toxicity and pathology of cowpea mosaic virus nanoparticles in vivo*. *J Control Release*, 2007. **120**(1-2): p. 41-50.
76. Pattenden, L.K., et al., *Towards the preparative and large-scale precision manufacture of virus-like particles*. *Trends Biotechnol*, 2005. **23**(10): p. 523-9.
77. Ma, Y., R.J.M. Nolte, and J.J.L.M. Cornelissen, *Virus-based nanocarriers for drug delivery*. *Advanced Drug Delivery Reviews*, 2012. **64**(9): p. 811-825.
78. Douglas, T. and M. Young, *Viruses: making friends with old foes*. *Science*, 2006. **312**(5775): p. 873-5.

79. Cao, J., et al., *Loading and release mechanism of red clover necrotic mosaic virus derived plant viral nanoparticles for drug delivery of doxorubicin*. *Small*, 2014. **10**(24): p. 5126-36.
80. Honarbakhsh, S., et al., *Polymeric systems incorporating plant viral nanoparticles for tailored release of therapeutics*. *Adv Healthc Mater*, 2013. **2**(7): p. 1001-7.
81. Sabin, J., et al., *Size and stability of liposomes: a possible role of hydration and osmotic forces*. *Eur Phys J E Soft Matter*, 2006. **20**(4): p. 401-8.
82. Weiner, N., *Phospholipid Liposomes: Properties and Potential Use in Flavor Encapsulation*, in *Flavor Technology*. 1997, American Chemical Society. p. 210-218.
83. Lembo, D. and R. Cavalli, *Nanoparticulate delivery systems for antiviral drugs*. *Antivir Chem Chemother*, 2010. **21**(2): p. 53-70.
84. Scherphof, G.L., et al., *Uptake and intracellular processing of targeted and nontargeted liposomes by rat Kupffer cells in vivo and in vitro*. *Ann N Y Acad Sci*, 1985. **446**: p. 368-84.
85. Alving, C.R., et al., *Therapy of leishmaniasis: superior efficacies of liposome-encapsulated drugs*. *Proc Natl Acad Sci U S A*, 1978. **75**(6): p. 2959-63.
86. Agrawal, A.K. and C.M. Gupta, *Tufts-in-bearing liposomes in treatment of macrophage-based infections*. *Adv Drug Deliv Rev*, 2000. **41**(2): p. 135-46.
87. Immordino, M.L., F. Dosio, and L. Cattel, *Stealth liposomes: review of the basic science, rationale, and clinical applications, existing and potential*. *Int J Nanomedicine*, 2006. **1**(3): p. 297-315.
88. Senior, J. and G. Gregoriadis, *Is half-life of circulating liposomes determined by changes in their permeability?* *FEBS Letters*, 1982. **145**(1): p. 109-114.
89. Hatakeyama, H., H. Akita, and H. Harashima, *The polyethyleneglycol dilemma: advantage and disadvantage of PEGylation of liposomes for systemic genes and nucleic acids delivery to tumors*. *Biol Pharm Bull*, 2013. **36**(6): p. 892-9.
90. Vert, M. and D. Domurado, *Poly(ethylene glycol): protein-repulsive or albumin-compatible?* *J Biomater Sci Polym Ed*, 2000. **11**(12): p. 1307-17.
91. Needham, D., T.J. McIntosh, and D.D. Lasic, *Repulsive interactions and mechanical stability of polymer-grafted lipid membranes*. *Biochim Biophys Acta*, 1992. **1108**(1): p. 40-8.
92. Ferreira, S.M.Z.M.D., et al., *Technetium-99m-labeled ceftizoxime loaded long-circulating and pH-sensitive liposomes used to identify osteomyelitis*. *Bioorganic & Medicinal Chemistry Letters*, 2012. **22**(14): p. 4605-4608.
93. Morilla, M.J., et al., *Etanidazole in pH-sensitive liposomes: Design, characterization and in vitro/in vivo anti-Trypanosoma cruzi activity*. *Journal of Controlled Release*, 2005. **103**(3): p. 599-607.
94. Andresen, T.L., S.S. Jensen, and K. Jørgensen, *Advanced strategies in liposomal cancer therapy: Problems and prospects of active and tumor specific drug release*. *Progress in Lipid Research*, 2005. **44**(1): p. 68-97.
95. Liu, X. and G. Huang, *Formation strategies, mechanism of intracellular delivery and potential clinical applications of pH-sensitive liposomes*. *Asian Journal of Pharmaceutical Sciences*, 2013. **8**(6): p. 319-328.
96. Kong, G., et al., *Efficacy of liposomes and hyperthermia in a human tumor xenograft model: importance of triggered drug release*. *Cancer Res*, 2000. **60**(24): p. 6950-7.

97. Zhang, H., et al., *Development and characteristics of temperature-sensitive liposomes for vinorelbine bitartrate*. International Journal of Pharmaceutics, 2011. **414**(1): p. 56-62.
98. Kim, M.S., et al., *Temperature-triggered tumor-specific delivery of anticancer agents by cRGD-conjugated thermosensitive liposomes*. Colloids and Surfaces B: Biointerfaces, 2014. **116**: p. 17-25.
99. Huang, S.-L., D.D. McPherson, and R.C. MacDonald, *A Method to Co-Encapsulate Gas and Drugs in Liposomes for Ultrasound-Controlled Drug Delivery*. Ultrasound in Medicine & Biology, 2008. **34**(8): p. 1272-1280.
100. Eloy, J.O., et al., *Liposomes as carriers of hydrophilic small molecule drugs: strategies to enhance encapsulation and delivery*. Colloids Surf B Biointerfaces, 2014. **123**: p. 345-63.
101. Kee, P.H., et al., *Synthesis, Acoustic Stability, and Pharmacologic Activities of Papaverine-Loaded Echogenic Liposomes for Ultrasound Controlled Drug Delivery*. Journal of Liposome Research, 2008. **18**(4): p. 263-277.
102. Lin, C.-Y., et al., *Ultrasound sensitive eLiposomes containing doxorubicin for drug targeting therapy*. Nanomedicine: Nanotechnology, Biology and Medicine, 2014. **10**(1): p. 67-76.
103. Saiyed, Z.M., N.H. Gandhi, and M.P. Nair, *Magnetic nanoformulation of azidothymidine 5'-triphosphate for targeted delivery across the blood-brain barrier*. Int J Nanomedicine, 2010. **5**: p. 157-66.
104. Faria, M.R., et al., *Synthesis and characterization of magnetoliposomes for MRI contrast enhancement*. International Journal of Pharmaceutics, 2013. **446**(1): p. 183-190.
105. Kawai, N., et al., *Anticancer effect of hyperthermia on prostate cancer mediated by magnetite cationic liposomes and immune-response induction in transplanted syngeneic rats*. 2005. **64**(4): p. 373-381.
106. Clares, B., et al., *Nano-engineering of 5-fluorouracil-loaded magnetoliposomes for combined hyperthermia and chemotherapy against colon cancer*. European Journal of Pharmaceutics and Biopharmaceutics, 2013. **85**(3, Part A): p. 329-338.
107. Jain, S., et al., *RGD-anchored magnetic liposomes for monocytes/neutrophils-mediated brain targeting*. International Journal of Pharmaceutics, 2003. **261**(1): p. 43-55.
108. Yavlovich, A., et al., *Light-sensitive lipid-based nanoparticles for drug delivery: design principles and future considerations for biological applications*. Molecular Membrane Biology, 2010. **27**(7): p. 364-381.
109. de Visscher, S.A.H.J., et al., *Fluorescence localization and kinetics of mTHPC and liposomal formulations of mTHPC in the window-chamber tumor model*. 2011. **43**(6): p. 528-536.
110. Yavlovich, A., et al., *A novel class of photo-triggerable liposomes containing DPPC:DC8,9PC as vehicles for delivery of doxorubicin to cells*. Biochimica et Biophysica Acta (BBA) - Biomembranes, 2011. **1808**(1): p. 117-126.
111. Wu, C., C. Yu, and M. Chu, *A gold nanoshell with a silica inner shell synthesized using liposome templates for doxorubicin loading and near-infrared photothermal therapy*. Int J Nanomedicine, 2011. **6**: p. 807-13.
112. You, J., et al., *Near-Infrared Light-Sensitive Liposomes for the Enhanced Photothermal Tumor Treatment by the Combination with Chemotherapy*. Pharmaceutical Research, 2014. **31**(3): p. 554-565.

113. Engin, K., et al., *Extracellular pH distribution in human tumours*. International Journal of Hyperthermia, 1995. **11**(2): p. 211-216.
114. Stubbs, M., et al., *Causes and consequences of tumour acidity and implications for treatment*. Molecular Medicine Today, 2000. **6**(1): p. 15-19.
115. Lee, E.S., et al., *Tumor pH-responsive flower-like micelles of poly(l-lactic acid)-b-poly(ethylene glycol)-b-poly(l-histidine)*. Journal of Controlled Release, 2007. **123**(1): p. 19-26.
116. Evjen, T.J., et al., *Lipid membrane composition influences drug release from dioleoylphosphatidylethanolamine-based liposomes on exposure to ultrasound*. International Journal of Pharmaceutics, 2011. **406**(1): p. 114-116.
117. Legendre, J.-Y. and F.C. Szoka Jr, *Delivery of Plasmid DNA into Mammalian Cell Lines Using pH-Sensitive Liposomes: Comparison with Cationic Liposomes*. Pharmaceutical Research, 1992. **9**(10): p. 1235-1242.
118. Drummond, D.C. and D.L. Daleke, *Synthesis and characterization of N-acylated, pH-sensitive 'caged' aminophospholipids*. Chemistry and Physics of Lipids, 1995. **75**(1): p. 27-41.
119. Mastrobattista, E., et al., *Functional characterization of an endosome-disruptive peptide and its application in cytosolic delivery of immunoliposome-entrapped proteins*. J Biol Chem, 2002. **277**(30): p. 27135-43.
120. Simões, S., et al., *On the formulation of pH-sensitive liposomes with long circulation times*. Advanced Drug Delivery Reviews, 2004. **56**(7): p. 947-965.
121. Barea, M.J., et al., *Evaluation of liposomes coated with a pH responsive polymer*. International Journal of Pharmaceutics, 2010. **402**(1): p. 89-94.
122. Liu, X., et al., *Fliposomes: pH-triggered conformational flip of new trans-2-aminocyclohexanol-based amphiphiles causes instant cargo release in liposomes*. J Liposome Res, 2012. **22**(4): p. 319-28.
123. Samoshina, N.M., et al., *Fliposomes: pH-Sensitive Liposomes Containing a trans-2-morpholinocyclohexanol-Based Lipid That Performs a Conformational Flip and Triggers an Instant Cargo Release in Acidic Medium*. Pharmaceutics, 2011. **3**(3): p. 379-405.
124. Brazdova, B., et al., *trans-2-Aminocyclohexanol as a pH-sensitive conformational switch in lipid amphiphiles*. Chem Commun (Camb), 2008(39): p. 4774-6.
125. Samoshin, A.V., et al., *Fliposomes: new amphiphiles based on trans-3,4-bis(acyloxy)-piperidine able to perform a pH-triggered conformational flip and cause an instant cargo release from liposomes*. Tetrahedron Letters, 2013. **54**(41): p. 5600-5604.
126. Zheng, Y., et al., *trans-2-Aminocyclohexanol-based amphiphiles as highly efficient helper lipids for gene delivery by lipoplexes*. Biochim Biophys Acta, 2015. **1848**(12): p. 3113-25.
127. Kamal, A., et al., *Copper(II) tetrafluoroborate-catalyzed ring-opening of epoxides by amines*. Tetrahedron Letters, 2005. **46**(15): p. 2675-2677.
128. Chemistry, T.J.o.O., *Guidelines for Authors*. 2018.
129. Avanti Polar Lipids, I., *What is the transition temperature of the lipid*. 2018.
130. Mozafari, M.R., *Nanoliposomes: preparation and analysis*. Methods Mol Biol, 2010. **605**: p. 29-50.
131. Avanti Polar Lipids, I., *Phase_Transition_Temps_for_Glycerophospholipids*. 2018.
132. Mozafari, M.R., et al., *Nanoliposomes and their applications in food nanotechnology*. J Liposome Res, 2008. **18**(4): p. 309-27.

133. Akbarzadeh, A., et al., *Liposome: classification, preparation, and applications*. 2013. **8**(1): p. 102.
134. Riaz, M., *Liposomes preparation methods*. Pak J Pharm Sci, 1996. **9**(1): p. 65-77.
135. Liu, L. and T. Yonetani, *Preparation and characterization of liposome-encapsulated haemoglobin by a freeze-thaw method*. J Microencapsul, 1994. **11**(4): p. 409-21.
136. Pick, U., *Liposomes with a large trapping capacity prepared by freezing and thawing of sonicated phospholipid mixtures*. Arch Biochem Biophys, 1981. **212**(1): p. 186-94.
137. Himanshu Anwekar, S.P., A.K Singhai, *Liposome as drug carriers*. IJPLS, 2011. **2**(7): p. 945-951.
138. Benny C. L. Cheung, T.H.T.S., Johanna M. Leenhouts, Pieter R. Cullis, *Loading of doxorubicin into liposomes by forming Mn²⁺-drug complexes*. Biochimica et Biophysica Acta (BBA) - Biomembranes, 1998. **Volume 1414**(Issues 1–2): p. Pages 205-216.
139. Amselem, S., A. Gabizon, and Y. Barenholz, *Optimization and upscaling of doxorubicin-containing liposomes for clinical use*. J Pharm Sci, 1990. **79**(12): p. 1045-52.
140. Amselem, S., Y. Barenholz, and A. Gabizon, *Optimization and Upscaling of Doxorubicin-Containing Liposomes for Clinical Use*. Journal of Pharmaceutical Sciences, 1990. **79**(12): p. 1045-1052.
141. Fujisawa, S., et al., *Dipalmitoylphosphatidylcholine (DPPC) and DPPC/cholesterol liposomes as predictors of the cytotoxicity of bis-GMA related compounds*. J Liposome Res, 2004. **14**(1-2): p. 39-49.
142. Monnard, P.-A., T. Oberholzer, and P. Luisi, *Entrapment of nucleic acids in liposomes*. Biochimica et Biophysica Acta (BBA) - Biomembranes, 1997. **1329**(1): p. 39-50.
143. RxList. *DOXIL Drug Description*. 2017; Available from: <https://www.rxlist.com/doxil-drug.htm#description>.
144. Briuglia, M.L., et al., *Influence of cholesterol on liposome stability and on in vitro drug release*. Drug Deliv Transl Res, 2015. **5**(3): p. 231-42.
145. Bertrand, N. and J.C. Leroux, *The journey of a drug-carrier in the body: an anatomophysiological perspective*. J Control Release, 2012. **161**(2): p. 152-63.
146. Bertrand, N. and J.-C. Leroux, *The journey of a drug-carrier in the body: An anatomophysiological perspective*. Journal of Controlled Release, 2012. **161**(2): p. 152-163.
147. Blasi, P., et al., *Solid lipid nanoparticles for targeted brain drug delivery*. Advanced Drug Delivery Reviews, 2007. **59**(6): p. 454-477.
148. Caracciolo, G., *Clinically approved liposomal nanomedicines: lessons learned from the biomolecular corona*. Nanoscale, 2018. **10**(9): p. 4167-4172.
149. Maeda, H., *Toward a full understanding of the EPR effect in primary and metastatic tumors as well as issues related to its heterogeneity*. Advanced Drug Delivery Reviews, 2015. **91**: p. 3-6.
150. Azhar Shekoufeh Bahari, L. and H. Hamishehkar, *The Impact of Variables on Particle Size of Solid Lipid Nanoparticles and Nanostructured Lipid Carriers; A Comparative Literature Review*. Adv Pharm Bull, 2016. **6**(2): p. 143-51.
151. Gyanani, V., *Turning stealth liposomes into cationic liposomes for anticancer drug delivery*. dissertation, 2013.
152. Khomutov, G.B., et al., *Langmuir monolayers and Langmuir-Blodgett films of pH-sensitive lipid*. Colloids and Surfaces A: Physicochemical and Engineering Aspects, 2017. **532**: p. 150-154.

153. Zheng, Y., *synthesis and conformational study of trans-2-aminocyclohexanol-based pH-triggered molecular switches and their application in gene delivery*. dissertation, 2013.
154. Baker, B.M. and C.S. Chen, *Deconstructing the third dimension – how 3D culture microenvironments alter cellular cues*. 2012. **125**(13): p. 3015-3024.
155. Amann, A., et al., *Development of an innovative 3D cell culture system to study tumour-stroma interactions in non-small cell lung cancer cells*. PLoS One, 2014. **9**(3): p. e92511.
156. Weaver, V.M., et al., *beta4 integrin-dependent formation of polarized three-dimensional architecture confers resistance to apoptosis in normal and malignant mammary epithelium*. Cancer Cell, 2002. **2**(3): p. 205-16.
157. Yamada, K.M. and E. Cukierman, *Modeling tissue morphogenesis and cancer in 3D*. Cell, 2007. **130**(4): p. 601-10.
158. Nath, S. and G.R. Devi, *Three-dimensional culture systems in cancer research: Focus on tumor spheroid model*. Pharmacology & Therapeutics, 2016. **163**: p. 94-108.
159. Wang, C., et al., *Three-dimensional in vitro cancer models: a short review*. Biofabrication, 2014. **6**(2): p. 022001.
160. Oloumi, A., et al., *Identification of genes differentially expressed in V79 cells grown as multicell spheroids*. Int J Radiat Biol, 2002. **78**(6): p. 483-92.
161. Andre, F., N. Berrada, and C. Desmedt, *Implication of tumor microenvironment in the resistance to chemotherapy in breast cancer patients*. Curr Opin Oncol, 2010. **22**(6): p. 547-51.
162. Kim, S.H., H.J. Kuh, and C.R. Dass, *The reciprocal interaction: chemotherapy and tumor microenvironment*. Curr Drug Discov Technol, 2011. **8**(2): p. 102-6.
163. Shekhar, M.P., *Drug resistance: challenges to effective therapy*. Curr Cancer Drug Targets, 2011. **11**(5): p. 613-23.
164. Freyer, J.P. and R.M. Sutherland, *Regulation of growth saturation and development of necrosis in EMT6/Ro multicellular spheroids by the glucose and oxygen supply*. Cancer Res, 1986. **46**(7): p. 3504-12.
165. Khaitan, D., et al., *Establishment and characterization of multicellular spheroids from a human glioma cell line; Implications for tumor therapy*. J Transl Med, 2006. **4**: p. 12.
166. Mueller-Klieser, W., J.P. Freyer, and R.M. Sutherland, *Influence of glucose and oxygen supply conditions on the oxygenation of multicellular spheroids*. Br J Cancer, 1986. **53**(3): p. 345-53.
167. Sant, S. and P.A. Johnston, *The production of 3D tumor spheroids for cancer drug discovery*. Drug Discov Today Technol, 2017. **23**: p. 27-36.
168. Lovitt, C.J., T.B. Shelper, and V.M. Avery, *Miniaturized Three-Dimensional Cancer Model for Drug Evaluation*. ASSAY and Drug Development Technologies, 2013. **11**(7): p. 435-448.
169. Cui, X., Y. Hartanto, and H. Zhang, *Advances in multicellular spheroids formation*. J R Soc Interface, 2017. **14**(127).
170. Graf, B.W. and S.A. Boppart, *Imaging and analysis of three-dimensional cell culture models*. Methods Mol Biol, 2010. **591**: p. 211-27.
171. Schmitt, J.M., A. Knüttel, and M. Yadlowsky, *Confocal microscopy in turbid media*. J Opt Soc Am A Opt Image Sci Vis, 1994. **11**(8): p. 2226-35.
172. Smithpeter, C.L., et al., *Penetration depth limits of in vivo confocal reflectance imaging*. Appl Opt, 1998. **37**(13): p. 2749-54.

173. Abella, I.D., *Optical Double-Photon Absorption in Cesium Vapor*. Physical Review Letters, 1962. **9**(11): p. 453-455.
174. Centonze, V.E. and J.G. White, *Multiphoton excitation provides optical sections from deeper within scattering specimens than confocal imaging*. Biophys J, 1998. **75**(4): p. 2015-24.
175. ThermoFisher Scientific. *Snarf pH indicators*. 2003; Available from: <https://www.thermofisher.com/order/catalog/product/C1270>.
176. Lin, R.Z. and H.Y. Chang, *Recent advances in three-dimensional multicellular spheroid culture for biomedical research*. Biotechnol J, 2008. **3**(9-10): p. 1172-84.
177. Kunz-Schughart, L.A., et al., *The use of 3-D cultures for high-throughput screening: the multicellular spheroid model*. J Biomol Screen, 2004. **9**(4): p. 273-85.
178. Swietach, P., et al., *Tumor-associated carbonic anhydrase 9 spatially coordinates intracellular pH in three-dimensional multicellular growths*. J Biol Chem, 2008. **283**(29): p. 20473-83.
179. Lee, J., et al., *In vitro toxicity testing of nanoparticles in 3D cell culture*. Small, 2009. **5**(10): p. 1213-21.
180. Pickl, M. and C.H. Ries, *Comparison of 3D and 2D tumor models reveals enhanced HER2 activation in 3D associated with an increased response to trastuzumab*. Oncogene, 2009. **28**(3): p. 461-8.
181. Sun, T., et al., *Culture of skin cells in 3D rather than 2D improves their ability to survive exposure to cytotoxic agents*. J Biotechnol, 2006. **122**(3): p. 372-81.
182. Colley, H.E., et al., *Polymersome-mediated delivery of combination anticancer therapy to head and neck cancer cells: 2D and 3D in vitro evaluation*. Mol Pharm, 2014. **11**(4): p. 1176-88.
183. Sprague, L., et al., *Dendritic cells: In vitro culture in two- and three-dimensional collagen systems and expression of collagen receptors in tumors and atherosclerotic microenvironments*. Exp Cell Res, 2014. **323**(1): p. 7-27.
184. Ocana, A., et al., *Preclinical development of molecular-targeted agents for cancer*. Nature Reviews Clinical Oncology, 2010. **8**: p. 200.
185. Hait, W.N., *Anticancer drug development: the grand challenges*. Nature Reviews Drug Discovery, 2010. **9**: p. 253.
186. Hutchinson, L. and R. Kirk, *High drug attrition rates—where are we going wrong?* Nature Reviews Clinical Oncology, 2011. **8**: p. 189.
187. Kabadi, P.K., et al., *Into the depths: Techniques for in vitro three-dimensional microtissue visualization*. Biotechniques, 2015. **59**(5): p. 279-86.
188. Zheng, M.J., et al., *A novel mouse model of gastric cancer with human gastric microenvironment*. Cancer Lett, 2012. **325**(1): p. 108-15.
189. Pampaloni, F., E.G. Reynaud, and E.H.K. Stelzer, *The third dimension bridges the gap between cell culture and live tissue*. Nature Reviews Molecular Cell Biology, 2007. **8**: p. 839.
190. Sarah-Louise, R., et al., *Drug Discovery Approaches Utilizing Three-Dimensional Cell Culture*. 2016. **14**(1): p. 19-28.
191. Mehta, G., et al., *Opportunities and challenges for use of tumor spheroids as models to test drug delivery and efficacy*. J Control Release, 2012. **164**(2): p. 192-204.

192. Bartosh, T.J., et al., *Aggregation of human mesenchymal stromal cells (MSCs) into 3D spheroids enhances their antiinflammatory properties*. Proc Natl Acad Sci U S A, 2010. **107**(31): p. 13724-9.
193. Fang, D.D., et al., *Expansion of CD133(+) colon cancer cultures retaining stem cell properties to enable cancer stem cell target discovery*. Br J Cancer, 2010. **102**(8): p. 1265-75.
194. Raof, N.A., et al., *Bioengineering embryonic stem cell microenvironments for exploring inhibitory effects on metastatic breast cancer cells*. Biomaterials, 2011. **32**(17): p. 4130-9.
195. Wang, L., et al., *Isolation and characterization of stem-like cells from a human ovarian cancer cell line*. Mol Cell Biochem, 2012. **363**(1-2): p. 257-68.
196. Bhadriraju, K. and C.S. Chen, *Engineering cellular microenvironments to improve cell-based drug testing*. Drug Discov Today, 2002. **7**(11): p. 612-20.
197. Baek, N., et al., *Monitoring the effects of doxorubicin on 3D-spheroid tumor cells in real-time*. Onco Targets Ther, 2016. **9**: p. 7207-7218.
198. Raghunand, N., et al., *Enhancement of chemotherapy by manipulation of tumour pH*. Br J Cancer, 1999. **80**(7): p. 1005-11.
199. Gerweck, L.E., S.V. Kozin, and S.J. Stocks, *The pH partition theory predicts the accumulation and toxicity of doxorubicin in normal and low-pH-adapted cells*. Br J Cancer, 1999. **79**(5-6): p. 838-42.
200. Gerweck, L.E., S. Vijayappa, and S. Kozin, *Tumor pH controls the in vivo efficacy of weak acid and base chemotherapeutics*. Mol Cancer Ther, 2006. **5**(5): p. 1275-9.
201. Centonze, V.E. and J.G. White, *Multiphoton Excitation Provides Optical Sections from Deeper within Scattering Specimens than Confocal Imaging*. Biophysical Journal, 1998. **75**(4): p. 2015-2024.
202. Eetezadi, S., et al., *Effects of Doxorubicin Delivery Systems and Mild Hyperthermia on Tissue Penetration in 3D Cell Culture Models of Ovarian Cancer Residual Disease*. Mol Pharm, 2015. **12**(11): p. 3973-85.
203. Kostarelos, K., et al., *Engineering lipid vesicles of enhanced intratumoral transport capabilities: correlating liposome characteristics with penetration into human prostate tumor spheroids*. J Liposome Res, 2005. **15**(1-2): p. 15-27.